HAL
open science

Evaluation of CNRM Earth-System model, CNRM-ESM 2-1: role of Earth system processes in present-day and future climate

Roland Séférian, Pierre Nabat, M. Michou, David Saint-Martin, Aurore Voldoire, Jeanne Colin, B. Decharme, Christine Delire, Sarah Berthet, Matthieu Chevallier, et al.

▶ To cite this version:

Roland Séférian, Pierre Nabat, M. Michou, David Saint-Martin, Aurore Voldoire, et al.. Evaluation of CNRM Earth-System model, CNRM-ESM 2-1: role of Earth system processes in present-day and future climate. Journal of Advances in Modeling Earth Systems, 2019, 11 (12), pp.4182-4227. 10.1029/2019MS001791 . hal-02403201

HAL Id: hal-02403201

https://hal.science/hal-02403201v1

Submitted on 19 Nov 2020

HAL is a multi-disciplinary open access archive for the deposit and dissemination of scientific research documents, whether they are published or not. The documents may come from teaching and research institutions in France or abroad, or from public or private research centers.

L'archive ouverte pluridisciplinaire **HAL**, est destinée au dépôt et à la diffusion de documents scientifiques de niveau recherche, publiés ou non, émanant des établissements d'enseignement et de recherche français ou étrangers, des laboratoires publics ou privés.

JAMES | Journal of Advances in Modeling Earth Systems

RESEARCH ARTICLE
10.1029/2019MS001791

Special Section:
The CNRM Climate and Earth System Models for CMIP6

Key Points:
- This study introduces CNRM-ESM2-1 and describes its set-up for CMIP6
- Represented Earth system processes further impact the model response to external forcing than the model performance over present-day
- Represented Earth system processes damp future warming by up to 10%

Supporting Information:
- Supporting Information S1

Correspondence to:
R. Séférian,
roland.seferian@meteo.fr

Citation:
Séférian, R., Nabat, P., Michou, M., Saint-Martin, D., Voldoire, A., Colin, J., et al (2019). Evaluation of CNRM Earth-System model, CNRM-ESM2-1: role of Earth system processes in present-day and future climate. *Journal of Advances in Modeling Earth Systems*, *11*, 4182–4227. https://doi.org/10.1029/2019MS001791

Received 22 JUN 2019
Accepted 23 OCT 2019
Accepted article online 6 NOV 2019
Published online 10 DEC 2019

©2019. The Authors.
This is an open access article under the terms of the Creative Commons Attribution-NonCommercial-NoDerivs License, which permits use and distribution in any medium, provided the original work is properly cited, the use is non-commercial and no modifications or adaptations are made.

Evaluation of CNRM Earth System Model, CNRM-ESM2-1: Role of Earth System Processes in Present-Day and Future Climate

Roland Séférian[1], Pierre Nabat[1], Martine Michou[1], David Saint-Martin[1], Aurore Voldoire[1], Jeanne Colin[1], Bertrand Decharme[1], Christine Delire[1], Sarah Berthet[1], Matthieu Chevallier[1], Stephane Sénési[1], Laurent Franchisteguy[1], Jessica Vial[2], Marc Mallet[1], Emilie Joetzjer[1], Olivier Geoffroy[1], Jean-François Guérémy[1], Marie-Pierre Moine[3], Rym Msadek[3], Aurélien Ribes[1], Matthias Rocher[1], Romain Roehrig[1], David Salas-y-Mélia[1], Emilia Sanchez[3], Laurent Terray[3], Sophie Valcke[3], Robin Waldman[1], Olivier Aumont[4], Laurent Bopp[2], Julie Deshayes[4], Christian Éthé[5], and Gurvan Madec[4,6]

[1]CNRM, Université de Toulouse, Météo-France, CNRS, Toulouse, France, [2]Ecole Normale Supérieure/PSL Res. Univ, Ecole Polytechnique, Sorbonne Université, Paris, France, [3]CECI, Université de Toulouse, CNRS, CERFACS, Toulouse, France, [4]LOCEAN-IPSL, Sorbonne Université-CNRS-IRD-MNHN, Paris, France, [5]Institut Pierre Simon Laplace, Paris, France, [6]INRIA, Université Grenoble Alpes, Grenoble, France

Abstract This study introduces CNRM-ESM2-1, the Earth system (ES) model of second generation developed by CNRM-CERFACS for the sixth phase of the Coupled Model Intercomparison Project (CMIP6). CNRM-ESM2-1 offers a higher model complexity than the Atmosphere-Ocean General Circulation Model CNRM-CM6-1 by adding interactive ES components such as carbon cycle, aerosols, and atmospheric chemistry. As both models share the same code, physical parameterizations, and grid resolution, they offer a fully traceable framework to investigate how far the represented ES processes impact the model performance over present-day, response to external forcing and future climate projections. Using a large variety of CMIP6 experiments, we show that represented ES processes impact more prominently the model response to external forcing than the model performance over present-day. Both models display comparable performance at replicating modern observations although the mean climate of CNRM-ESM2-1 is slightly warmer than that of CNRM-CM6-1. This difference arises from land cover-aerosol interactions where the use of different soil vegetation distributions between both models impacts the rate of dust emissions. This interaction results in a smaller aerosol burden in CNRM-ESM2-1 than in CNRM-CM6-1, leading to a different surface radiative budget and climate. Greater differences are found when comparing the model response to external forcing and future climate projections. Represented ES processes damp future warming by up to 10% in CNRM-ESM2-1 with respect to CNRM-CM6-1. The representation of land vegetation and the CO_2-water-stomatal feedback between both models explain about 60% of this difference. The remainder is driven by other ES feedbacks such as the natural aerosol feedback.

1. Introduction

The sixth phase of the Coupled Model Intercomparison Project (CMIP6, Eyring et al. (2016)) is a standard experimental protocol for studying the outputs of coupled Atmosphere-Ocean General Circulation Models (AOGCMs) and Earth system models (ESMs). Proposed experiments aim at addressing outstanding scientific questions that arose as part of the process leading to the elaboration of the Sixth Assessment Report (AR6) by the Intergovernmental Panel on Climate Change (IPCC). The goal is to improve the understanding of climate and to provide estimates of future climate change that will be useful to those considering its possible consequences and the effect of mitigation strategies.

Compared to the fifth phase of the Coupled Model Intercomparison Project (CMIP5), CMIP6 proposes to stratify analyses within focused model intercomparison projects (MIPs) endorsed by CMIP6, which altogether aim to:

1. Compare models' versions between each other within an ensemble of models of the same generation or across an ensemble of models of different generations and evaluate how realistic these models are in simulating the recent past.
2. Characterize the model's response to external forcing, and, in particular, understand some of the factors responsible for differences in model projections, including quantifying some key feedbacks such as those involving clouds and the carbon cycle.
3. Prospect the range of magnitude and pace of climate change at centennial timescales given an ensemble of scenarios considering the role of the climate variability at interannual and decadal timescales, and assess the predictability of relevant climate variables.

In order to support research on these overarching topics, the CNRM-CERFACS climate group aims at contributing to a large number of MIPs using three different models (Table 1): the standard resolution (i.e., ~1° or ~140 km) AOGCM of sixth generation (CNRM-CM6-1, Voldoire et al. (2019)), the high-resolution (i.e., ~0.5° or ~50 km) AOGCM (CNRM-CM6-HR), and the standard (i.e., ~1° or ~140 km) resolution Earth system model of second generation (CNRM-ESM2-1, this study). These three models have been designed to tackle the overarching scientific questions as proposed by CMIP6 using an alternative mapping (with respect to CMIP5) pending on model resolution and complexity.

This paper provides key information relative to CNRM-ESM2-1 contribution to CMIP6. In particular, we document the development of CNRM-ESM2-1, which uses the physical-dynamical core of the ocean-atmosphere coupled climate model CNRM-CM6-1 as detailed in Voldoire et al. (2019) and accounts for several Earth system feedbacks enabled by interactive atmospheric chemistry and aerosols, as well as interactive land and ocean carbon cycles. We also detail the modeling setup used for CMIP6 including the use of recommended forcing and the spin-up strategy.

So far, the published literature assessed in IPCC AR4 (2007) and in IPCC AR5 (2013) has assumed that the inclusion of Earth system components in a climate model may affect predictions of future climate for a given forcing because of the representation of biogeochemical and other Earth system feedbacks (e.g., Ciais et al., 2013). It is also believed that this inclusion could degrade the model's simulation of the present-day climate since driving inputs originally derived from observed quantities (such as aerosols, vegetation, or ocean chlorophyll distributions) are replaced by interactive schemes for which the driving processes remain poorly constrained and are potentially less well understood than physical processes (e.g., Booth et al., 2012; De Noblet-Ducoudré et al., 2012; Friedlingstein et al., 2014). However, both working hypotheses have not been disproved or corroborated to date because of the lack of traceable AOGCM/ESM pairs from the various modeling groups at the time of CMIP5 (e.g., see Table 9.1 in Flato et al. (2013)).

Here, the comparison between CNRM-ESM2-1 and CNRM-CM6-1 provides a comprehensive framework to investigate how far an ESM can differ from an AOGCM when they are both based on the same physical core. Indeed, the development of CNRM-ESM2-1 and CNRM-CM6-1 has been guided to ensure the maximum of compatibility between both configurations, which substantially contrasts with the previous cycle of development for CMIP5 configurations where CNRM-CM5 and CNRM-ESM 1 were based on different codes.

As a consequence, this manuscript aims at assessing the "traceability" of CNRM-ESM2-1 with respect to CNRM-CM6-1. Traceability can be understood as a comprehensive description of differences between these two models, either in terms of code or represented processes, and their impact in terms of present-day mean state climate and response to external forcings.

This manuscript is structured as follows: the model is presented in section 2; section 3 describes the modeling setup employed for CMIP6; the results of the CNRM-ESM2-1 simulations are discussed in section 4; and finally, conclusions are summarized in section 5.

2. CNRM-ESM2-1 Components

2.1. The Physical Core

2.1.1. Physical Components Shared With CNRM-CM6-1

CNRM-ESM2-1 is based on the physical core of the CNRM-CM6-1 AOGCM which represents atmosphere, land, ocean, and sea ice physical as well as dynamical processes and their interactions (Voldoire et al., 2019).

Table 1
Overview of the CNRM-CERFACS Contribution to CMIP6, Including the Assumed Fit for Purpose of These Models

MIPs		Scope	CNRM-CERFACS models	Fit for purpose
CMIP6 entry card	DECK[1]	Benchmarking model's general equilibrium and response to CO_2	CNRM-CM6-1, CNRM-ESM2-1, and CNRM-CM6-HR	Aim at documenting the model uncertainty as function of the internal variability (with large number of model realizations), forcing and resolved processes, and model resolution
	Historical[1]	Benchmarking models against modern observations	CNRM-CM6-1, CNRM-ESM2-1, and CNRM-CM6-HR	
Projections, predictions, and variability	ScenarioMIP[2]	Explore future climate outcomes	CNRM-CM6-1, CNRM-ESM2-1, and CNRM-CM6-HR	
	GeoMIP[3]	Explore potential solutions to limit global warming using solar radiation management	CNRM-ESM2-1	Includes all represented processes in order to sample of the "true" climate uncertainty and assesses impacts of solar radiation management and carbon dioxide removal on terrestrial and oceanic ecosystem
	CDRMIP[4]*	Explore potential solutions to limit global warming using carbon dioxide removal	CNRM-ESM2-1	
	DCPP[5]	Explore potential and effective near-term predictions	CNRM-CM6-1	Includes know processes at play at decadal timescales and captures the range of the internal decadal variability with a large number of realizations
Reality check and bias understanding	OMIP[6]	Understand systematic errors in ocean components of climate models	Ocean component of CNRM-CM6-1 and CNRM-ESM2-1	Include relevant ocean physical and/or biogeochemical processes as used in coupled model configurations
	LS3MIP[7]	Understand systematic errors in land surface components of climate models	Land component of CNRM-CM6-1 and CNRM-ESM2-1	Include relevant land physical and/or biogeochemical processes as used in coupled model configurations
	SIMIP[8]	Improve our understanding of the role of sea ice in the climate system	CNRM-CM6-1, CNRM-CM6-1-HR, and CNRM-ESM2-1	Include relevant sea ice physical processes as used in coupled model configurations
	GMMIP[9]	Analysis of the climatology and variability of monsoons and of their future changes; evaluation of the monsoon representation in climate models	CNRM-CM6-1	Ensemble of SST-imposed and coupled historical simulations
	HighResMIP[10]	Determine how far systematic biases are related to model resolution	CNRM-CM6-1 and CNRM-CM6-HR	Include the same suite of processes; the two models only differ with their horizontal resolution
Response to external forcings and assessment of climate and Earth system feedbacks	AerChemMIP[11]	Improve the quantification of aerosols and chemically reactive gases impacts on past and future climate, and vice versa	CNRM-ESM2-1	Includes an interactive representation of aerosols and chemistry and targeted contributions of various climate forcers
	C4MIP[12]	Understand and quantify the role of carbon cycle feedbacks	CNRM-ESM2-1	Simulates atmosphere, land, and ocean carbon cycle interactively; can be driven by CO2 emissions
	CFMIP[13]	Understanding and evaluation of cloud feedbacks and the response of large-scale atmospheric circulation and regional-scale precipitation to forcings	CNRM-CM6-1	Enables a hierarchy of model configurations (aquaplanet, atmosphere-only and coupled models), and allows to switch on/off of the cloud radiative effect (at least for the longwave component)
	DAMIP[14]	Understand and disentangle the role of external forcing considering the internal variability	CNRM-CM6-1	Ability to simulate forced response consistent with observation over the historical period
	FAFMIP[15]		CNRM-CM6-1	

Table 1
(continued)

MIPs		Scope	CNRM-CERFACS models	Fit for purpose
		Investigate the model spread in projections of CO_2-forced sea-level and ocean climate change		Resolves the main components of the ocean and sea ice water and energy budgets
	ISMIP6[16]	Improve projections of sea level rise via improved projections of the Greenland and Antarctic ice sheets	CNRM-CM6-1	Takes into account Greenland and Antarctic ice sheets melting in a semi-prognostics mode (use water flow from external ice sheet models)
	LUMIP[17]	Understand and quantify the role of land use and land cover changes in past, recent, and future climate	CNRM-ESM2-1	Takes into account land use and land cover changes processes
	PMIP[18]	Evaluate the ability of climate models in simulating past climates, and understand the associated mechanisms	CNRM-CM6-1	Paleoclimate configurations of the model (including the use of past orbital parameters) are available
	RFMIP[19]	Improve the understanding of climate model errors and spread in simulating radiative forcing and the associated climate system response	CNRM-CM6-1 and CNRM-ESM2-1	Enables hierarchy of simulations to assess the radiative forcing of greenhouse gases or aerosols; online diagnostics of various aspects of radiative forcings; offline radiative transfer calculations
	VolMIP[20]	Improve the understanding of climate response to volcanic eruption	Not participating	Not participating
	PAMIP[21]	Improve our understanding of polar amplification phenomenon	CNRM-CM6-1	Includes atmospheric and oceanic processes relevant for the high latitude response to sea ice and SST changes. Use of large ensembles to maximize the signal-to-noise ratio
	ZECMIP[22]	Improve the quantification of the zero emission commitment	CNRM-ESM2-1	Includes all represented processes require to run in emission-driven mode and assess the model response when CO_2 emissions are set to zero
Regional downscaling	CORDEX-MIP	Regional dynamical downscaling of historical and scenarios output	CNRM-ESM2-1	Provide the output necessary to force regional climate model with ensuing studies (impacts, vulnerability, adaptation and climate services)

Note. Reference papers are given as follows: [1]Eyring et al. (2016); [2]O'Neill et al. (2016); [3]Kravitz et al. (2015); [4]Keller et al. (2018); 5Boer et al. (2016); [6]Griffies et al. (2016); [7]van den Hurk et al. (2016); [8]Notz et al. (2016); [9]Zhou et al. (2016); [10]Haarsma et al. (2016); [11]Collins et al. (2017); [12]Jones et al. (2016); [13]Webb et al. (2017); [14]Gillett et al. (2016); [15]Gregory et al. (2016); [16]Nowicki et al. (2016); [17]Lawrence et al. (2016); [18]Kageyama et al. (2018); [19]Pincus et al. (2016); [20]Zanchettin et al. (2016); [21]Smith et al. (2018); [22]Jones et al. (2019); *indicates an optional participation.

In this section, the various components of the CNRM-ESM2-1 physical core are briefly described in terms of grids and key characteristics.

The atmosphere component is based on Version 6.3 of the global spectral model ARPEGE-Climat (ARPEGE-Climat_v6.3). The atmospheric physics and dynamics are solved on a T127 triangular grid truncation that offers a spatial resolution of about 150 km in both longitude and latitude. Consistently to CNRM-CM6-1, CNRM-ESM2-1 employs a "high-top" configuration with 91 vertical levels that extend from the surface to 0.01 hPa in the mesosphere; 15 hybrid σ-pressure levels are available below 1500 m. The dynamical core and the physical component of the model are identical to those employed in CNRM-CM6-1. In particular, they use the same calibration. The reader is referred to Voldoire et al. (2019) for further details.

To simulate surface state variables and fluxes at the surface-atmosphere interface, CNRM-ESM2-1 uses the SURFace EXternalisée modeling platform Version 8.0 over the same grid and with the same time step as the atmosphere model. SURFEXv8.0 encompasses several submodules for modeling the interactions between the atmosphere, the ocean, the lakes and the land surface. Similarly to CNRM-CM6-1, CNRM-ESM2-1 employs the Exchange Coefficients from Unified Multi-campaigns Estimates scheme and the FLAKE model revisited by Le Moigne et al. (2016) to simulate surface fluxes over oceans and lakes, respectively. Over the land surface, both CNRM-CM6-1 and CNRM-ESM2-1 use the Interaction Soil-Biosphere-Atmosphere (ISBA) land surface model coupled to the CNRM version of the Total Runoff Integrating Pathways (CTRIP) river routing model to solve energy and water budgets at the land surface, as well as to simulate river discharge. ISBA explicitly solves the continental hydrological cycle accounting for snow, canopy interception, floodplains, liquid and solid soil moisture, unconfined aquifers, and upward capillarity fluxes into the superficial soil. Plant transpiration is controlled by stomatal conductance of leaves which has been adapted to ISBA from following the Jacobs et al.'s (1996) formulation (Calvet et al., 1998). However, in the configuration of ISBA-CTRIP as used in CNRM-CM6-1, the leaf area index (LAI) is not calculated as the result of the carbon balance of the leaves but prescribed from climatological ECOCLIMAP data (Faroux et al., 2013; Masson et al., 2003), involving that only the CO_2 effect on stomatal closure is represented (called the "antitranspiration" effect of CO_2). There are no land cover changes in CNRM-CM6-1, and the land cover distribution is fixed in time according to the ECOCLIMAP database (Table 2). This database includes climatological observations at high resolution over the 2000s, such as LAI, vegetation roughness length, snow-free land surface albedo (Carrer et al., 2014), or soil textural properties, from the Harmonized World Soil Database at a 1-km resolution (HWSD, 2012). More details on the physical processes represented in the ISBA-CTRIP system can be found in Decharme et al. (2019).

The ocean component of CNRM-ESM2-1 is the Nucleus for European Models of the Ocean (NEMO) Version 3.6 (Madec et al., 2017) which is coupled to both the Global Experimental Leads and ice for ATmosphere and Ocean (GELATO) sea ice model (Salas Mélia, 2002) Version 6 and also the marine biogeochemical model Pelagic Interaction Scheme for Carbon and Ecosystem Studies version 2-gas (PISCESv2-gas detailed in section 2.5). NEMOv3.6 operates on the eORCA1L75 grid (Mathiot et al., 2017) which offers a nominal resolution of 1° to which a latitudinal grid refinement of (1/3)° is added in the tropics; this grid describes 75 ocean vertical layers using a vertical z*-coordinate with partial step bathymetry formulation (Bernard et al., 2006). The ocean layers are distributed unevenly as a function of depth with a resolution of 1 m at ocean surface to 200 m below 4000 m.

2.1.2. Earth System Processes Represented in CNRM-ESM2-1

This section focuses on Earth system processes and the biophysical couplings represented within the physical component of CNRM-ESM2-1 and CNRM-CM6-1. In the following, we detail component by component where Earth system processes or biophysical couplings differ between CNRM-ESM2-1 and CNRM-CM6-1. These latter are summarized in Table 2.

In atmospheric physics, key differences between CNRM-ESM2-1 and CNRM-CM6-1 arise from the use of interactive atmospheric chemistry and aerosols (see sections 2.2 and 2.3 for further details). In CNRM-ESM2-1, the 3-D concentrations of aerosols and of a number of trace gases, including CO_2, interact with the atmospheric radiative code at each call of the radiative scheme, for the longwave part of the spectrum (aerosols, H_2O, CO_2, O_3, CH_4, N_2O, CFC11, and CFC12) and for its shortwave counterpart (aerosols, O_3, H_2O and CO_2). This enables the representation of aerosol-radiation and chemistry-radiation interactions as well as the interactions between climate and aerosols (Table 2).

Table 2
Overview of the Earth System Processes Represented in CNRM-CM6-1 and CNRM-ESM2-1

	Represented Earth system processes						
	Vegetation-radiation [a]	Vegetation-hydrology [b]	Vegetation-dust [c]	Marine biota-radiation [d]	Aerosol-radiation [e]	Climate-aerosols [f]	Chemistry-radiation [g]
CNRM-CM6-1	Derived from a monthly climatology of observed LAI	Derived from a monthly climatology of observed LAI		Derived from a monthly climatology of observed surface chlorophyll	Derived from a monthly aerosols optical depth climatology varying each year	Derived from a monthly aerosols optical depth climatology varying each year	Global mean annual concentrations of radiatively active gases
CNRM-ESM2-1							

Note. The green shading denotes that Earth system processes are represented (see sections 2.1.2, 2.2, 2.3, 2.4, 2.5, and 2.6). The yellow shading indicates that the interaction is derived using a semi-offline approach, that is from a previous model simulation or an offline computation. The orange shading highlights the use of prescribed boundary condition that varies each year if not specified otherwise. The red shading indicates where an Earth system process is missing or kept the same as in the preindustrial control simulation. [a] denotes variations in surface albedo; [b] denotes variations vegetation transpiration or vegetation water stress; [c] denotes how vegetation cover influence the dust emissions; [d] denotes the use of the influence of ocean chlorophyll on radiative transfer; [e] denotes the coupling between aerosols and radiation (direct and first indirect aerosol effects); [f] denotes how climate variations may influence the emissions of dust and sea-salt aerosols; [g] denotes how radiative active species such as ozone and methane will interact with radiation pending on atmosphere dynamics (e.g., variations of the tropopause height).

Over the land surface, key differences represented processes between CNRM-ESM2-1 and CNRM-CM6-1 which arise from the representation of both vegetation phenology and land cover changes (Table 2). Conversely to CNRM-CM6-1, the vegetation in CNRM-ESM2-1 responds to environmental variations. It accounts for both CO_2 effect on stomatal closure and the CO_2 fertilization on vegetation biomass. As a consequence, the LAI of vegetation in CNRM-ESM2-1 results from the carbon balance of the leaves (section 2.4). These ecophysiological processes enable the representation of vegetation-radiation and vegetation-hydrological interactions (Table 2). Land cover changes are prescribed in CNRM-ESM2-1 following CMIP6 standard, enabling the representation of interactions between the dust emission scheme (depending on bare soil fraction) and the land cover distribution (summarized as "vegetation-dust" in Table 2). It also plays a role in the vegetation-radiation interactions by modifying the reflective characteristics of land surfaces (Table 2). Further details about land cover changes are detailed below (section 2.5).

Finally, in the ocean, CNRM-ESM2-1 uses the same suite of ocean physical schemes as in CNRM-CM6-1, except from the representation of marine biota-radiation interactions (Table 2). Indeed, the main difference in the ocean component of CNRM-ESM2-1 with respect to CNRM-CM6-1 arises from the use of the ocean biogeochemical model PISCESv2-gas (detailed in section 2.6), which resolves the interaction between the marine phytoplankton and the penetration of downwelling shortwave radiation (Table 2). In this scheme, the radiative transfer in the water column is resolved using a chlorophyll-dependent three-wave band scheme as described in Lengaigne et al. (2007) and Mignot et al. (2013). As explained in Voldoire et al. (2019), CNRM-CM6-1 uses a 12-month climatology of surface chlorophyll derived from a former NEMO-PISCES simulation performed at 25 km and forced by atmospheric reanalyses (Lee et al., 2016) to estimate the modulation of the solar warming rate by phytoplankton. In CNRM-ESM2-1, PISCESv2-gas (see section 2.6) enables the representation of the phytoplankton-light feedback in CNRM-ESM2-1 because the chlorophyll concentrations of the phytoplankton intervene in the computation of the solar warming rate by modulating the amount of downwelling solar radiation across the water column (see Supplementary Materials).

2.1.3. Coupling and Outputs

CNRM-ESM2-1 exploits the full capabilities of the OASIS3-MCT software (Craig et al., 2017), which allows the exchange of 31 physical and 4 biogeochemical fields across the various model components (Figure 1). In the CNRM-CERFACS climate models such as CNRM-ESM2-1, the coupling is implemented in SURFEX, NEMO, and CTRIP. The generic coupling interface implemented in SURFEX is detailed in Voldoire et al. (2017).

CNRM-ESM2-1 is also interfaced with XIOS (Meurdesoif, 2018) which is an Input/Output parallel server software allowing for a declarative description of output files content and for the realization of online calculation on geophysical fields.

2.2. Atmospheric Chemistry

The atmospheric chemistry scheme of CNRM-ESM2-1 is Reactive Processes Ruling the Ozone Budget in the Stratosphere Version 2 (REPROBUS-C_v2), first implemented and evaluated in a former version of CNRM climate model (Michou et al., 2011), and more recently during the course of the Chemistry Climate Model Initiative (CCMI) research

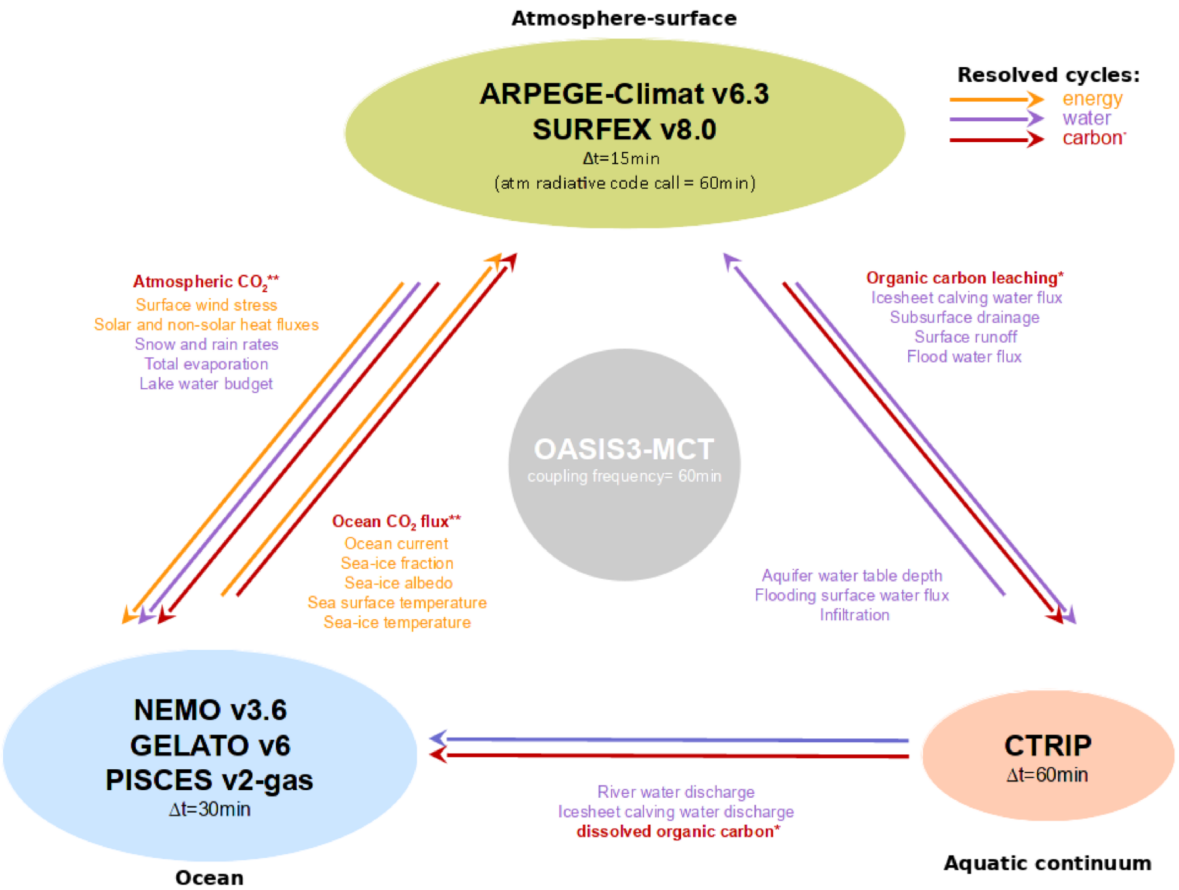

Figure 1. Overview of the coupling between CNRM-ESM2-1 components. t denotes model time step in minutes. Orange, blue, and red arrows give the direction of the exchange of energy, water, and biogeochemical fields between models. * denotes the biogeochemical fields that are used in all CNRM-ESM2-1 simulation, except in stand-alone configuration such as OMIP. ** denotes the biogeochemical fields that are used only in emission-driven simulations.

(e.g., Maycock, Matthes, et al., 2018; Maycock, Randel, et al., 2018; Morgenstern et al., 2017; Wales et al., 2018; Zhang et al., 2018). It is an "online" scheme whereby the chemistry routines are part of the physics of the atmospheric climate model and called at each time step of the physics. The scheme resolves the spatial distribution of 63 chemistry species but does not represent the low troposphere ozone non-methane hydrocarbon chemistry. Chemical evolution is computed down to the ad hoc level of 560 hPa (for details, see Michou et al. (2011) and Morgenstern et al. (2017)). Below this level, the concentrations of a number of species (i.e., N_2O, CH_4, CO, CO_2, CFC11, CFC12, CFC113, CCl4, CH_3CCl_3, CH_3Cl, HCFC22, CH_3Br, H1211, and H1301) are relaxed toward the yearly evolving global mean abundances set by the CMIP6 experiments (Malte Meinshausen et al., 2017); for other species, concentrations below the 560-hPa level are relaxed toward the 560-hPa value. Consistently with the relaxation, explicit emissions, dry deposition, washout, and parameterized transport (diffusion and convection) of the chemical fields are not considered.

The main differences between the current and the Michou et al. (2011) versions of the chemistry scheme consist of the following: (a) Kinetics and photolysis rates are now those of Sander et al. (2011), (b) monthly distributions of stratospheric sulfate aerosols are, on the basis of the study of Thomason et al. (2018), those of CMIP6, as is the solar information that modulates the photolysis rates (Matthes et al., 2017), (c) photolysis rates are no longer modified according to cloudiness, (d) a different processing between the surface and the 560-hPa level as detailed above, and (e) the vertical extension of the chemistry scheme that goes with that of the climate model (91 model levels from the surface into the mesosphere, up to about 80 km). This did not require any specific adjustment except for the relaxation of H_2O performed over the first seven levels of the model (below 0.5 hPa, toward 6.5 ppmv). Forty-four chemical variables are transported by the large-scale advection scheme of CNRM-ESM2-1, as the meteorological variables.

To shed light on this intercomparison exercise between CNRM-CM6-1 and CNRM-ESM2-1, one has to note that the CNRM-CM6-1 chemistry consists, firstly, of a simple parameterization of the ozone production rate which is a linear function of the ozone mixing ratio, the temperature, and the partial ozone column above the point considered (Table 2, see also Voldoire et al. (2019) for further details). All coefficients of this linear function had been computed from simulations performed with the atmospheric component of CNRM-ESM2-1 using the CMIP6 *historical* forcings over the years 1950–2014 (an ensemble of three realizations was performed), and the CMIP6 projected forcings from 2015 to 2100. Coefficients are time-varying monthly averages after 1950 and kept at the 1950 values beforehand. Therefore, by construction, the ozone concentrations of CNRM-CM6-1 should be close to those of CNRM-ESM2-1. Second, a simple parameterization of the upper-stratospheric source of water vapor due to methane oxidation is implemented in CNRM-CM6-1 (European Centre for Medium-Range Weather Forecast, 2014).

2.3. Tropospheric Aerosols

CNRM-ESM2-1 includes an interactive tropospheric aerosol scheme included in the atmospheric component ARPEGE-Climat. This aerosol scheme, named Tropospheric Aerosols for ClimaTe In CNRM (TACTIC_v2), represents the main anthropogenic and natural aerosol species of the troposphere. Originally developed in the European Centre for Medium-Range Weather Forecast Integrated Forecasting System as presented in Morcrette et al. (2009), this scheme has been adapted to the ARPEGE/ALADIN-climat code (Michou et al., 2015; Nabat et al., 2015). It is based on a sectional representation of desert dust (three size bins whose limits are 0.01, 1.0, 2.5, and 20 μm), sea-salt (three bins whose limits are 0.03, 0.5, 5.0, and 20.0 μm), sulfate (one bin), organic matter (two bins), and black carbon (two bins). The separation in two bins for organic matter and black carbon allows us to distinguish hydrophilic and hydrophobic particles. An additional prognostic variable is added to represent sulfate precursors considered as sulfur dioxide (SO_2). Sulfate precursors evolve in sulfate aerosols through a simple equation depending on latitude. All these 12 species are prognostic variables in the model, affected by transport (semi-lagrangian advection, turbulent and convective transport through the atmospheric convection scheme), dry deposition, and in-cloud and sub-cloud scavenging.

Natural emissions are calculated online as a function of surface wind and soil characteristics (Kok, 2011; Marticorena & Bergametti, 1995) for desert dust particles and as a function of surface wind and sea surface temperature (Grythe et al., 2014; Jaeglé et al., 2011) for sea-salt particles. The dust emission scheme uses soil textures, bare soil fraction, surface roughness length, and superficial soil moisture provided by the land surface module in SURFEX. Dimethylsulfide (DMS) emissions are also taken into account through the climatology of (Kettle et al., 1999), as well as volcanic sulfur emissions. Anthropogenic and biomass burning emissions come from official CMIP6 inventories, respectively provided by van Marle et al. (2017) and Hoesly et al. (2018). All these aerosols interact with shortwave and longwave radiation, through optical properties (extinction coefficient, single scattering albedo and asymmetry parameter) calculated using the Mie theory. Sulfate, organic matter, and sea-salt concentrations are used to determine the cloud droplet number concentration following Menon et al. (2002), thus representing the cloud albedo effect (first aerosol indirect effect).

The inclusion of this interactive aerosol scheme in CNRM-ESM2-1 is one of the main differences with CNRM-CM6-1 (Table 2). In the latter, aerosols are prescribed through monthly aerosol optical depth (AOD) fields varying each year (Voldoire et al., 2019), coming from atmosphere-only type simulations using the TACTIC_v2 scheme and the same emissions as CNRM-ESM2-1. Here, interactive aerosols enable the representation of Earth system feedbacks such as changes in natural aerosol emissions (i.e., dust and sea-salt) with climate change.

2.4. Land Carbon Cycle

Land carbon cycle and vegetation-climate interactions in CNRM-ESM2-1 are simulated with the ISBA scheme embedded in the SURFEXv8.0. ISBA simulates plant physiology, carbon allocation and turnover, and carbon cycling through litter and soil as detailed in Calvet et al. (1998) and Gibelin et al. (2006, 2008). The main characteristics of the land carbon cycle module are described below.

Vegetation in ISBA is represented by six biomass pools (leaves, stem/twigs, wood, fine and coarse roots, and a storage of nonstructural carbohydrates) (Gibelin et al., 2008). Vegetation biomass is simulated interactively

based on the carbon assimilated by photosynthesis and released by turnover and respiration. Vegetation biomass is also influenced by natural disturbances such as natural fires which are simulated interactively by ISBA. The carbon balance of the leaves controls the vegetation phenology and the LAI as detailed in Gibelin et al. (2006).

The litter and soil organic matter module derives from the CENTURY soil carbon model (Parton et al., 1988). It includes four litter carbon pools which differ between each other by their location (above- or below-ground), presumed chemical composition, and potential decomposition rates (or turnover times). The three soil organic matter reservoirs (active, slow, and passive) are characterized by their resistance to decomposition with turnover times spanning from a few months for the active pool to 240 years for the passive pool.

Compared to the version used in CNRM-ESM 1, key improvements have been done in ISBA as used in CNRM-ESM2-1; they relate to the assimilation and autotrophic respiration processes used in the vegetation physiology scheme. In particular, the structural parameters of the photosynthetic scheme such as the mesophyll conductance, the maximum photosynthetic rate, and the leaf carbon-to-nitrogen ratio have been calibrated on the TRY database (Kattge et al., 2011). The autotrophic respiration scheme has been revised following Joetzjer et al. (2015) which scale leaf to canopy respiration by using a vertical exponential profile of leaf nitrogen as suggested by Bonan et al. (2012). Finally, in the absence of nitrogen cycling within the vegetation, an implicit nitrogen limitation scheme has been implemented in ISBA following the meta-analysis of Yin (2002). Leaf nitrogen concentration per unit mass decreases with increasing CO_2, which results in a decrease in specific leaf area (SLA) with increasing CO_2 concentration because ISBA linearly relates SLA to leaf nitrogen concentration per unit mass (Gibelin et al., 2006). This decrease in SLA limits leaves growth and LAI and indirectly reduces assimilation of atmospheric CO_2.

While this empiric relationship does not aim at replacing a fully resolved nitrogen cycle, this implicit nitrogen limitation parameterization is assumed to capture the vegetation response to nutrient limitation under rising CO_2 (Yin, 2002).

Other key differences arise from the fact that ISBA includes both natural and anthropogenic disturbances. The considered natural disturbances are wildfires and flooding that affect litter and soil organic carbon leaching. Both processes impact the net ecosystem carbon balance and are relevant for biomes and climate studies. In CNRM-ESM2-1, the soil carbon leaching scheme as simulated by ISBA-CTRIP is coupled to PISCESv2-gas (see section 2.4). Yet, this model version only handles the transport of dissolved organic carbon (DOC) through the aquatic continuum as simulated by CTRIP. Thus, CTRIP does not include other carbon-related chemical species such as dissolved inorganic carbon which would enable the computation of air-water carbon exchange. As a consequence, the carbon cycle as simulated in CNRM-ESM2-1 is not entirely bounded.

2.5. Land Cover Change

The land cover changes are the only anthropogenic disturbances represented in ISBA. This means that land use processes (i.e., harvest of crop and wood, nitrogen fertilization, or irrigation) are not simulated in ISBA.

These changes are prescribed in ISBA by yearly net changes in land cover. The net land cover changes are derived from the Land Use Harmonized (LUH, Hurtt et al., 2006) Version 2.0 h data set (http://luh.umd.edu/data.shtml) and the modern distribution of the 16 living plant functional types (see Table S2) and 3 non-living types (bare soil, permanent ice, and rocks) as given in ECOCLIMAP (Faroux et al., 2013; Masson et al., 2003). The yearly changes in land cover distribution in CNRM-ESM2-1 drive changes in the rate of dust emissions because the aerosol scheme uses the fraction of bare soil to compute the amount of dust that can be emitted from the ground (Table 2).

2.6. Marine Biogeochemistry

The biogeochemical component of CNRM-ESM2-1 uses the Pelagic Interactions Scheme for Carbon and Ecosystem Studies Volume 2 version trace gases (PISCESv2-gas), which derives from PISCESv2 as described in Aumont et al. (2015).

Within the ocean interior, PISCESv2-gas resolves the evolution of 26 compartments which enables the resolution of oxygen, carbon, sulfur, and nutrients on the NEMO grid.

Common key characteristics of PISCESv2-gas and PISCESv2 are described in the following. PISCESv2-gas simulates the distribution of five nutrients (from macronutrients nitrate, ammonium, phosphate, and silicate to micronutrient iron) which regulate the growth of two explicit phytoplankton classes (nanophytoplankton and diatoms). In CNRM-ESM2-1, PISCESv2 uses the complex iron chemistry of Tagliabue and Völker (2011). This formulation of iron chemistry employs on two ligands and five iron forms. Diatoms differ from nanophytoplankton because they need silicon and more iron (Sunda & Huntsman, 1997) and because they have higher half-saturation constants due to their larger mean size. Phytoplankton growth is also limited by light. Redfield ratios between carbon, nitrate, and phosphate are assumed identical for all plankton classes (122:16:1, respectively; Takahashi et al. (1985)), while the internal concentrations of carbon, iron, chlorophyll, and silicon (for diatoms only) are represented in phytoplankton biomasses. Their evolution follows a mixed Monod-Quota approach as detailed in Aumont et al. (2015), except for phytoplankton chlorophyll concentration which follows the formulation of Geider et al. (1998). Two zooplankton groups (microzooplankton and mesozooplankton) interact with the two phytoplankton groups, with each other, and with the organic carbon pools (see below). Compared to phytoplankton, only the total carbon biomass is modeled for these two zooplanktons. As a consequence, the ratios between carbon, nitrogen, phosphate, and dioxygen are fixed in time and space and are set to the Redfields ratio as published by Takahashi et al. (1985): 122/16/1 for carbon/nitrogen/phosphate and the oxygen-to-carbon ratio is set to 1.34 following Körtzinger et al. (2001). The iron to carbon ratio is also constant and set to 10 μmol Fe/mol C. PISCESv2-gas resolves the evolution of semi-labile dissolved organic matter (characterized by a lifetime between 1 month and a few years), small (1–100 μm) and large (100–5000 μm) sinking particles. The internal concentrations in carbon, nitrogen, and phosphate within these pools of organic carbon are derived from Redfield ratios fixed in time and space whereas that of iron, silicon, and calcite pools are resolved explicitly.

In addition to these compartments, PISCESv2-gas resolves the evolution of dissolved inorganic carbon, total alkalinity (Alk), dissolved oxygen, DMS, and nitrous oxide across the water column.

The following suite of parameterizations is specific to the model set-up as used in CNRM-ESM2-1.

Dissolved inorganic carbon and Alk are involved in the computation of the carbonate chemistry, which is resolved by "model the ocean carbonate system" Version 2 (mocsy 2.0,Orr & Epitalon, 2015) in PISCESv2-gas. Mocsy 2.0 enables a better and faster resolution of the ocean carbonate chemistry at thermodynamic equilibria. Besides, calcium carbonate is assumed to exist only in the form of calcite. The production of calcite is prescribed according to a variable rain ratio which is a function of the mixed layer depth, temperature, and light. The dissolution of calcite depends on the local saturation state.

Oxygen is prognostically simulated using two different oxygen-to-carbon ratios, one when ammonium is converted to or mineralized from organic matter, the other when oxygen is consumed during nitrification. Their values have been set respectively to 131/122 and 32/122.

The distribution of oxygen is used to define the regions where oxic or anoxic degradation processes take place. It also influences the production of nitrous oxide (N_2O) within the ocean column because PISCESv2-gas uses the oxygen-dependent formulation of N_2O production of Jin and Gruber (2003). This formulation assumes an oxygen-dependent yield of N_2O, which also encompasses the denitrification and nitrification; both processes enhance the production of N_2O at low oxygen concentrations. This formulation also assumes a constant background yield presumed to represent the N_2O production by nitrification and a consumption of N_2O in suboxic conditions. Originally implemented by Martinez-Rey et al. (2015), this N_2O scheme has benefited from a recoding and an improved calibration. In PISCESv2-gas, the coefficients assigned to background and the oxygen-dependent yields are set to 1.1 10^{-4} mol N_2O mol O_2^{-1} and 30 10^{-4}, respectively. They are closer to those proposed by Jin and Gruber (2003). The consumption of N_2O is set of 7.12 10^{-4} d^{-1}, which is twice greater than the values used in Martinez-Rey et al. (2015), but within the range provided by Bianchi et al. (2012).

PISCESv2-gas simulates the distribution of DMS and dimethylsulfoniopropionate (DMSP) using a mechanistic scheme following Masotti et al. (2016). This scheme computes the particulate DMSP from the carbon biomass of the two phytoplankton groups using group-specific DMSP-to-carbon ratios. Once produced, particulate DMSP is instantaneously transformed into dissolved DMS by bacteria. The production of particulate DMSP by phytoplankton increases with phosphorus and iron limitation. This production also increases with

rising incoming solar radiation and rising ocean temperature following the formulation proposed by Vogt et al. (2010). Compared to Masotti et al. (2016), PISCESv2-gas includes a response of DMSP production to ocean acidity inferred from Six et al. (2013), which mimics the mean reduction of DMS concentration to rising ocean acidity as inferred from laboratory mesocosm experiments. The DMS consumption by bacteria is driven by light, nutrients (nitrogen, phosphorus, and iron) and DOC. In this version of PISCES, the photochemical loss of DMS is controlled by the amount of photosynthetically available radiation and not by the total irradiance as used in Masotti et al. (2016), which is consistent with observational studies such as Bouillon (2004) or Derevianko et al. (2009).

At ocean surface, PISCESv2-gas exchanges carbon, oxygen, DMS, and nitrous oxide (N_2O) tracers with the atmosphere using the revised air-sea exchange bulk as published by Wanninkhof (2014). Nonetheless, the exchange of carbon is fully resolved in a two-way mode in the emission-driven configuration of CNRM-ESM2-1 only.

At the bottom of the ocean, the exchange between the sediments and the ocean is treated differently between species. The burial of particulate organic carbon is determined using a formulation proposed by Dunne et al. (2007). The meta-model of Middelburg et al. (1996) is used to determine the fraction of degradation of the remaining organic matter that is due to denitrification. This latter is then used to estimate the magnitude of denitrification and oxic degradation fluxes at the sediment interface.

PISCESv2-gas uses several boundary conditions which represent the supply of nutrients from five different sources: atmospheric deposition, rivers, sediment mobilization, sea ice, and hydrothermal vents. PISCESv2-gas handles external nutrients inputs as PISCESv2. Yet, some exceptions are found for the treatment of the external nutrients supply as used in CNRM-ESM2-1. Dust depositions as used in CNRM-ESM2-1 are derived from a modern 1986–2005 climatology of dry and wet dust deposition as estimated from the aerosol scheme used in CNRM-ESM2-1 (see section 2.3 for further details). Riverine inputs are interactive in CNRM-ESM2-1 because the litter and soil carbon leaching in SURFEXv8.0 (see section 2.4 for further details) is routed as dissolved organic carbon in CTRIP and supplied to the oceans as organic carbon by rivers in PISCESv2-gas. Since only the routing of DOC is bounded in CNRM-ESM2-1, the supply of the other nutrients has been parameterized using the global average ratios of nitrogen-to-DOC (0.72), phosphorus-to-DOC (0.59), and silicon-to-DOC (0.15) from Mayorga et al. (2010) and the global average ratios of dissolved inorganic carbon-to-DOC (1.48) and Alk-to-DOC (1.11) from Ludwig et al. (1996). Finally, PISCESv2-gas as used in CNRM-ESM2-1 does not include iron supply from sea ice melting and hydrothermal vents as described in Aumont et al. (2015).

3. Model Setup for CMIP6 Experiments

Table 3 documents how external forcings are taken into account in CNRM-ESM2-1 and CNRM-CM6-1. The only exception that is not included in Table 3 is the ocean chlorophyll which is neither a boundary condition properly speaking nor an external forcing as recommended for CMIP6 (Eyring et al., 2016). Yet, we believe that this field is relevant in the context of this study because it is used by both models in different manners and it impacts the regional climate with a magnitude comparable to the radiative forcing of land cover change (e.g., Lengaigne et al., 2009; Mignot et al., 2013).

The CMIP6 specification requires each model to reach its equilibrium state before kicking off formal simulations. To obtain the initial conditions for CNRM-ESM2-1 preindustrial steady state at year 1850, we first initialize the various physical and biogeochemical components of the model as described below.

ARPEGE-Climat_v6.3 and SURFEXv8.0 were initialized from modern present state, except vegetation and soil carbon reservoirs which were set to zero. NEMOv3.6 and PISCESv2-gas were initialized from modern observed climatologies from the World Ocean Atlas 2013 observations for temperature (Locarnini et al., 2013), salinity (Zweng et al., 2013), oxygen (Garcia et al., 2014a), nutrients (Garcia et al., 2014b), and the Global Ocean Data Analysis Project Version 2 (GLODAPv2.0, Key et al., 2015; Lauvset et al., 2016; Olsen et al., 2016) for dissolved inorganic carbon and Alk. GELATOv6 was initialized using an analytical state of sea ice: the sea ice concentration was set to 100% and its surface temperature at −10 °C where sea surface temperature is at freezing point. The sea ice thickness was set to 2 m in the Arctic and 1 m in the Antarctic. The initial thickness of the snow layer upon sea ice was set to zero.

Table 3
Overview of the External Forcings Involving Model Boundary Conditions (i.e., Atmospheric Concentrations or Emissions) as Used by CNRM-CM6-1 and CNRM-ESM2-1

		CNRM-CM6-1	CNRM-ESM2-1
External forcing	CO_2	Annual global mean concentration	Calculated in emission-driven simulation (not investigated in this study)
	Well-mixed greenhouse gases	Annual global mean concentration	
	Ozone	Linear ozone scheme with monthly coefficients from an atmosphere-only CNRM-ESM2-1 simulation	
	Aerosols	Derived from a monthly aerosols optical depth climatology varying each year	
	Land use	Fixed in time to the 1990s land cover distribution	Prescribed net land cover change varying each year
	Natural*	Annual global mean for solar forcing; zonal monthly mean for volcanoes and aerosols	Annual global mean for solar forcing; zonal monthly mean for volcanoes and aerosols

Note. This table lists the climate forcings required to be changed from the preindustrial control run in order to set up and perform each CMIP6 experiment. The green shading denotes that forcing is taken into account and its evolution is fully interactive (see section 2.1.2). The yellow shading indicates that the forcing is derived using a semi-offline approach, that is from a previous model simulation or an offline computation. The orange shading highlights the use of prescribed boundary condition or forcing that varies each year if not specified otherwise. The red shading indicates where a forcing is missing or kept the same as in the preindustrial control simulation. *Natural forcing includes variations of solar incoming radiation and volcanic aerosol injections.

From these initial conditions, CNRM-ESM2-1 was spun-up as follows.

The land surfaces were spun-up using a sequential approach where SURFEXv8.0 was first run offline during 1000 years using the atmospheric fields taken from a preindustrial atmosphere-alone simulation with ARPEGE-Climat. For the atmospheric forcing, a sequence of 10 years is repeated continuously. The spin-up for land carbon reservoirs employs an acceleration scheme updating the wood growth, the litter, and soil carbon modules several times per model time step with constant incoming carbon fluxes and physical conditions, allowing the various reservoirs of carbon to fill up much faster. Consequently, soil carbon and wood reservoirs were respectively spun-up for 21800 and 1200 years.

The ocean biogeochemistry was also run using a sequential approach where the marine biogeochemical model PISCESv2-gas was run offline using the daily ocean and sea ice outputs of the last 20 years of the fully coupled preindustrial simulation of CNRM-CM6-1 (Voldoire et al., 2019). About 1500 years of offline spin-up were used to equilibrate deep ocean biogeochemical state variables of PISCES consistently with the recommendation of Séférian, Gehlen, et al. (2016).

With all physical and biogeochemical reservoirs at equilibrium, a fully coupled spin-up was performed with CNRM-ESM2-1 under preindustrial conditions (Table 3). This fully coupled spin-up lasted for about 900 years during which global mean concentrations of nutrients and Alk were restored to global mean observed concentrations. Finally, a 300-yearlong spin-up simulation has been achieved with CNRM-ESM2-1 in fully coupled mode with the land-ocean riverine carbon coupling.

4. Results and Discussions

4.1. Preindustrial Mean State and Model Equilibrium

In this section, we analyze the preindustrial steady state as simulated by CNRM-ESM2-1 in the CMIP6 preindustrial control (*piControl*) simulation.

The calibration strategy applied for CNRM-CM6-1 is described in Voldoire et al. (2019). The main objective was to prevent a drift of the global mean SST of the coupled system by targeting a net surface energy balance on the ocean surface close to 0 W m^2 after a spin-up phase. As CNRM-ESM2-1 and CNRM-CM6-1 share the same physical core, and given the close distribution of aerosol and ozone forcings, no additional tuning was carried out for CNRM-ESM2-1. It allows a better traceability between the two versions.

Figure 2 shows an overview of key climate metrics tracking the level of equilibrium of CNRM-ESM2-1. The global mean top of the atmosphere (TOA) net radiative balance and global mean net surface heat flux document the global energy cycle as simulated by CNRM-ESM2-1 over the 500-yearlong preindustrial simulation. The global land water storage and the sea surface salinity are used to characterize the global hydrological cycle over land masses and over the oceans. The Northern Hemisphere and Southern Hemisphere sea ice volume (NIV, SIV, respectively) are global metrics for the cryosphere as resolved in CNRM-ESM2-1. The global land and ocean carbon fluxes and stocks are used to track the level of equilibration of the global carbon cycle. Finally, global mean temperature (GMT) and global average ocean surface temperature (OST) are provided as a qualitative metrics to assess the stability of preindustrial temperature as given by CNRM-ESM2-1 and to document potential drift of the model in terms of simulated GMT and OST.

All these metrics indicate that CNRM-ESM2-1 has reached a satisfying global equilibrium after the 1100-yearlong spin-up, although Figure 2a shows a slight mismatch between TOA net radiative balance and net surface heat flux. This difference is of about 0.68 W m^{-2} in average over the 500 years of the piControl simulation. This mean mismatch has been substantially reduced compared to CNRM-ESM 1 (about 2.7 W m^{-2}; Séférian, Delire, et al. (2016)). The long-term trend for both net radiative fluxes is 0.01 W m^{-2} century which is comparable to that of CNRM-CM6-1 (Voldoire et al., 2019) but four times smaller than of CNRM-ESM 1.

The hydrological cycle global scale metrics (Figure 2bc) indicate almost no drift for sea surface salinity, NIV, and SIV, with drifts smaller than 10^{-5} units per century or 10^{-5} 10^6 km^2 per century. The only exception is land water storage, with a drift of about 10^{-3} Yt per century, slightly greater than the other hydrological cycle global scale metrics. It may be explained by the treatment of ice sheets in CNRM-ESM2-1 which would require a longer spin-up to reach equilibrium (~10 ky).

Land and ocean carbon fluxes have also reached a steady state after the model spin-up (Figure 2d). Long-term steady-state carbon fluxes between the atmosphere and land and ocean are about −0.009 PgC y and 0.79 PgCy averaged over the 500 years of the piControl simulation. The long-term drift of both land and ocean carbon fluxes is about -10^{-4} GtC y^{-1} per century which fits the recommendation of *C4MIP* (Jones et al., 2016).

Figure 2d shows that CNRM-ESM2-1 does not simulate a net carbon imbalance close to zero, although the mean preindustrial ocean carbon outgassing is consistent with the published estimates of Resplandy et al. (2018). This net carbon imbalance is explained by the fact that PISCESv2-gas considers the riverine inputs of inorganic and organic carbon whereas in ISBA-CTRIP only represents the export of DOC. The export of dissolved inorganic carbon, particulate organic and inorganic carbon, and calcium carbonate is assumed based on observed ratios between these species and DOC at river mouths. We would like to stress that the magnitude of this net carbon imbalance remains in the range of the known uncertainty on the current global carbon budget depicted by the magnitude of the budget imbalance (±1.0 PgC y) as given in Le Quéré et al. (2018).

Figure 2e gives another view of the equilibration of the global carbon cycle by showing the land and ocean carbon stocks in CNRM-ESM2-1. This Figure shows that stocks of carbon over land and in the first 100 m of the ocean have reached an equilibrium, whereas the total ocean stock of inorganic carbon still drifts over the 500 years of the piControl simulation with a rate of 0.47 PgC y, that is, 0.6% of the total ocean mass dissolved inorganic carbon (Figure 2e).

Our analyses show that the drift in the total ocean stock of inorganic carbon is mainly controlled by the riverine inputs of inorganic and organic carbon. Indeed, the amount of riverine carbon inputs (~1.68 PgC y) simulated by CNRM-ESM2-1 is too large compared to the current best estimate of riverine carbon export to the open ocean (~0.95 PgC y; Ciais et al., 2013). These latter are not balanced by the burial of inorganic carbon in the ocean sediment (~0.43 PgC y), leading to an accumulation of dissolved inorganic carbon of

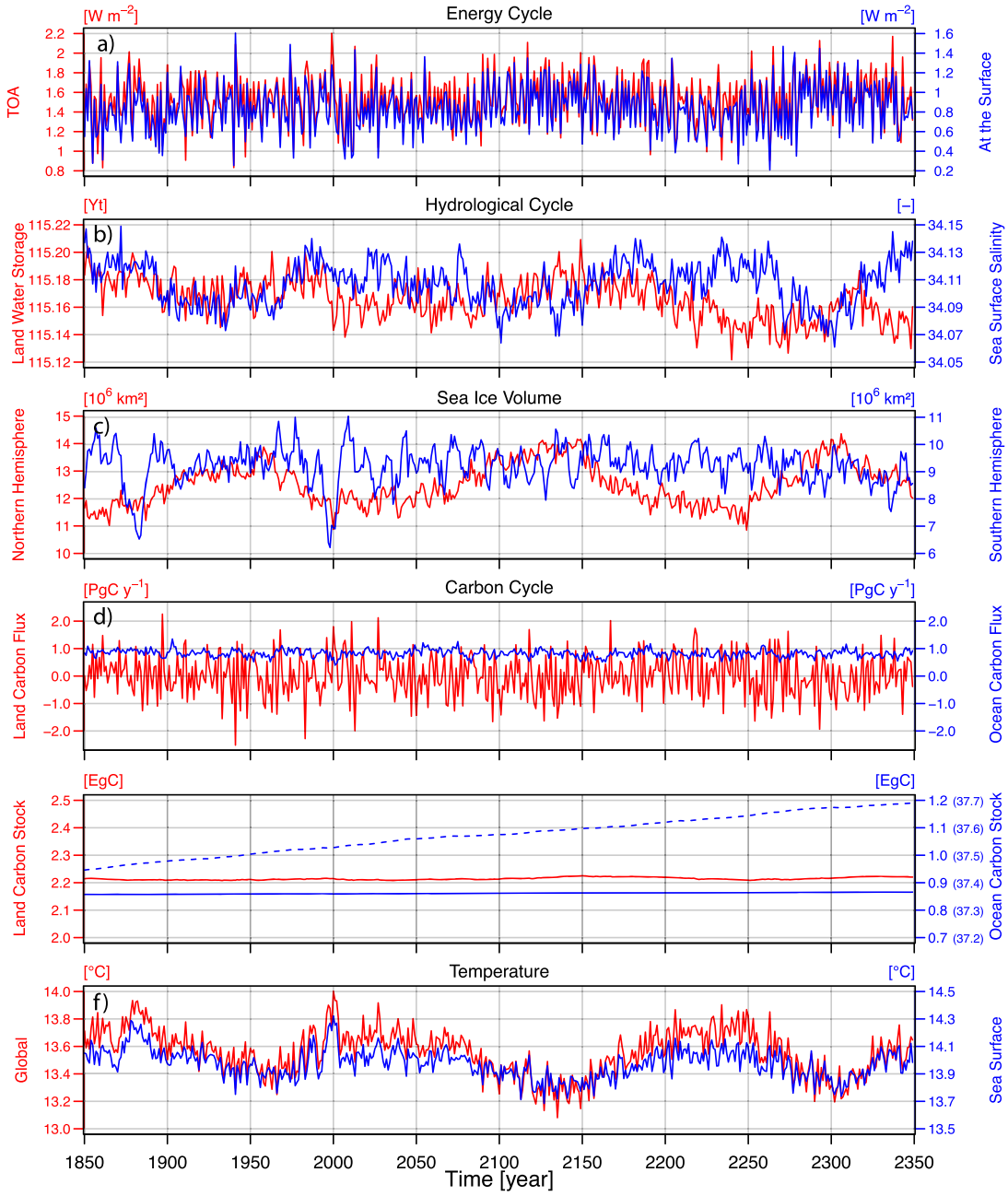

Figure 2. Overview of the various climate indices that are used to track the equilibration of CNRM-ESM2-1 along the 500-yearlong control simulation. (a) Net radiative fluxes at the top of the atmosphere (in red, left *y*-axis) and the net heat flux at surface (in blue, right *y*-axis); (b) continental water storage (in red, left *y*-axis) and sea surface salinity (in blue, right *y*-axis); (c) sea ice volume in the Northern Hemisphere (in red, left *y*-axis) and in the Southern Hemisphere (in blue, right *y*-axis); (d) global carbon fluxes over land (in red, left *y*-axis) and over ocean (in blue, right *y*-axis); (e) global carbon stocks over land (in red, left *y*-axis) and in the ocean (in blue, right *y*-axis); and (f) near-surface global average temperature (in red, left *y*-axis) and global averaged sea surface temperature (in blue, right *y*-axis). For carbon fluxes, negative (positive) fluxes indicate an uptake (outgassing) of CO_2 by land or ocean. The land carbon stock considers the vegetation biomass and the soil carbon content. The ocean carbon stocks represent the content of dissolved inorganic carbon in the first 100 m of the ocean (solid line) and the total ocean content of dissolved inorganic carbon across the water column (dashed lines, units are given in the right in brackets).

about 0.47 PgC y (Figure 2e). A longer spin-up simulation in boundless carbon cycle mode would have reduced the magnitude of the drift but would have increased the total ocean stock of inorganic carbon.

Finally, GMT and OST have also reached a steady state (Figure 2f). GMT is about 14 °C in average over the 500 years of *piControl*. OST is slightly cooler with 13.5 °C on average over the same period. They exhibit a

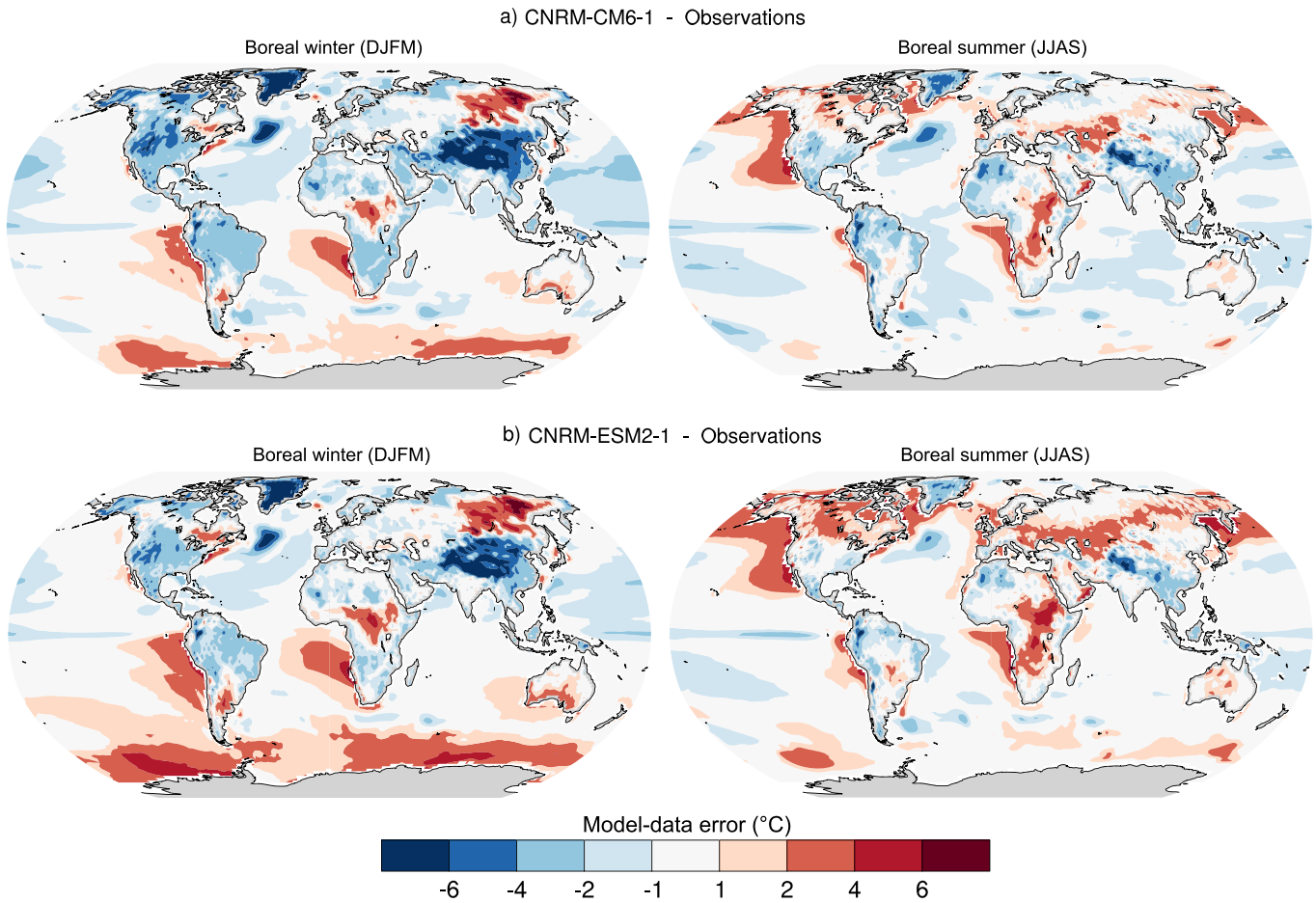

Figure 3. Departure in blended surface temperature as simulated by CNRM-CM6-1 (a, c) and CNRM-ESM2-1 (b, d) from observations averaged over 1981–2010. Blended surface temperature combines surface-air temperature over land and sea ice and sea surface temperature over ice-free sea water. Observations average several data sets: HadISST1 (Rayner, 2003) and ERSST v5 (Huang et al., 2017) over ice-free sea water; BEST (Muller, Curry, et al., 2013; Muller, Rohde, et al., 2013), CRU-TS4-00 (Harris et al., 2014), and GHCN-CAMS (Fan & van den Dool, 2008) over land and sea ice.

drift of $-0.3\ 10^{-6}$ °C per century and $-0.2\ 10^{-6}$ °C per century, respectively, which is consistent with those of CNRM-CM6-1 (Voldoire et al., 2019).

With this general overview, Figure 2 confirms that energy, hydrological, and carbon cycles simulated by CNRM-ESM2-1 have reached a steady state at the end of the spin-up simulation and are stable over the pre-industrial climate simulation.

4.2. Modern Climate Mean State

The performance of CNRM-ESM2-1 at reproducing modern observations is now evaluated using the results of the CMIP6 *historical* simulations. We compare CNRM-ESM2-1 skill against that of CNRM-CM6-1 to determine the level of similarity between both models. All calculations of the present section use an ensemble mean of five realizations of the CMIP6 *historical* performed with CNRM-ESM2-1. They are compared to ten realizations performed with CNRM-CM6-1. All the observational data sets are projected on the model grid using a bilinear interpolation.

4.2.1. Atmosphere

We start the modern climate mean state evaluation with the comparison of simulated blended surface temperature (Figure 3) and surface total precipitation (Figure 4) against observations.

Blended surface temperature consists in a combination of air surface temperature over land masses and sea surface temperature over oceans and has been recognized as the most suitable geophysical field to assess

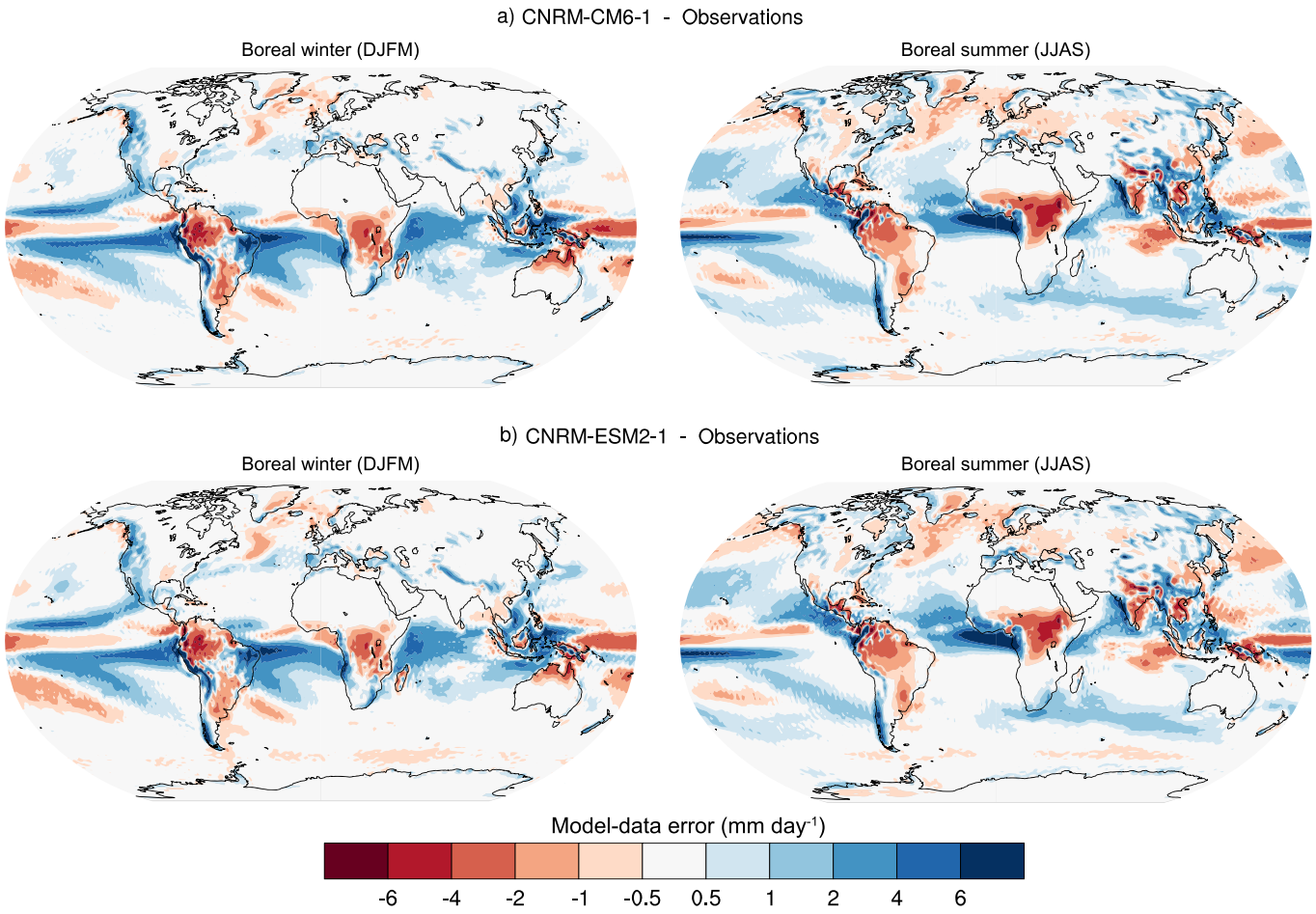

Figure 4. Departure in precipitation (PR) as simulated by CNRM-CM6-1 (a, c) and CNRM-ESM2-1 (b, d) from observations averaged over 1981–2010. Observations average several data sets: GPCC (Schneider et al., 2014), GPCP-1.2 (Adler et al., 2003), MSWEP (Beck et al., 2017), and TRMM-L3-4B43-V7 (Huffman et al., 2007).

patterns of global warming over the recent years (e.g., Karl et al., 2015). Both CNRM-ESM2-1 and CNRM-CM6-1 are able to capture the geographical structure of the blended surface temperature, with regional absolute model-data errors generally smaller than 6 °C (Figure 3). Table 4 highlights that the pattern of model-data error is very similar between both models because the pattern correlation between CNRM-ESM2-1 and CNRM-CM6-1 model-data errors is higher than 0.97 in boreal winter (DJFM) and boreal summer (JJAS). Notwithstanding this level of similarity, both Figure 3 and Table 4 show that CNRM-ESM2-1 is slightly warmer than CNRM-CM6-1. Cold biases are weaker in CNRM-ESM2-1 than in CNRM-CM6-1. In contrast, the warm bias is greater in CNRM-ESM2-1 than CNRM-CM6-1. This occurs clearly over the oceans in the boreal winter (DJFM in Figure 3), especially in the Southern Ocean, and over the continents in boreal summer (JJAS Figure 3). Flato et al. (2013) explained that the warmer bias over Southern Ocean represents a commonly shared epistemic error across previous generations of climate models. Voldoire et al. (2019) show that this epistemic error has been reduced in CNRM-CM6-1 compared to CNRM-CM5 in the Southern Ocean, but it somehow increased again in CNRM-ESM2-1 (Figure 3). This warm bias is driven by a smaller aerosols burden over the Southern Ocean and a weaker masking effect of the aerosols in CNRM-ESM2-1 compared to CNRM-CM6-1 (see sections 4.2.3 and 4.3.3). Despite these large regional biases, global average bias and root-mean-squared error (rmse) are generally smaller for CNRM-ESM2-1 than for CNRM-CM6-1 (Table 4).

In addition to surface temperature, precipitation is an important geophysical field when tracking model performance (Flato et al., 2013; Knutti et al., 2013). It is also an important driver of the Earth system by its influence on the land carbon cycle (Huntzinger et al., 2017; Keenan et al., 2016; Miralles et al., 2019). Figure 4

Table 4
Skill Assessment Metrics (Bias and Root-Mean-Squared Error, mse) for CNRM-CM6-1 and CNRM-ESM2-1 as Derived From Model-Data Comparison

Realm	Variable	CNRM-CM6-1 bias	CNRM-CM6-1 rmse	CNRM-ESM2-1 bias	CNRM-ESM2-1 rmse	Correlation between spatial pattern of error
Atmosphere	Surface temperature DJFM [°C]	−0.64	2.04	−0.09	1.97	0.98
	Surface temperature JJAS [°C]	−0.37	1.47	0.15	1.49	0.97
	Precipitation DJFM [°C]	0.33	1.53	0.30	1.47	0.99
	Precipitation JJAS [°C]	0.31	1.63	0.28	1.56	0.98
Ocean	MLD_{max} [m]	−11.45	135.83	−14.33	127.13	0.95
Aerosols and chemistry	Total ozone column [DU]	1.70	12.00	−0.28	13.00	0.95
	AOD [-]	−0.058	0.095	−0.065	0.101	0.95
Land surface and vegetation	Bare soil Fraction [%]	2.89	14.42	0.21	17.40	0.77
	Cropland Fraction [%]	−1.95	13.11	−1.66	9.64	0.71
	LAI min [m^2/m^2]	0.10	0.28	−0.22	0.39	0.14
	LAI max [m^2/m^2]	0.85	0.60	1.04	0.64	0.30
Marine biology	Chlorophyll min [mgChl m^{-3}]	−0.14	0.44	−0.12	0.45	0.99
	Chlorophyll max[mgChl m^{-3}]	−0.06	1.25	0.26	1.27	0.89
Carbon cycle	Combined land and ocean carbon fluxes [gC m^{-2} y^{-1}]	25.15	43.34	−0.47	25.26	0.06

Note. Error pattern correlation is used as a traceability metrics to establish the degree of similarity between the geographical structure of model biases of CNRM-CM6-1 and CNRM-ESM2-1.

shows that CNRM-CM6-1 and CNRM-ESM2-1 exhibit the same geographical distribution of model-data error with spatial correlation >0.98 in boreal winter and boreal summer. In particular, both models strongly underestimate the precipitation over the continents in the tropics inducing model-data errors in simulated land carbon cycle (detailed in section 4.2.4). In these regions, it is interesting to note that the interactive vegetation used in CNRM-ESM2-1 does not amplify model-data error in simulated precipitation with respect to CNRM-CM6-1, which uses a prescribed climatology of modern LAI (hence nonresponsive to biases in precipitation).

4.2.2. Ocean

The annual maximum mixed layer depth is an important ocean geophysical field to evaluate in Earth system models because of its role in deep water masses formation, ocean ventilation and ocean heat, and carbon uptake (Ito et al., 2010; Levy, Bopp, et al., 2013; Sallée et al., 2012). Figure 5 displays the annual maximum mixed layer depth as modeled by CNRM-CM6-1 and CNRM-ESM2-1 and observed from Argo measurements (Holte et al., 2017). Overall, both models have a very similar behavior over the historical period. As noted in Voldoire et al. (2019) for CNRM-CM6-1, the main observed deep convection areas are located in the Labrador Sea and the Greenland-Iceland-Nordic Seas. They are reasonably well reproduced in both models, although with a predominant deep convection in the latter region. In the Southern Hemisphere, an intense and unobserved persistent polynia is modeled in the Indian sector of the Southern Ocean. This explains rmse above 100 m in both models, mean biases being comparable and modest (Table 4). Both models display a deep convection site in the Japan Sea, in agreement with past observations (Talley et al., 2003). Finally, intermediate convection is modeled at subpolar fronts, with an equatorward bias though. Despite the use of an interactive biophysical coupling in CNRM-ESM2-1 (see section 2.1), this high level of similarity between the two models is not surprising. Indeed, the differences in heat trapping due to phytoplankton is expected to be small over the modern period because of the high level of similarity between the prescribed chlorophyll climatology used in CNRM-CM6-1 and the interactive chlorophyll concentrations simulated by CNRM-ESM2-1 (see below for further details). In addition, the biological modulation of the solar heat penetration only affects a shallow surface layer (typically above 50 m depth) and therefore impacts marginally deeper mixed layers.

Table 5 shows modeled and estimated transports at key oceanic sections, namely, at Drake Passage which quantifies the Antarctic Circumpolar Current (ACC) transport, the Florida-Bahamas and Denmark Straits which contribute to both the North Atlantic gyre and overturning circulations, and the Indonesian throughflow which is the main heat exchange pathway from the Pacific to the Indian Ocean. Again, both models have very similar behaviors, with differences below 10% at all sections. In light of recent estimates, the

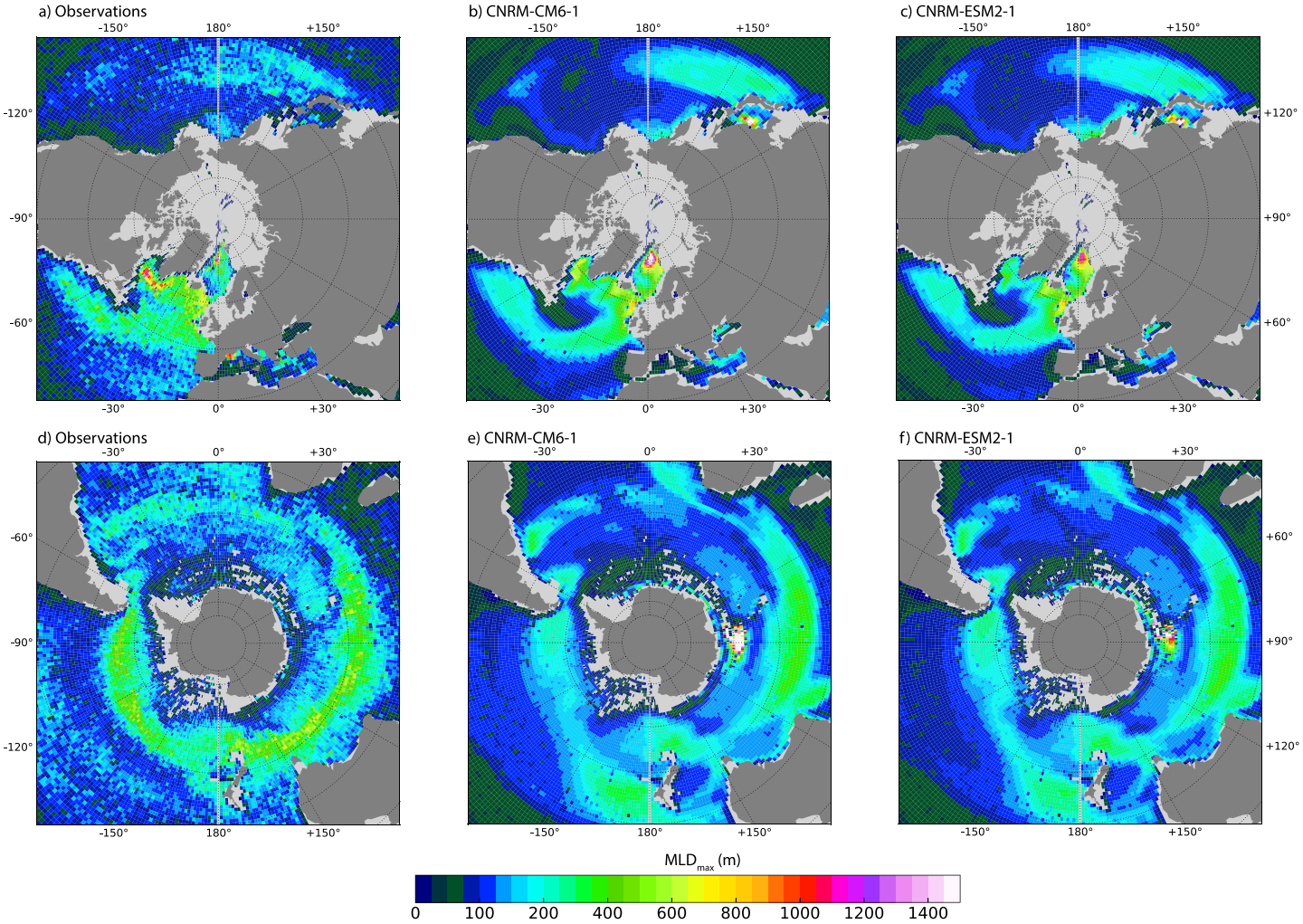

Figure 5. Annual maximum mixed layer depth (MLD_{max}) for (a, d) observations, (b) CNRM-CM6-1, and (c) CNRM-ESM2-1. Observed estimates are reconstructed from the 2004 to 2018 ARGO observations (Holte et al., 2017). Mixed layer depth is defined with the density threshold of 0.03 kg m^{-3} with respect to 10 m. The annual maximum of mixed layer depth is computed from monthly means. Model estimates are calculated from the ensemble mean historical over the 1981–2010 period; model outputs have been collocated in space and time with observations.

Drake Passage and therefore the Antarctic Circumpolar Current transport are largely underestimated by both models, which put them in the lower range of the CMIP5 ensemble (mean value of 155 ± 51 Sv, Meijers (2014)). Such a bias is likely related to underestimated meridional density gradients in the Southern Ocean (Olbers et al., 2004). The Denmark Strait transport is overestimated, consistently with a too large deep convection in the Greenland-Iceland-Nordic Seas (see Figure 5). The Florida-Bahamas Strait transport is larger by over 50% in models; however due to the low resolution, the Bahamas archipelago is not resolved so that the modeled western boundary transport also includes the Antilles Current East of the

Table 5
Various Estimates of the Mass Transport Across Major Ocean Sections (Expressed in Sverdrup, 1 Sv = 10^6 m^3 s^{-1})

Transect	Observed estimates	CNRM-CM6-1	CNRM-ESM2-1
Denmark Strait	−3.4 ± 1.4	−4.4 ± 1.0	−4.8 ± 1.0
Drake Passage	173.3 ± 10.7	108.8 ± 5.0	101.1 ± 4.4
Florida-Bahamas Strait	31.6 ± 2.1	50.4 ± 2.6	46.5 ± 3.0
Indonesian throughflow	−15 ± 3	−13.0 ± 2.0	−12.5 ± 1.8

Note. Observed estimates are based on the most up-to-date measurements as detailed in Griffies et al. (2016), except for the Drake Passage estimate which has recently been updated by Donohue et al. (2016).

Bahamas. Adding the measured 4.7 ± 7.5 Sv Antilles Current transport (Meinen et al., 2019) gives a reasonable modeled behavior, with a positive bias though. Lastly, the Indonesian throughflow transport is well represented by both models.

4.2.3. Atmospheric Chemistry

Figure 6 shows that the observed total ozone column is well reproduced by CNRM-CM6-1 and CNRM-ESM2-1 (see skill score metrics in Table 4). The total ozone column climatologies of CNRM-CM6-1 (Figure 6b) and CNRM-ESM2-1 (Figure 6c) compare well between each other. Both models represent correctly the observed latitudinal gradient. The observed contrast between the weak zonal variability of the columns in the tropics and the large-scale zonal variability elsewhere is also well modeled, with the correct location of the relative maximum in the high northern latitudes or in the 30–60°S band. Globally, the total ozone column simulated by CNRM-CM6-1 is slightly too high compared to NIWA-BSv3.3 (see http://www.bodekerscientific.com/data/total-column-ozone and Struthers et al. (2009)) with a global mean bias of about 1.70 DU, whereas CNRM-ESM2-1 exhibits a smaller negative bias of about−0.28 DU (Table 4). The geographical distribution of model-data error for both CNRM-CM6-1 and CNRM-ESM2-1, with too high columns in the tropical band and too low columns in the 30–60°N band, could be the signature of a weak Brewer Dobson circulation, although this is not supported by the excess of ozone in the 30–60°S band in CNRM-ESM2-1 and, to a lesser extent, in CNRM-CM6-1. A comprehensive analysis of the ozone in CNRM-CM6-1 and CNRM-ESM2-1 will be carried out in a forthcoming work.

4.2.4. Tropospheric Aerosols

Regarding the aerosols, CNRM-CM6-1 and CNRM-ESM2-1 share the same spatial patterns in average AOD at 550 nm (Figure 7, Table 4). Both models display high AOD in northern Africa due to mineral dust aerosols, in eastern Asia due to anthropogenic emissions, and over the Southern Ocean because of strong winds generating primary sea-salt particles. All these important aerosol loads are also present in satellite observations (MODIS data, Figure 7a).

For both CNRM-CM6-1 and CNRM-ESM2-1, the aerosol scheme has difficulties at reproducing the high AOD observed values in northern latitudes, especially over the boreal forests. This suggests that TACTIC_v2 underestimates the emissions of secondary organic aerosols. Besides, part of this model-data error over the western United States and Alaska is due to an overestimated wet scavenging in association to the excessive precipitation rate over this domain (Figure 4).

Concerning smoke aerosols emitted over the tropical region (Amazonia, Indonesia, and Central Africa), results confirm Petrenko et al.'s (2017) findings suggesting an underestimation of biomass burning emissions in the current emission database.

Besides, our analyses suggest that biases in precipitation impact the partition between dry and wet deposition of aerosols in several regions. This is the case over the Saharan Air Layer where the positive bias in JJAS precipitation in both models (Figure 4) enhances the wet deposition of dust through below-clouds scavenging. Similar conclusions were obtained over the Southeast Atlantic where the transport of significant smoke aerosol concentrations occurs (Zuidema et al., 2016). It should also be reminded that the differences observed in AOD could be due to uncertainties in the MODIS AOD retrievals (Gupta et al., 2018), parameterization of aerosol optical properties (especially changes with the relative humidity), altitude of injection as well as the atmospheric dynamics, precipitation, affecting the transport and as well as the dry and wet removal of aerosols.

4.2.5. Land Cover

Figure 8 highlights how far the land cover differs between the two models. Indeed, both models underestimate the fraction of bare soil compared to the European Space Agency Climate Change Initiative Land Cover (ESA-CCI-LC, Poulter et al., 2015)). The model-data error is however stronger in CNRM-ESM2-1 in most of the arid area and particularly in Arabia (Figure 8).

Differences in land cover representation between both models drive differences in land cover-aerosol interactions. Furthermore, land cover changes, considered in CNRM-ESM2-1 only, can lead to different aerosol emissions in CNRM-ESM2-1 with respect to CNRM-CM6-1. For instance, as the fraction of bare soil is essential in the dust emission parameterization in TACTIC_v2, dust emissions have been reduced in CNRM-ESM2-1 compared to CNRM-CM6-1 and result in a stronger underestimation of dust AOD in CNRM-ESM2-1.

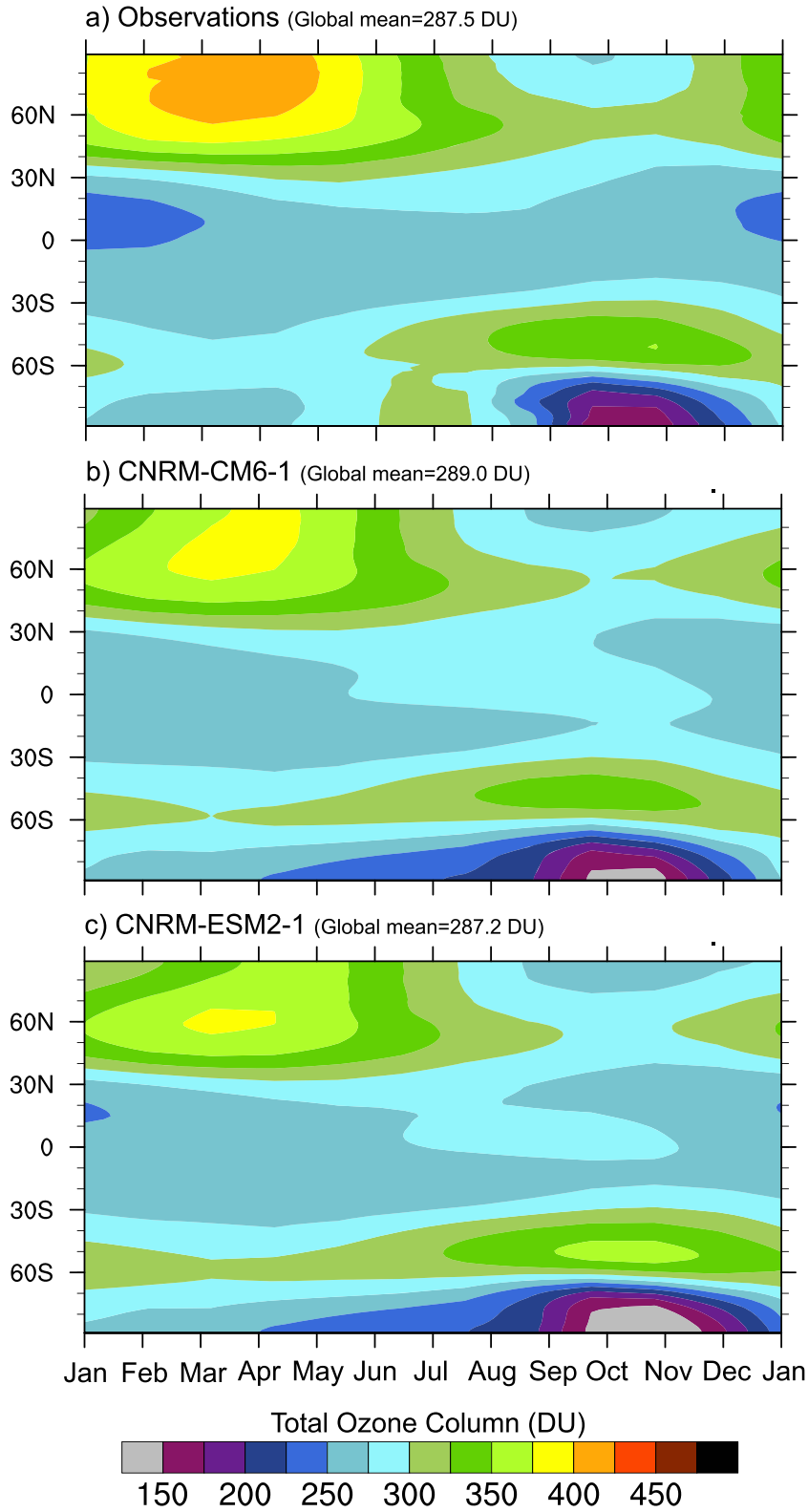

Figure 6. Mean annual cycle of the total ozone column in Dobson units (DU) presented as a month-latitude diagram in averaged over 1979–2014 for (a) observations (Bodeker et al., 2005, NIWA-BS Version 3.3 updated in 2018), (b) CNRM-CM6-1, and (c) CNRM-ESM2-1. The global annual mean are given in brackets.

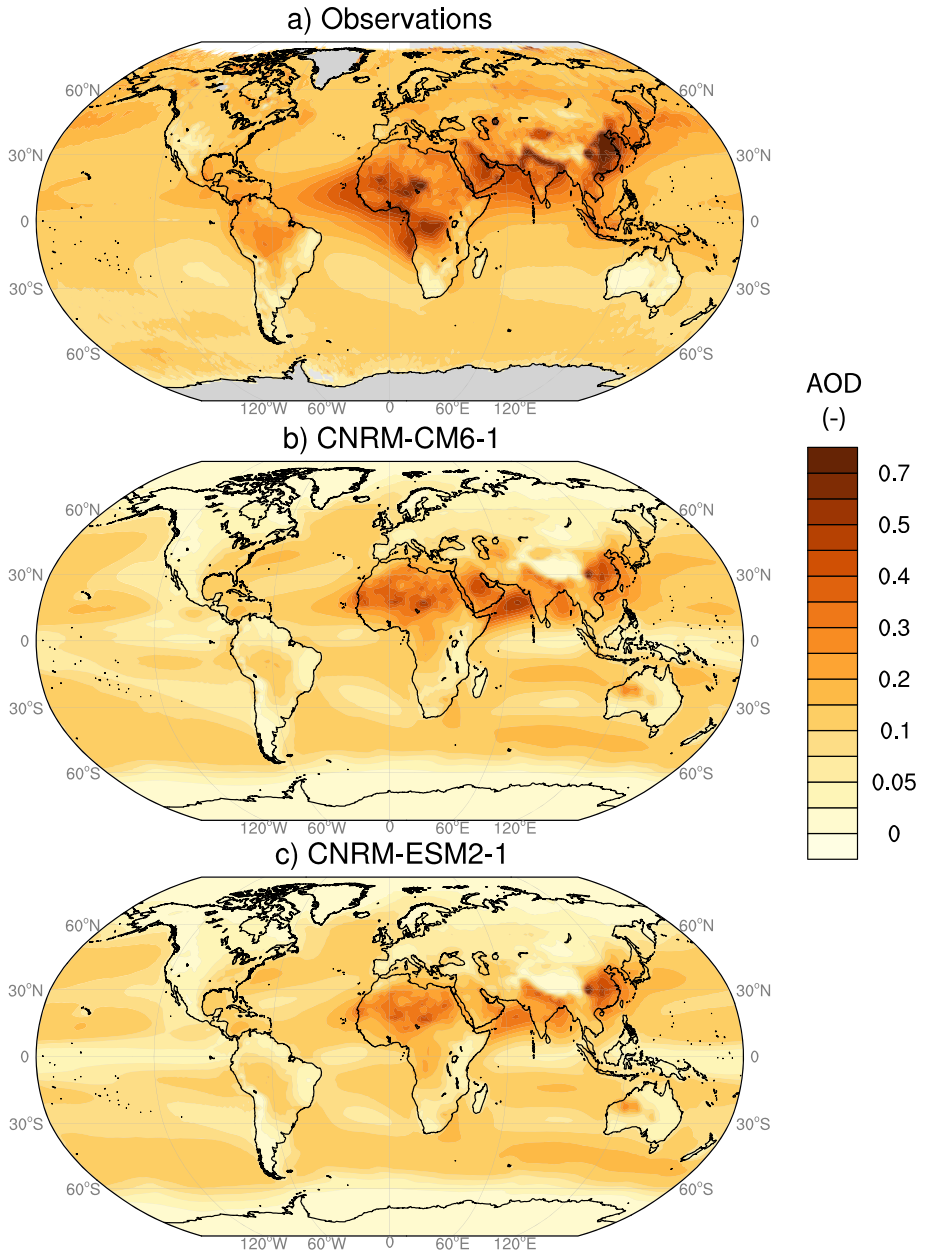

Figure 7. Mean aerosol optical depth (AOD) at 550 nm over the 2003–2014 period for (a) MODIS AQUA combined product (Levy, Bopp, et al., 2013), (b) CNRM-CM6-1 and (c) CNRM-ESM2-1.

Because the aerosols burden influences the surface energy budget, the differences in AOD between CNRM-ESM2-1 and CNRM-CM6-1 explain most of the difference in surface temperature and climate over the present-day (Table 4). This effect reveals an example of the coupling between the land use and the aerosol scheme that should be carefully handled in an Earth system model. Yet, Table 4 suggests that the geographical distribution of bare soils in CNRM-ESM2-1 remains realistic with regard to the global averaged bias and rmse.

Figures 8d–8f show that regional differences over the cropland fractions are much more pronounced in CNRM-CM6-1 than in CNRM-ESM2-1 because CNRM-ESM2-1 considers the evolution of croplands as provided by LUHv2.0 h, whereas CNRM-CM6-1 does not. As a consequence, regional errors in cropland fraction are stronger in CNRM-CM6-1 than in CNRM-ESM2-1.

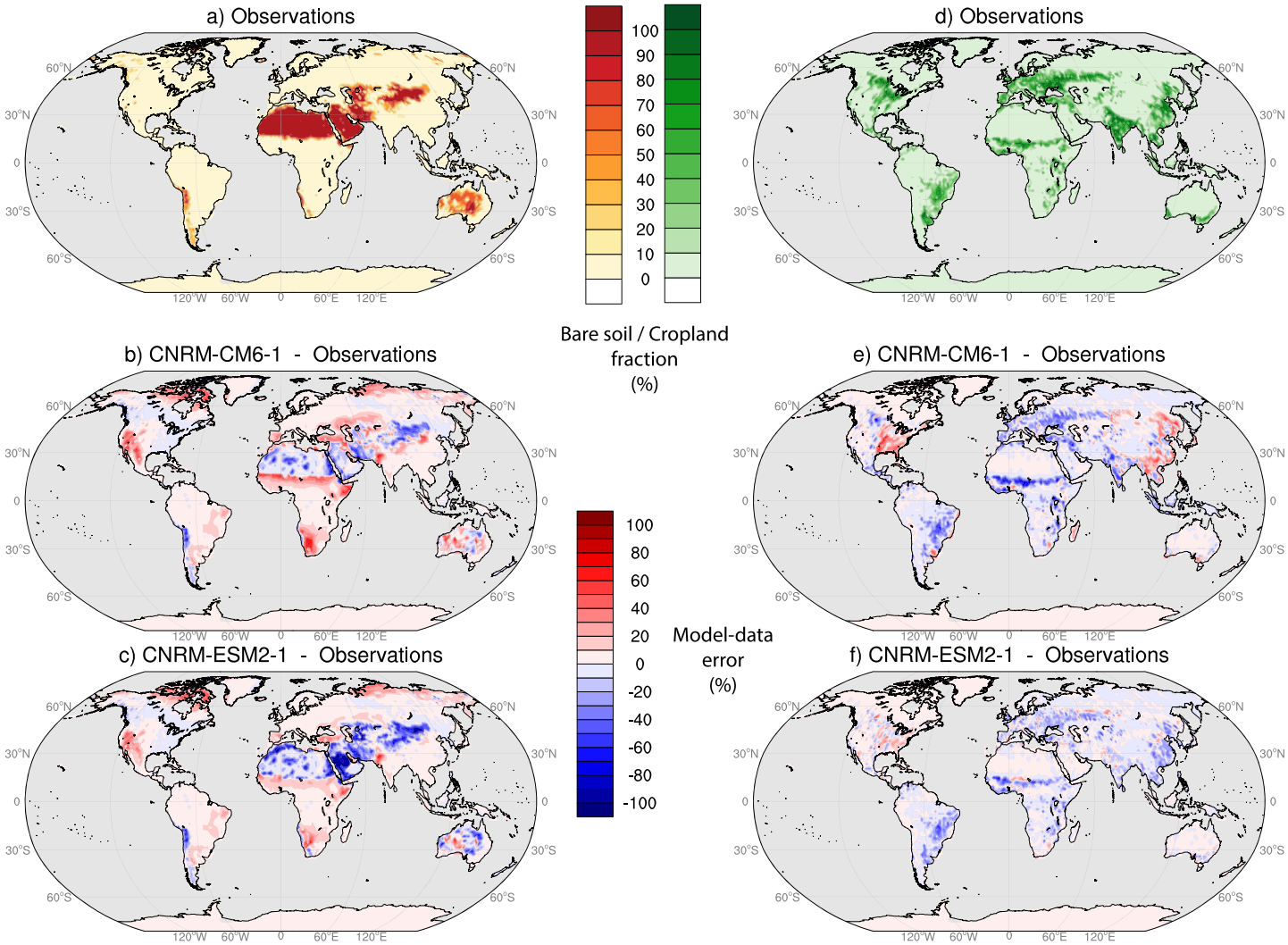

Figure 8. Fraction of bare soil (left) and crops (right) in 2000 as (a, d) observed from satellite (ESA-CCI Land cover data product, Poulter et al. (2015)) and the departure from observed values as simulated by (b, e) CNRM-CM6-1 and (c, f) CNRM-ESM2-1. Cropland areas included the fraction of C3 and C4 and rainfed and irrigated croplands for both satellite and models. In CNRM-ESM2-1, the cropland area is directly prescribed from the LUHv2.0 h data set.

4.2.6. Land and Ocean Biosphere

Land vegetation and ocean chlorophyll are both important geophysical fields that are recognized as tracers of biophysical coupling over land (e.g., Zeng et al., 2017) and oceans (e.g., Kahru et al., 1993; Sonntag & Hense, 2011). The comparison of these fields between the two models provides a valuable information to decipher differences in model climate response. To further this evaluation, we analyze simultaneously the seasonal extrema of LAI over land and of surface chlorophyll concentration over oceans (Figure 9).

Prescribed LAI and chlorophyll extremums as used in CNRM-CM6-1 better match observations than CNRM-ESM2-1 (Figure 9). The global mean bias and rmse in CNRM-CM6-1 (Table 4) are slightly lower than those associated with the interactive LAI and chlorophyll in CNRM-ESM2-1. This result is not surprising because CNRM-CM6-1 uses observational-derived LAI of the ECOCLIMAP data set and a modern reconstruction for surface chlorophyll based on a former run with NEMO-PISCES at 25 km forced by atmospheric reanalyses (Voldoire et al., 2019). However, these two fields do not respond to the bias in precipitation or mixed layer depth shown in Figure 4 and Figure 5, which tends to distort the physical consistency of the biophysical feedbacks as simulated in CNRM-CM6-1. This consistency is only captured in CNRM-ESM2-1 which displays errors in LAI and surface chlorophyll in agreement with physical drivers (Figures 9e and 9f).

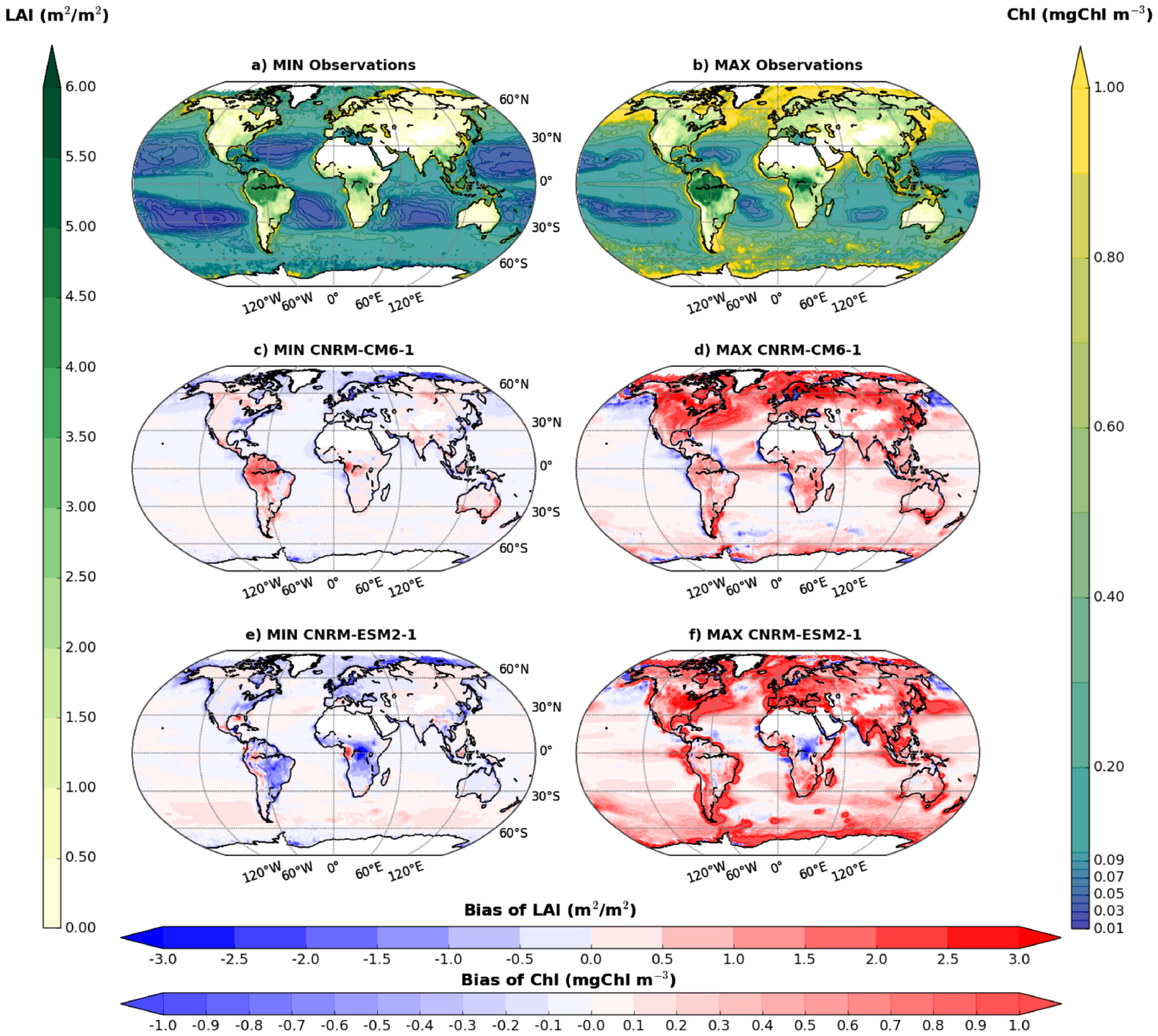

Figure 9. Composite of yearly minimum and maximum of leaf area index (LAI) over land surface and surface chlorophyll over ocean (Chl) over 1998–2011 for (a, b) observations (AVHRR LAI (Zhu et al., 2013) and ESA-CCI chlorophyll (Valente et al., 2016)) and the departure from observed values as simulated by (c, d) CNRM-CM6-1 and (e, f) CNRM-ESM2-1.

Figures 9d and 9f shows that both CNRM-CM6-1 and CNRM-ESM2-1 display large model-data errors for the annual maximum of chlorophyll and LAI. For LAI, this is a common feature also found in the previous generation of models (Anav, Friedlingstein, et al., 2013). It is explained by a too long growing season and a poor representation of mortality processes (Anav, Murray-Tortarolo, et al., 2013). For surface chlorophyll, this feature is not only explained by an erroneous representation of the phytoplankton growth in high-nutrient low-chlorophyll regions (e.g., Southern Ocean) and the nutrient-to-light limitation but also by the difficulty of remote-sensing data to observe deep chlorophyll maximum.

Figure 9f sheds light upon important differences in coastal chlorophyll maximum between CNRM-ESM2-1 and CNRM-CM6-1. This difference between the two models is attributed to the use of the interactive riverine inputs in CNRM-ESM2-1 and not in CNRM-CM6-1. Properly speaking, this CNRM-

ESM2-1's feature does not reveal a bias in simulated chlorophyll but rather the difficulties of the open-ocean retrieval algorithm (as used in European Space Agency Climate Change Initiative Ocean Color, ESA-CCI-OC, Valente et al. (2016)) to estimate coastal concentrations of surface chlorophyll. The optical properties of these oceanic coastal domains are influenced by terrestrial substances (such as minerals and humus) that do not vary with phytoplankton (Zheng & DiGiacomo, 2017). A specific evaluation of the impact of the land-ocean aquatic continuum coupling on coastal regions will be carried in a forthcoming work.

4.2.7. Global Carbon Cycle

We conclude this section with the comparison of simulated carbon fluxes. This evaluation aims at assessing natural carbon sinks (i.e., the net ecosystem productivity over land and the sea-to-air carbon fluxes over ocean) for both observations and models.

Here the so-called observations should be taken with caution because they consist in a combination of a feed-forward neural network data product (Landschützer et al., 2016) over ocean and in a multimodel best estimate of land model reconstructions over land (Huntzinger et al., 2013). Both data sets have been compared to the observations and show a good agreement in terms of mean state over the modern period, supporting their use for evaluating the natural carbon sinks as simulated by CNRM-ESM2-1 and CNRM-CM6-1.

The simulated land carbon sinks differ substantially between the two models (Figure 10), with the spatial correlation of model-data errors of CNRM-ESM2-1 and CNRM-CM6-1 being below 0.1 (Table 4). This is explained by different regional features. Figure 10b shows that CNRM-CM6-1 overestimates severely the carbon uptake by the tropical vegetation. This response is unrealistic given the model deficit in precipitation over these regions and is due to the use of a prescribed LAI (Figure 9) nonresponsive to climate variations. Figure 10c shows, on the contrary, that the regional errors in land carbon sink in CNRM-ESM2-1 clearly mirror the geographical error of physical drivers such as the precipitation in the tropics. Besides, CNRM-CM6-1 overestimates the land carbon sink, whereas CNRM-ESM2-1 does the opposite.

The ocean carbon fluxes can be only assessed for CNRM-ESM2-1 because CNRM-CM6-1 does not resolve the ocean carbon cycle. Figure 10c shows that CNRM-ESM2-1 captures the geographical distribution of observed sea-to-air carbon fluxes. CNRM-ESM2-1 displays regional errors smaller than 10 gC m^{-2} y^{-1} with respect to observational data product, except in the Southern Ocean where the negative bias in sea-air fluxes mirror the error in simulated mixed layer depth. The global mean error in simulated natural land and ocean carbon sinks of CNRM-ESM2-1 (-0.47 gC m^{-2} y^{-1}) is reasonable in regard to the global-average estimates of natural land and ocean carbon sinks (~20 gC m^{-2} y^{-1}).

4.3. Response to External Forcings

In this section, we compare the response to external forcing as simulated by CNRM-ESM2-1 and CNRM-CM6-1 using the CMIP6-DECK *abrupt-4xCO2* and *1pctCO2* simulations as well as the C4MIP *1pctCO2-bgc* and the AerChemMIP/RFMIP *piClim-control*, *piClim-anthro*, *piClim-ghg*, *piClim-4xCO2*, *piClim-lu*, and *piClim-aer* simulations (see Table S1 for further details on these model experiments). In addition, when possible, we compare both CNRM-ESM2-1 and CNRM-CM6-1 to the CMIP5 ensemble.

4.3.1. Equilibrium Climate Response to Rising CO_2

The influence of Earth system processes in the global climate response to an instantaneous quadrupling of atmospheric CO_2 (relative to preindustrial conditions) is assessed as follows.

First, we use the traditional linear forcing-feedback framework introduced by Gregory et al. (2004) to diagnose the forcing F, the feedback (λ), and the equilibrium climate sensitivity (ECS). In this approach, the Earth's TOA radiative imbalance (N) is $N = F + \lambda T_s$ where T_s is the global mean surface air temperature change, F is the stratosphere-troposphere adjusted radiative forcing, and λ (< 0) is the radiative feedback parameter. F, λ, and the equilibrium climate sensitivity (ECS = -F/λ) are deduced from a least squares fit of N onto T_s where the yearly sampled differences are computed between annual means of the instantaneous $4 \times CO_2$ experiment (abrupt-4xCO2) and the climatological mean from the piControl experiment.

Then, we use a radiative kernel approach following Vial et al. (2013) to decompose the climate sensitivity in terms of feedback and tropospheric adjustments associated with water vapor, temperature lapse rate, surface

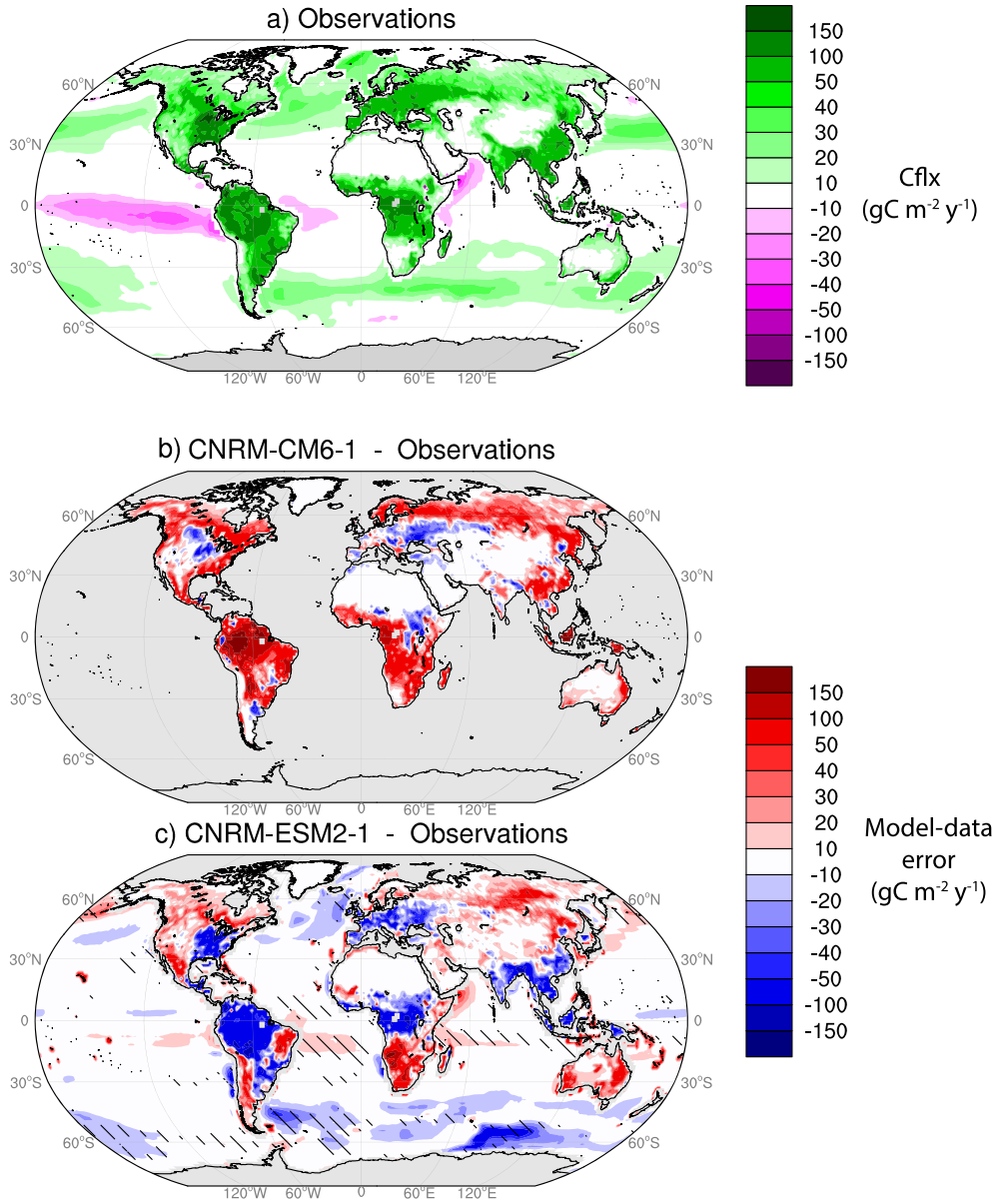

Figure 10. Land and ocean carbon sink (Cflx) in average over 1982–2010 for (a) observations (combination of the MsT-MIP model average over land (Huntzinger et al., 2013) and the neural network data product over ocean (Landschützer et al., 2016)) and the departure from observed values as simulated by (b) CNRM-CM6-1 and (c) CNRM-ESM2-1. Shading is indicative of the model-data absolute difference in magnitude of land and ocean carbon fluxes. Red regions indicate areas in models where the magnitude of the carbon flux is greater than that observed, whereas blue regions indicate the reverse. Light gray shading in the middle panel indicates missing data. Hatching in the bottom panel indicates disagreement in sign of the carbon fluxes between model and observations.

albedo, and clouds. This approach can also be used to estimate λ. The tropospheric adjustments to CO_2 forcing are computed using 30-year mean differences between the instantaneous 4 × CO2 experiment (*piClim-4xCO2*) and the preindustrial control run (*piClim-control*) with fixed preindustrial sea surface temperature. In these simulations, a small global mean surface temperature change occurs (around 0.5 °C), which is solely due to the land surface warming. The feedbacks are derived using the differences between *abrupt-4xCO2* and *piClim-4xCO2*, where the CO_2 concentration is now held fixed, but the surface temperature is allowed to change as the ocean warms. The reader can refer to Vial et al. (2013) for further details on the approach and the exact decomposition.

Table 6
Various Estimates of Adjusted Forcing, Climate Feedback Parameter, and Equilibrium Climate Sensitivity (ECS) as Simulated by CNRM-CM6-1 and CNRM-ESM2-1 Using the Linear Regression (Gregory et al., 2004; See Also Figure S2) or the Kernel (Vial et al., 2013) Approaches

	CNRM-CM6-1			CNRM-ESM2-1		
Method	Linear regression Gregory et al. (2004)		Kernels Vial et al. (2013)	Linear regression Gregory et al. (2004)		Kernels Vial et al. (2013)
Years	1–150 (full)	10–150	See text	1–150 (full)	10–150	See text
Adjusted Forcing (W m^{-2})	7.19	**6.94**	7.99	5.82	**6.45**	7.64
Net feedback parameter (W m^{-2} K^{-1})	−0.73	**−0.69**	−0.92	−0.61	**−0.71**	−0.96
ECS (K)	4.95	**5.06**	4.60	4.84	**4.55**	3.93

Note. Values highlighted in bold correspond to the best linear fit with $R^2 > 0.95$. These parameters are computed from the *abrupt-4xCO2* with respect to the climatological mean of the first 150 years of the preindustrial control simulation.

As shown in Table 6, the two methods lead to quite different estimates for the three parameters (i.e., adjusted forcing, radiative feedback parameter, and ECS) because of the different working hypothesis: for example, the ECS is estimated at $N = 0$ with the least squares fit, whereas it is calculated at $N \neq 0$ with the Kernels. Besides, our analysis suggests that the nonlinear climate response that occurs within the first 10 years of the *abrupt-4xCO2* experiment in CNRM-ESM2-1 (Figure S2) impacts the estimates of F, λ, and ECS calculated with least squares fit (Table 6). It is also worth noting that the adjusted forcing from the kernel approach is the same as the one diagnosed using the "fixed-SST" method (Hansen et al., 2005). In the CMIP5 ensemble, the fixed-SST radiative forcing is known to exceed the regression-based one by 0.3–1.1 W m^{-2} depending on models (Andrews, Gregory, et al., 2012).

Despite these uncertainties due to the choice of the method, the differences between the two model versions are consistent, especially when excluding the first 10 years in the regression method. Table 6 shows that CNRM-CM6-1 exhibits a stronger forcing and a weaker (less negative) feedback parameter, which both lead to a stronger ECS than in CNRM-ESM2-1, by ~10% (with the regression) to ~15% (with the kernels).

The analysis using the kernel decomposition suggests that the differences in climate sensitivity arise primarily from the feedbacks (Figure 11a). Consistently with the findings of Geoffroy et al. (2012), we show that the contribution from the tropospheric adjustments (F_{adj}) and the land surface warming to the GMT change is small overall (Figure 11a). The direct CO_2 forcing (F_{CO2}) induces about one third of the global warming, but it cannot explain the temperature change difference because F_{CO2} has been fixed to the value of Vial et al. (2013) for all models.

Although the differences between both models remain small in comparison to the range of ECS as estimated from the CMIP5 model ensemble (2.1–4.7 °C, Andrews, Gregory, et al., 2012), our analyses show that represented Earth system processes reduce the climate sensitivity by up to 0.5 °C—an order of magnitude comparable to the albedo or the clouds feedbacks estimated with the kernels. This global scale analysis shows that the long-term climate response to rising CO_2 may differ between an ESM and an AOGCM, contradicting the findings of Andrews, Ringer, et al. (2012) established with HadGEM2-ES and HadGEM2-AO.

Figure 11 goes further in the analysis by separating the various contributions to the adjusted forcing (Figure 11b) and feedback term (Figure 11c). All the adjustments estimated from CNRM-CM6-1 and CNRM-ESM2-1 compare well with the range of CMIP5 models as studied in Vial et al. (2013). When mapping the feedbacks on the same array of contributors (Figure 11c), our analysis suggests that both models exhibit fairly similar results, albeit with slightly stronger estimates in CNRM-CM6-1 than in CNRM-ESM2-1, which overall explain the difference in climate sensitivity between the two models. The geographical distributions of these feedbacks are shown in Figures S3, S4, and S5 and highlight stronger intermodel differences at the regional scale, especially over the oceans, in the North Atlantic, equatorial Pacific, and the Southern Ocean.

The differences with the previous generation of models is, however, clearer: the feedback contributions to the ECS in both CNRM-CM6-1 and CNRM-ESM2-1 are almost twice as large as in the CMIP5 ensemble

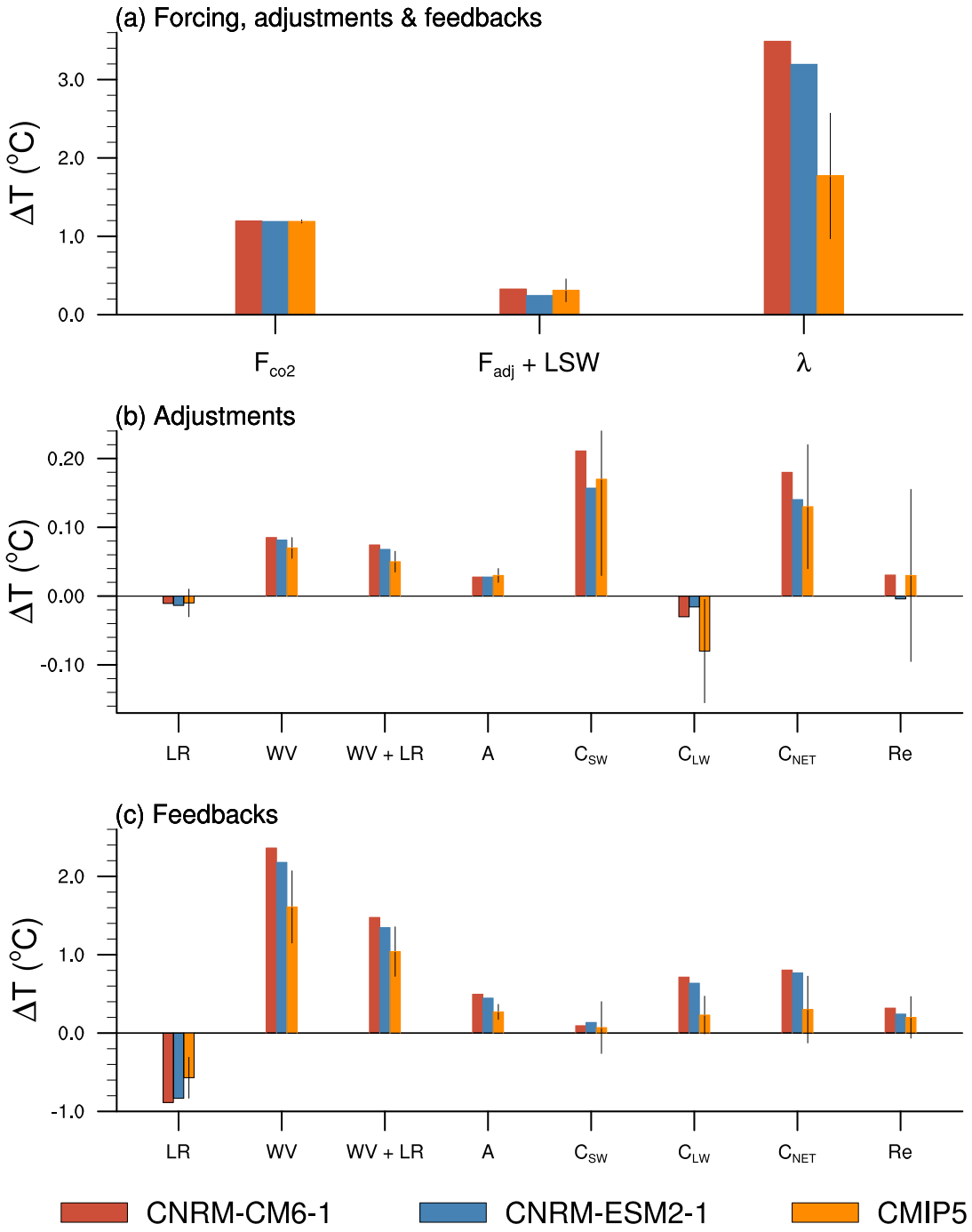

Figure 11. Contributions to equilibrium climate sensitivity for CNRM-CM6-1 (red), CNRM-ESM2-1 (blue), and the CMIP5 multimodel mean (yellow) following the decomposition of Vial et al. (2013) using the kernel approach. The different contributions are (a) the Planck response to the stratosphere-adjusted forcing (F_{co2}), the sum of Planck response to the tropospheric adjustments to CO_2 forcing (F_{adj}), and land surface warming (LSW) and the sum of feedbacks (l); (b) the tropospheric adjustments to CO_2 forcing and land surface warming associated with changes in the lapse rate (LR), the water vapor (WV), the sum of water vapor and lapse rate (WV + LR), the surface albedo (A), the clouds (SW, LW, and NET), and the residual (Re); (c) same decomposition as (b) but for the feedbacks. All values for CMIP5 models are from Vial et al., 2013 (derived from parameters in Tables 2 and 3). The error bars correspond to the intermodel standard deviation (1 sigma) for CMIP5 models.

mean, leading to a substantially higher climate sensitivity (Figure 11a and 11c). This difference arises primarily from the longwave cloud feedback and secondly from the combined water vapor and lapse rate feedback (Figure 11c). The pronounced increase in the altitude of the tropical high clouds, in CNRM-

Table 7
Transient Climate Response (TCR), Realized Warming Fraction (RWF), and Transient Climate Response to Cumulative Emissions (TCRE) as Estimated for CNRM-CM6-1 and CNRM-ESM2-1 From the 1pctCO2 Simulation With Respect to the Climatological Mean of the First 150 Years of the piControl Simulation

	CNRM-CM6-1	CNRM-ESM2-1
TCR (K)	2.0	1.92
RWF (-)	0.40	0.43
TCRE (K EgC^{-1})	NA	1.73

Note. The TCR is estimated using the 21-year averaged with the central year at CO2 doubling with respect to the long-term average of the piControl simulation. The realized warming fraction (RWF) corresponds to the TCR-to-ECS ratio for both models computed from 10 to 150 years excluding the strong nonlinear behavior due to stratospheric ozone (as shown in Table 6). Finally, the transient climate response to cumulative emissions (TCRE) has been estimated from the 1pctCO2 simulation as in Gillett et al. (2013).

CM6-1 and CNRM-ESM2-1, could potentially explain the stronger longwave cloud feedback with respect to the CMIP5 ensemble, as this process dominates the (positive) longwave cloud feedback in general (Zelinka & Hartmann, 2010). As for the combined water vapor and lapse feedback, it could depend to some extent on changes in the upper-tropospheric relative humidity (Vial et al., 2013).

4.3.2. Transient Climate Response to Rising CO_2

Table 7 shows that the difference in transient climate response (TCR) is small between the two models (~4%). These two estimates of TCR lie within the upper 5–95% range as assessed in Gillett et al. (2013) with CMIP5 models, that is, 0.9–2.3 °C. The realized warming fraction (RWF), that is, the TCR-to-ECS ratio, is higher in CNRM-ESM2-1 than in CNRM-CM6-1, suggesting that more warming has being expressed in the former. This behavior agrees with the findings of Pfister and Stocker (2018) based on the previous generation of Earth system models, suggesting that high-ECS models display relatively low RWF and hence a stronger warming commitment.

We can estimate the transient climate response to cumulative emissions (TCRE) only for CNRM-ESM2-1 because it simulates the evolution of the global carbon sinks in response to rising CO_2 and climate change (see Figure 12 and associated text below). When diagnosing the cumulative CO_2 emissions as in Jones et al. (2013) from the 1pctCO2 simulation, we find a TCRE of about 1.73 K EgC^{-1} at CO_2 doubling (Table 7), which lies well within the range of estimates as produced by the previous generation of CMIP5 Earth system models, that is, 0.8–2.4 K EgC^{-1} (Gillett et al., 2013). Nonetheless, CNRM-ESM2-1 exhibits a TCRE that is ~28% higher than the observationally constrained best estimate (1.35 K EgC^{-1}) as published in Gillett et al. (2013).

Figure 12 provides another view of the climate response to rising CO_2 by breaking down the response of the vegetation carbon cycle and hydrological cycle.

Figures 12 shows first that the climate response to rising CO_2—that is, α in the climate-carbon feedbacks framework of Friedlingstein et al. (2006)—is greater in CNRM-CM6-1 (6.20 10^{-3} °C ppm^{-1}) than in CNRM-ESM2-1 (5.89 10^{-3} °C ppm^{-1}), given that both models display a stronger sensitivity to rising CO_2 than CMIP5 models. This implies a difference of about 5% between the response of CNRM-CM6-1 and CNRM-ESM2-1 which is consistent with the TCR estimates (Table 7).

We explain this difference by three factors:

1. The vegetation antitranspiration effect of rising CO_2 under a constant climate
2. The response of vegetation biomass and ecophysiology to rising temperature and climate change
3. The other Earth system feedbacks such as the change in stratospheric ozone and aerosols radiative forcing in response to climate change

The first two factors contribute to the CO_2-water-stomatal feedback which depicts a reduction in vegetation transpiration due to rising CO_2, amplifying the warming (Figure S6). Figure 12 shows indeed that this feedback inferred from the transpiration-CO_2 relationship is about 10% stronger in CNRM-CM6-1 than in CNRM-ESM2-1. This difference between both models is explained by the fact that CNRM-CM6-1 displays at the same time a stronger response in the carbon assimilation to rising CO_2 (Assimilation-CO_2 in

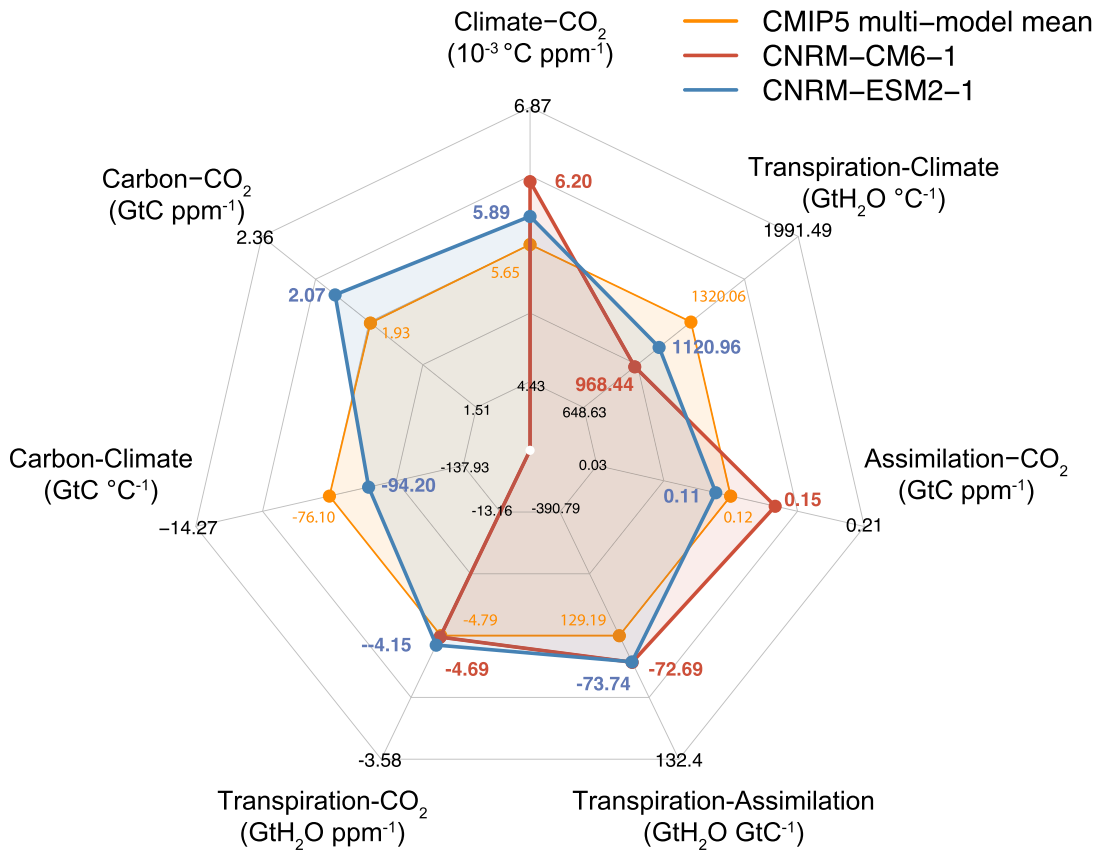

Figure 12. Spider diagram representing the response of the carbon cycle to rising CO_2 and global warming as estimated from CNRM-CM6-1 (red), CNRM-ESM2-1 (blue), and CMIP5 (orange). Climate-CO_2 (α), carbon-CO_2 (β), and carbon-climate (γ) represent the carbon cycle-climate feedback parameters as deduced from Arora et al. (2013) using piControl and 1pctCO2 from CMIP6-DECK (Eyring et al., 2016) and 1pctCO2-bgc as requested by C4MIP (Jones et al., 2016). These feedback parameters are not available for CNRM-CM6-1 because this model does not resolve global carbon cycle. Transpiration-Climate, Transpiration-CO_2, Transpiration-Assimilation of Carbon, and Assimilation of Carbon-CO_2 represent feedback parameters to diagnosed difference in CO_2-stomata-water feedbacks. The decomposition of those feedbacks is provided in Figure S6. Parameter estimates for CMIP5 are deduced from the same ensemble of models that were assessed in IPCC AR5 (Ciais et al., 2013).

Figure 12) and a weaker response of transpiration to rising temperature than those of CNRM-ESM2-1 (Transpiration-Climate in Figure 12). We attribute these differences to the response of vegetation to rising CO_2 and climate change which both impact vegetation biomass and ecophysiology in CNRM-ESM2-1 but not in CNRM-CM6-1 (carbon-climate in Figure 12).

We isolate the influence of the antitranspiration effect of rising CO_2 on α by computing the difference between C4MIP *1pctCO2-bgc* simulations as produced by CNRM-ESM2-1 and CNRM-CM6-1. We find a difference of sensitivity of 0.18 10^{-3} °C ppm^{-1} in average over the last 10 years of the simulation, implying that vegetation may drive about 60% of the difference in α between CNRM-CM6-1 and CNRM-ESM2-1.

The remaining 40% of difference in α are thus attributed to other represented Earth system processes and feedbacks such as change in stratospheric ozone and aerosol radiative forcing in response to climate change. We find that changes in sea-salt aerosol emissions due to increasing surface winds and rising ocean temperature control the largest part of this signal (not shown).

We also assess the magnitude of the carbon cycle feedbacks in CNRM-ESM2-1 using the C4MIP simulations in the framework of Friedlingstein et al. (2006). Figure 12 shows that CNRM-ESM2-1 predicts a carbon-concentration feedback, β, which is stronger than the CMIP5 multimodel mean. This is not surprising because the CMIP5 multimodel mean includes the outcomes of CESM1-BGC and NorESM2-ME which simulated a strong weakening of the CO_2 fertilization with a strong nitrogen limitation.

Our analyses show that the relatively strong $\beta$for CNRM-ESM2-1 is driven by land carbon cycle (~1.365 PgC ppm^{-1}); the ocean β of CNRM-ESM2-1 (0.705 PgC ppm^{-1}) is slightly lower than the IPCC AR5 best estimate (0.92 $\pm$ 0.44 PgC ppm^{-1}, Ciais et al., 2013). This behavior suggests that the implicit nitrogen limitation parameterization as used in ISBA weakly constrains the assimilation of CO_2 by land vegetation. With that being said, the order of magnitude of the land β of CNRM-ESM2-1 remains consistent with the range of response constrained by observations in the Northern high latitudes (Wenzel et al., 2016).

Consistently with its response to rising CO_2, the response of the carbon cycle simulated by CNRM-ESM2-1 predicts a climate-carbon cycle feedback, γ, stronger than the CMIP5 multimodel mean. Here again, this feature is controlled by the response of the land carbon cycle: land γ of CNRM-ESM2-1 is stronger (−85.24 PgC °C^{-1}) than the IPCC AR5 best estimate (−58.4 $\pm$ 28.5 PgC °C^{-1}). In contrast, ocean γ of CNRM-ESM2-1 (−8.96 PgC °C^{-1}) is consistent with the IPCC AR5 assessed *likely* range (−7.8 $\pm$ 2.9 PgC °C^{-1}, Ciais et al., 2013). This behavior is not surprising because there is a tight relationship between β and γ over land (Huntzinger et al., 2017): the magnitude of γ increases with rising β.

The climate gain ($g = -\alpha\gamma/(1+\beta)$) resulting from the carbon cycle feedbacks can be estimated using the framework Friedlingstein et al. (2006). In CNRM-ESM2-1, g=0.16, meaning that carbon cycle feedbacks would amplify the warming by about 0.2 °C per °C of temperature change.

Because of the abovementioned climate feedbacks, the geographical distribution of warming induced by a CO_2 increase differs between models (Figure 13). CNRM-ESM2-1 is warmer than CNRM-CM6-1 over the Arctic and in the tropics. CNRM-CM6-1, in contrast, warms more over the middle- and high-latitude Southern Hemisphere. The largest difference is found off Antarctica, where the warming of CNRM-CM6-1 is twice as large as the global average, unlike in CNRM-ESM2-1. Finally, both models display a noticeable difference over the North Atlantic "warming hole" where little to no warming occurs. It is more intense and farther south in CNRM-ESM2-1 than in CNRM-CM6-1. Because of these differences, we can anticipate differences in future projections and climate impacts.

4.3.3. Other Climate Forcings

In this section, we assess the potential contribution of each climate forcing to climate change in terms of radiative forcing in both CNRM-CM6-1 and CNRM-ESM2-1. For that purpose, we use the concept of effective radiative forcing (ERF) defined as the change in net downward radiative flux at the TOA after the adjustments of atmospheric temperatures, water vapor, clouds, and land albedo, but with unchanged global mean surface temperature and ocean and sea ice conditions. Thus, ERF has been calculated using RFMIP and AerChemMIP simulations where all climate forcers are set to preindustrial values (1850), except the one which is tested. The *piClim-control* simulation with all forcers set to 1850 is used as the reference. Results are presented in Figure 14, where values of CNRM-CM6-1 and CNRM-ESM2-1 are noted in W m^2 for year 2014. The estimation from IPCC AR5 (Myhre et al., 2013a) are given for year 2005 as a qualitative range for comparing CNRM-ESM2-1 and CNRM-CM6-1 results. Indeed, we estimate that the difference in greenhouse gase concentrations between 2005 and 2014 could lead to an increase of about 0.30 W m^2. The impact is less important for aerosols and land use since both forcings have not varied significantly between 2005 and 2014.

First of all, all the ERF calculated in both models for the different climate forcers are in the *likely* range of IPCC AR5. However, the comparison between both models is an essential asset to understand the role of each climate forcer, since both models share all the other characteristics (atmospheric and ocean physics, surface model, etc.).

In that sense, it should be highlighted that the breakdown of the anthropogenic forcing between land use, aerosols, and greenhouse gases is different in both models although the total anthropogenic forcing is close (1.59 W m^{-2} in CNRM-ESM2-1 and 1.50 W m^{-2} in CNRM-CM6-1). Indeed, as explained in the previous section, the greenhouse gases exert a lower forcing in the ESM model (2.41 W m^{-2} in CNRM-ESM2-1 and 2.64 W m^{-2} in CNRM-CM6-1, Figure 14). Besides, aerosols, whose forcing is negative, have also a lower ERF in absolute values in CNRM-ESM 2-1, both in their interactions with radiation (−0.21 vs −0.42 W m^{-2}) and clouds (−0.61 vs −0.79 W m^{-2}). This difference in aerosol ERF could probably come from the use of the interactive scheme in CNRM-ESM2-1 compared to CNRM-CM6-1 using monthly averaged AOD fields, thus underlying the potential role of aerosol variability. Indeed, the use of monthly AOD fields in CNRM-CM6-1

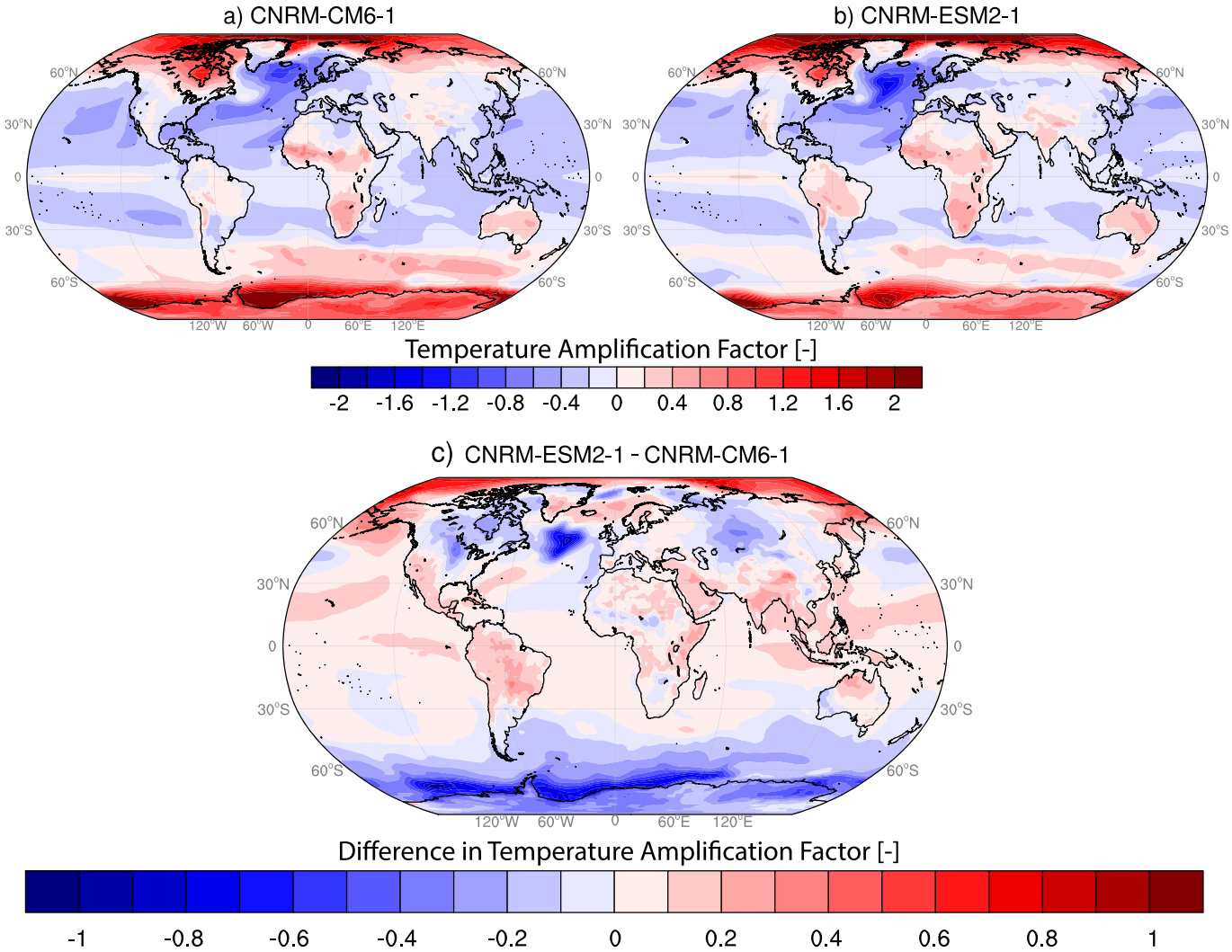

Figure 13. Geographical pattern of warming at 4xCO2 as simulated by (a) CNRM-CM6-1 and (b) CNRM-ESM2-1. (c) displays the difference in warming pattern between CNRM-ESM2-1 and CNRM-CM6-1. The geographical pattern of warming is estimated using the temperature amplification factor = T/GMT - 1 over the last 50 years of the abrupt-4xCO2 relative to the preindustrial control.

limits the range of values that aerosol loads can have, both for lower and higher values. This is also important for the first indirect aerosol effect which is represented in the model, following the work of Menon et al. (2002), in which the cloud droplet number concentration depends on the aerosol mass of sulfate, sea-salt, and organic matter. Finally, it is worth noting that CNRM-ESM2-1 also includes land use and land cover changes, which exert a small negative forcing (-0.07 W m^{-2}). This climate forcer is not represented in CNRM-CM6-1.

4.4. Historical Climate Reconstruction and Future Climate Projections

In this last section, we analyze CMIP6 *historical* simulations and the future projections of ScenarioMIP as performed by CNRM-ESM2-1 and CNRM-CM6-1. The reader can refer to Table S1 for further details about the future scenarios studied in this section.

4.4.1. Reconstruction of the Historical Climate

Figure 15 provides an overview of the industrial-era climate (1850–2014) as simulated by CNRM-ESM2-1 and CNRM-CM6-1 with respect to the most up-to-date observations (CMIP6 *historical*).

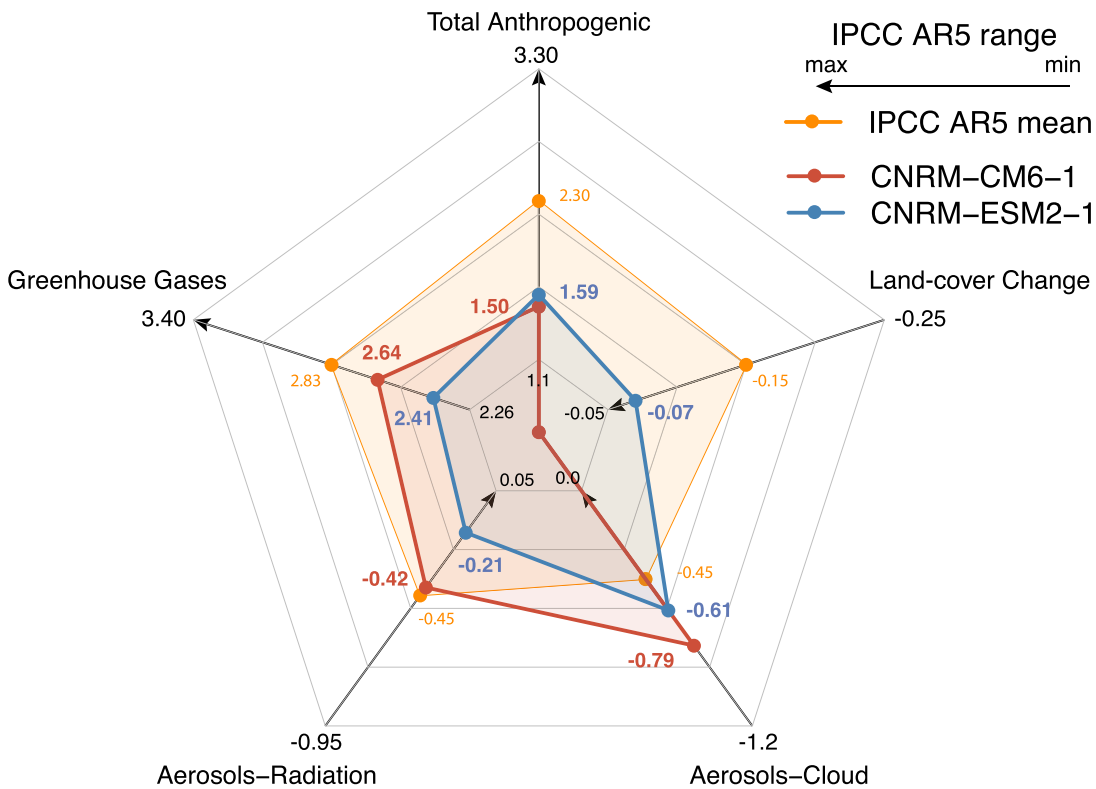

Figure 14. Spider diagram representing the effective radiative forcing of the climate system as estimated from CNRM-CM6-1 (red) and CNRM-ESM2-1 (blue) in 2014. The effective radiative forcing as assessed in IPCC AR5 (orange) is provided for year 2005. It is displayed as an indicative range for comparing the results of CNRM-CM6-1 and CNRM-ESM2-1. The arrows are indicative of the range of estimates as assessed by IPCC AR5 (Myhre et al., 2013a). The central point of the spider diagram is representative of a missing external forcing.

Figure 15a presents the evolution of the global warming with respect to the 1850–1900 average. The simulated global warming is computed by applying the observational mask of the HadCRUT4 data set on model surface air temperature fields.

Figure 15a shows that both models capture the industrial-era warming. Both models compare well in terms of skill to the previous generation of Earth system models as evaluated in Anav, Friedlingstein, et al. (2013). Over the modern period (2005–2014), the observed warming is 0.81 ± 0.05 °C (1 sigma, i.e., the standard deviation estimated from the year-to-year variations over 2005–2014) as compared to the reference 1850–1900 average. CNRM-CM6-1 ensemble mean compares well to the observed warming (0.86 ± 0.08 °C), whereas CNRM-ESM2-1 underestimates it (0.70 ± 0.06 °C). Figure 15a also shows that the timing in historical warming is better represented in CNRM-CM6-1 than in CNRM-ESM2-1. In particular, CNRM-ESM2-1 fails at simulating the early warming onset in the 1940s. Given that both models exhibit a particularly strong internal variability at the centennial timescale, part of this difference could be explained by the limited sampling of the internal variability (five ensemble members are used for CNRM-ESM 2-1, whereas ten are used for CNRM-CM6-1).

A similar agreement is found between observed and simulated 0–700 m ocean heat content with respect to 1955–2006 average (Figure 15b). Both CNRM-ESM2-1 and CNRM-CM6-1 capture the fluctuations in ocean heat content due to major volcanic eruptions of the twentieth century (i.e., Agung in 1963, El Chichon in 1982, Pinatubo in 1991). The observed storage of heat in the first 700 m of the ocean reaches 10.65 ± 1.41 ZJ on average over 2005–2014. Figure 15b shows that CNRM-CM6-1 and CNRM-ESM2-1 are in good agreement with observations despite a slight overestimation of about 1 ZJ in the ocean heat content relative to 1955–2006. It is interesting to note that the accumulation of heat within the 700 m of the ocean between 2005 and 2014 relative to the 1855–1876 level as simulated by CNRM-ESM2-1 is in good agreement with the long-term estimates of Gleckler et al. (2016), whereas it is

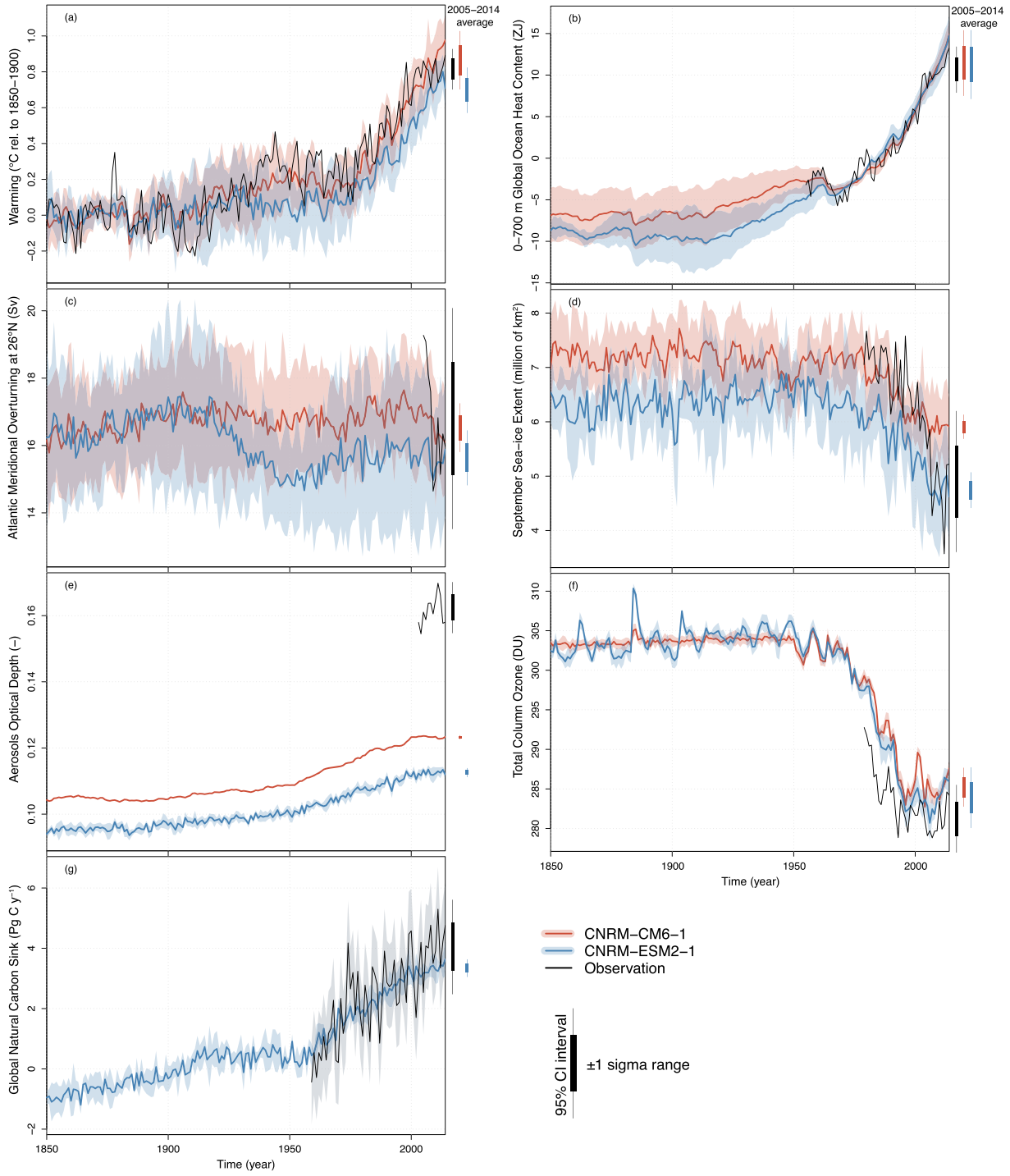

Figure 15. Time series of various climate indices as monitored from available observations (black solid line) and as simulated by CNRM-CM6-1 (red solid line) and CNRM-ESM2-1 (blue solid line) since 1850 with global warming (a), 0–700 m ocean heat content (b), Atlantic meridional overturning circulation (c), September arctic sea ice extent (d), global average aerosols optical depth at 550 nm (e), total ozone column (f), and global land and ocean carbon flux (g). Global metrics for observations are estimated from the HadCRUT4 database (Morice et al., 2012) for the global warming, the WOA-based ocean heat content (Levitus et al., 2012), the RAPID-MOCHA transport measurements at 26°N (Smeed et al., 2018), the NSIDC September sea ice extent (Fetterer et al., 2002), the MODIS AQUA aerosol optical depth at 550 nm (Levy, Mattoo, et al., 2013), the NIWA-BSv3.3 total ozone column patched data sets (Bodeker et al., 2005), and the combined land and ocean carbon sink from the Global Carbon project (Le Quéré et al., 2018). For carbon fluxes, positive (negative) fluxes indicate an uptake (outgassing) of CO_2 by land or ocean. For CNRM-ESM2-1 (CNRM-CM6-1), the shading (hatching) indicates the 1 sigma range around the 5 (10) members ensemble mean. The simulated global warming is computed by applying the observational mask of the HadCRUT4 data set on model surface air temperature fields. Whisker-plots on the right-hand side are estimated from the model ensemble mean over 2005–2014 period.

overestimated by CNRM-CM6-1. This difference might amplify the future warming in CNRM-CM6-1 compared to CNRM-ESM2-1.

Figures 15c and 15d provide a different view of the ocean response over the industrial era by analyzing the response of the Atlantic Meridional Overturning Circulation (AMOC) at 26°N and the September sea ice extent to climate change. Both geophysical variables are responsive to climate change but are less directly tightened to changes in Earth's energy balance (because of external forcing) than global mean surface temperature or ocean heat content. Figure 15c displays the AMOC at 26°N as observed from 2004 by the RAPID section (McCarthy et al., 2015) and modeled in the historical period by CNRM-CM6-1 and CNRM-ESM2-1 models. With an average magnitude over 2005–2014 of 16.5 $\pm$ 0.4 Sv for CNRM-CM6-1 and 15.6 $\pm$ 0.4 Sv for CNRM-ESM 2-1, the modeled AMOC is in good agreement with the average observed value of 17.2 Sv. Both models show a large ensemble spread, consistently with the large low-frequency AMOC variability documented by Voldoire et al. (2019) for CNRM-CM6-1. Such a variability is a limitation to document forced changes of AMOC transport and other related climate indices (e.g., the Atlantic Multidecadal Variability). In particular, neither model shows any significant AMOC trend, although recent observations suggest that the North Atlantic Ocean is in a state of reduced overturning (Smeed et al., 2018). Note that the apparent ensemble mean low-frequency AMOC variability of CNRM-ESM2-1 model is likely due to a too small ensemble size, suggesting that ten members are necessary to document such internal climate variability.

Figure 15d shows that the modeled September sea ice extents differ in terms of mean state and trends. CNRM-CM6-1 displays the largest cover of September sea ice over the 1850–2014 period. Over the recent decades, CNRM-CM6-1 displays a low sensitivity to climate change. Voldoire et al. (2019) attribute this behavior to an overestimated snow cover preventing the sea ice from melting. This leads CNRM-CM6-1 to overestimate the September sea ice coverage on average over 2005–2014 by about 1.5 $\pm$ 0.2 10^6 km^2 with respect to the observations. The recent trend in September sea ice extent is better captured by CNRM-ESM2-1 than CNRM-CM6-1 in spite of an underestimation of the September sea ice extent before 2005. The difference in recent trends is partly explained by the use of ocean biophysical feedbacks (see section 2.1). The occurrence of phytoplankton blooms in summer close to the sea ice border in CNRM-ESM2-1 tends to amplify the magnitude of the ocean warming. Such phenomenon reinforces the melting of sea ice in autumn (Lengaigne et al., 2009). This response is stronger in CNRM-ESM2-1 than in CNRM-CM6-1 because of the use of an interactive marine biogeochemistry which responds to the retreat of sea ice over the recent decades. Nevertheless, our analysis suggests that neither CNRM-ESM2-1 nor CNRM-CM6-1 are able to replicate at the same time the long-term mean and linear trend over 1979–2010 as used as observational constraints of September Arctic sea ice extent in Massonnet et al. (2012).

Figures 15e, 15f, and 15g give an overview on the transient evolution of Earth system components.

Consistently with Figure 7, Figure 15e shows that the global average AOD at 550 nm differ substantial between models and observations. This Figure shows that CNRM-CM6-1 and CNRM-ESM2-1 display a comparable increase in AOD from 1850 to 2014. However, it is difficult to discuss how far the simulated trends in AOD compare to observations given the length of the observational records (2003–2014).

Figure 15f presents the evolution of the global average total ozone column from 1850 to 2014. This geophysical field is involved in the radiative balance of the climate system as simulated in CNRM-ESM2-1 and CNRM-CM6-1. Figure 15f shows that the simulated total ozone column of both models compares reasonably well with observations given the range of model uncertainty assessed in Eyring et al. (2013). Over the 2005–2014 period, CNRM-ESM2-1 displays a slightly better agreement with the observed total ozone column (283.89 $\pm$ 1.95 DU with respect to 281.23 $\pm$ 2.17 DU) than CNRM-CM6-1 (285.22 $\pm$ 1.25 DU). Figure 15f shows that both models capture the ozone depletion trends from 1970 to 2000 consistently with the NIWA-BSv3.3 data. They also replicate the stoppage of the ozone depletion trends from 2000 onward that results from the Montréal Protocol in 1987 and the ban of anthropogenic chlorofluorocarbon emissions in 1989.

Figure 15g presents the transient response of the global carbon sink to rising CO_2, changing climate, and land cover change. Compared to aerosols and atmospheric chemistry, the carbon cycle as simulated by

CNRM-ESM2-1 run in a concentration-driven mode does not impact the radiative balance of the Earth system, except by the biophysical feedbacks (discussed above). So, the present evaluation aims at looking at the global carbon sink as a diagnostic to track change in allowable CO_2 emissions (Jones et al., 2013) or to anticipate potential model biases in forthcoming emission model simulations (Friedlingstein et al., 2014). We focus here only on the global carbon sink as simulated by CNRM-ESM2-1 because CNRM-CM6-1 does not simulate the ocean carbon sink nor land cover change and associated CO_2 emissions. Figure 15g shows that CNRM-ESM2-1 captures the long-term reinforcement of the global carbon sink as shown by the Global Carbon Project (GCP) reconstruction between 1959 and 2014 (Le Quéré et al., 2018). Although this reconstruction is not a pure observational data product, it represents the best estimates of the global carbon sink over the industrial since 1959. It has been elaborated with various lines of evidence including pure observations, atmospheric inversion, data-driven models, and model reconstructions forced by atmospheric reanalyses (Le Quéré et al., 2018).

Over the modern period (2005–2014), CNRM-ESM2-1 simulates reasonably well the magnitude of the global carbon sink with a sink of carbon of about 3.34 ± 0.14 Pg C y^{-1} that is slightly weaker than the GCP reconstruction (4.03 ± 0.15 Pg C y^{-1}). The model also captures the long-term reinforcement of the land and ocean carbon sinks associated with rising atmospheric CO_2 (Ciais et al., 2019; DeVries et al., 2019). However, it is important to stress that CNRM-ESM2-1 strongly underestimates the magnitude of the interannual variability compared to the GCP reconstruction, that is, 0.19 Pg C y^{-1} versus 0.84 Pg C y^{-1}. This model deficiency may be explained by erroneous pattern of precipitation in the tropics that damps the year-to-year variability of the land carbon sink in this region. This suggests that the global carbon cycle simulated by CNRM-ESM2-1 still suffers from deficiencies as already highlighted by Ciais et al. (2013) in the previous generation of Earth system models.

4.4.2. Future Climate Projections

Given the evaluation of the industrial era's tendency of key climate fields, we now focus on future projections as conducted in ScenarioMIP (O'Neill et al., 2016). It is important to stress that CNRM-ESM2-1 contributes to the entire scenario matrix, whereas CNRM-CM6-1 has performed the tier-1 projections only. Figure 16 shows the future projections from 2015 to 2100 of both models in terms of global mean surface temperature, ocean heat content, and global carbon sink are compared to the well-established climate emulator MAGICC6 (Meinshausen et al., 2011). MAGICC6 is able to emulate the full range of CMIP5 results by exploring range of ECS as assessed by AR5, that is, a likely range (66%) of 1.5–4.5 °C and a very likely range (90%) of 1–6 °C). The idea here is to compare the future projections as simulated by CNRM-ESM2-1 or CNRM-CM6-1 to the median outcomes of MAGICC6 emulating the median climate response of CMIP5 models for these CMIP6 scenarios.

Figure 16a highlights different features in terms of future warming between CNRM-ESM 2-1, CNRM-CM6-1, and MAGICC6. It shows in particular that, for a given scenario, CNRM-CM6-1 warms more than CNRM-ESM2-1. The difference is about 0.7 °C on average over 2081–2100 for *ssp585*, but it is smaller (i.e., between 0.15 and 0.25 °C) for the other scenarios.

Our analyses confirm that the difference in future warming between CNRM-ESM2-1 and CNRM-CM6-1 are rather driven by their response to CO_2 than by their response to aerosols. Indeed, the differences in AOD (Figure S8a) have only a small effect on the predicted warming (Figures S7 and S8). Using the absolute global temperature potential for non-CO_2 (Myhre et al., 2013b, SM 11.2), we estimate that the contribution of the direct aerosol forcing (aerosol-radiation interaction only, Figure S8) leads to a difference in predicted warming of about ~0.01 °C in average over 2081–2100. This implies that the direct contribution of aerosols to global warming explains up to 7.5% of the intermodel difference in global warming. These estimates represent nonetheless the lower range of the temperature changes due to aerosols because our calculations only consider the direct effect of aerosols. The inclusion of the aerosols indirect effect, that is, the interaction with clouds, might strengthen the relative contribution of aerosols to global warming, without however encompassing for the difference in future warming between both models.

Figure 16a shows that the median warming simulated by MAGICC6 stays always below the warming projected by CNRM-ESM2-1 (and hence CNRM-CM6-1), except for *ssp585* where there is a rather good agreement in average over 2081–2100: 5.02 ± 0.45 °C for CNRM-ESM2-1 and 5.14 ± 0.45 °C for MAGICC6. We attribute this difference to the radiative forcing of non-CO_2 greenhouse gases and aerosols that is stronger

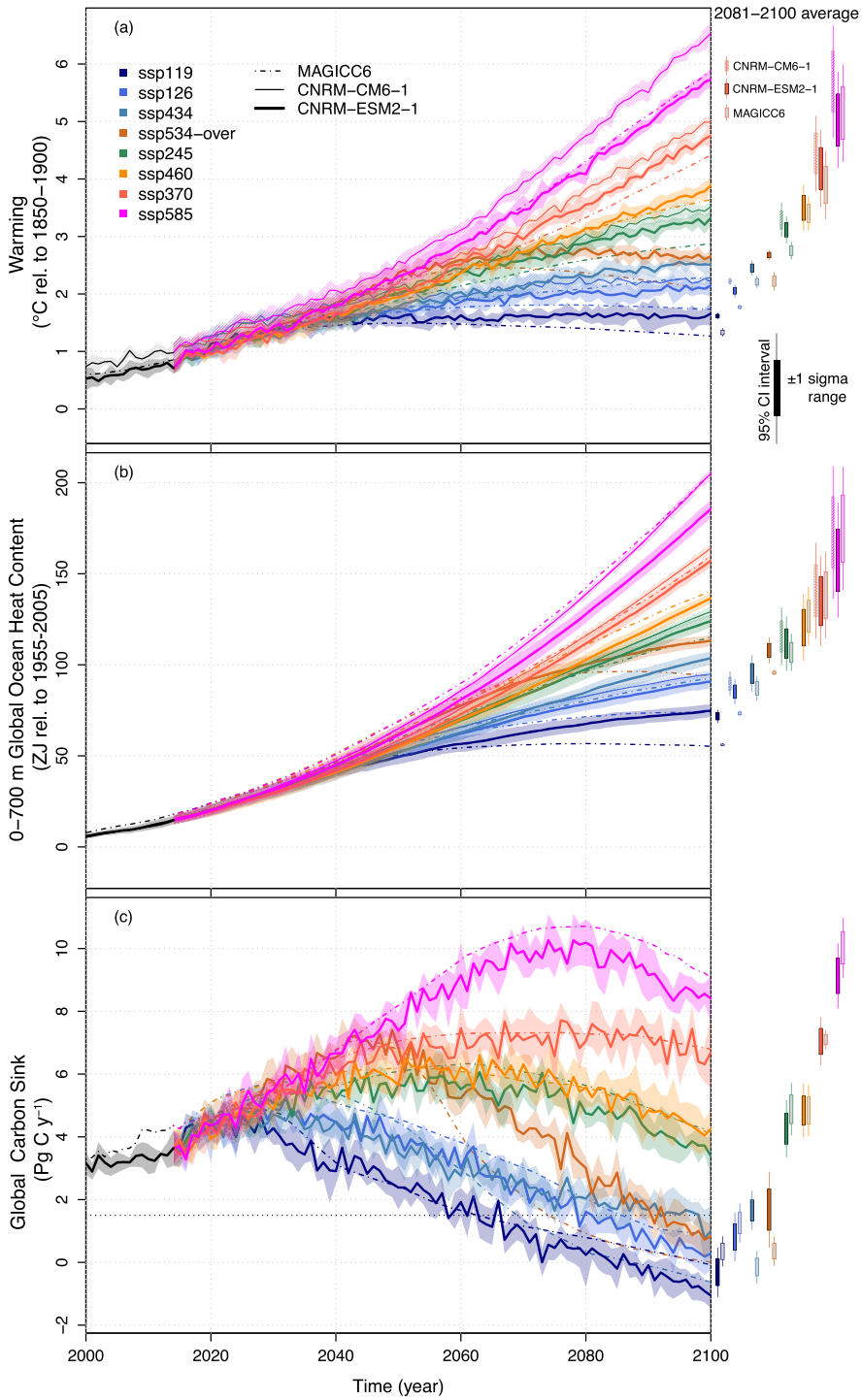

Figure 16. Future climate projections from 2014 to 2100 as simulated by CNRM-CM6-1 (thin solid lines), CNRM-ESM2-1 (thick solid lines), and the median of 600 simulations performed by MAGICC6 in probabilistic mode (dashed lines). (a) shows the global warming, (b) shows the 0–700 m ocean heat content, and (c) shows the global combined land and ocean carbon flux. For carbon fluxes, positive (negative) fluxes indicate an uptake (outgassing) of CO_2 by land or ocean. For CNRM-ESM2-1 (CNRM-CM6-1), the shading (hatching) indicates the 1 sigma range around the 5 (6) members ensemble mean. Wisker-plots on the right-hand side are estimated from the model ensemble mean over 2081–2100 period for each scenario. Hatched whisker boxes are used for CNRM-CM6-1; filled whisker boxes are used for CNRM-ESM2-1; gray-filled whisker boxes are used for the median outcome from MAGICC6. The acronym "sspXYY" indicates the shared socioeconomic pathways (ssp) based on a development pathway X (i.e., 1, 2, 3, 4, or 5) reaching a net radiative Y. Y by 2100. Here, the ssps are ordered by increasing radiative forcing, with ssp119 reaching 1.9 W m^{-2} by 2100 at the left and ssp585 reaching 8.5 W m^{-2} by 2100 at the right. ssps can be also classified by development pathway where ssp1, ssp3, ssp4, and ssp5 assume respectively "sustainability," "regional rivalry," "inequality," and "fossil-fuel intensive development." ssp 2 is assumed as a "middle of the road" pathway.

in CNRM-ESM2-1 than in MAGICC6 leading to more warming. This statement is supported by the fact that the difference between CNRM-ESM2-1 and MAGICC6 is smaller in *ssp585* due to the predominance of CO_2 forcing with respect to the other climate forcers.

Interestingly, the largest differences are found for the overshoot scenarios (*ssp119*, *ssp126*, and *ssp534-over*) where MAGICC6 displays a temperature overshoot relative to 2100 of ~0.22 °C in *ssp119*, ~0.07 °C in *ssp126* and ~0.37 °C in *ssp534-over*. CNRM-ESM2-1 simulates in comparison a much weaker temperature overshoot relative to 2100 that is ~0.01 °C for *ssp119*, 0 °C for *ssp126*, and 0.15 °C for *ssp534-over*, which might be explained by the strong differences in ocean heat uptake as shown in Figure 16b.

Figure 16b shows the evolution of the ocean heat content in the first 700 m of the ocean relative to 1955–2005. This Figure shows that models broadly predict similar changes in ocean heat content by 2100, except for *ssp585* and all of the overshoot scenarios.

For the *ssp585*, the median outcomes from MAGICC6 in terms of ocean heat content better agree with CNRM-CM6-1 than CNRM-ESM2-1. This feature might be explained by the difference in background (pre-industrial) ocean heat content which is larger in CNRM-ESM2-1 by about 26.7 ZJ in 1850 with respect to CNRM-CM6-1. This background heat storage suggests a greater tendency of CNRM-ESM 2-1's ocean for stratification that counteracts the heat uptake over time.

For the overshoot scenarios, MAGICC6 simulates either a "plateau" or an overshoot in ocean heat content, whereas both CNRM-CM6-1 and CNRM-ESM2-1 predict a continuous accumulation of heat in the first 700 m of the ocean.

This suggests that for these scenarios, the response of the ocean to radiative forcing as simulated by either CNRM-ESM2-1 or CNRM-CM6-1 has a greater inertia than that emulated by MAGICC6.

It is hard to evaluate the realism of these features given the lack of observational records over paleoclimate period such as the Eocene-Oligocene climate transition (Lear et al., 2008; Pagani et al., 2005; Pearson et al., 2009) where the radiative forcing (such as atmospheric CO_2) decreases.

Figure 16c compares the global carbon sinks from CNRM-ESM2-1 and MAGICC6. This shows that for all scenarios except *ssp434* and *ssp534-over*, the global carbon sinks as simulated by CNRM-ESM2-1 is slightly lower than the median outcomes of MAGICC6. The mean difference over 2081 and 2100 ranges between 0.6 Pg C y^{-1} and 0.9 Pg C y^{-1}. For *ssp434* and *ssp534-over*, the median outcomes of MAGICC6 are significantly lower than that simulated by CNRM-ESM2-1 with absolute differences >1.5 Pg C y^{-1} in average over 2081–2100.

Most of these differences are attributable to the sensitivity of the carbon cycle to rising CO_2 and climate change as captured in the two models. MAGICC6 has been calibrated on the first generation of Earth system models that displayed a greater sensitivity to rising CO_2 and climate change (Friedlingstein et al., 2006). Although quite high, the response of the carbon module of CNRM-ESM2-1 to rising CO_2 and temperature remains lower than that of MAGICC6. The other difference arises from the future warming (Figure 16a) as discussed above, which influences both land and ocean carbon fluxes, enhancing the difference between MAGICC6 and CNRM-ESM2-1. In particular, differences in climate responses to non-CO_2 climate forcers can explain the difference in carbon sinks between *ssp126* and *ssp434* because these two scenarios display similar features in atmospheric CO_2 from 2014 to 2100 (temporal correlation >0.99).

Figure 17 compares the *very likely* (90%) and the *likely* (66%) range of warming in 2100 of CMIP5 models as emulated by MAGICC with respect to individual projections of CNRM-ESM2-1 and CNRM-CM6-1. Despite of the their high ECS, both CNRM-ESM2-1 and CNRM-CM6-1 simulate a warming in 2100 that remains within the 16th–84th percentiles of warming as inferred by the previous generation of climate models for high emission scenarios (itself emulated by MAGICC6). For median emission scenarios, the warming projected by CNRM-ESM2-1 and CNRM-CM6-1 in 2100 is stronger than the 16th–84th percentiles. However, this latter remains within the 90% range, that is, the 5th–95th percentiles of MAGICC6 outcomes. Contrasting with high- and medium-emission scenarios, CNRM-ESM2-1 and CNRM-CM6-1 simulate a warming in 2100 that falls outside the 90% range of MAGICC6 outcomes suggesting that deeper emission cuts are required to halt global warming below 2 °C (*ssp126*) or 1.5 °C (*ssp119*).

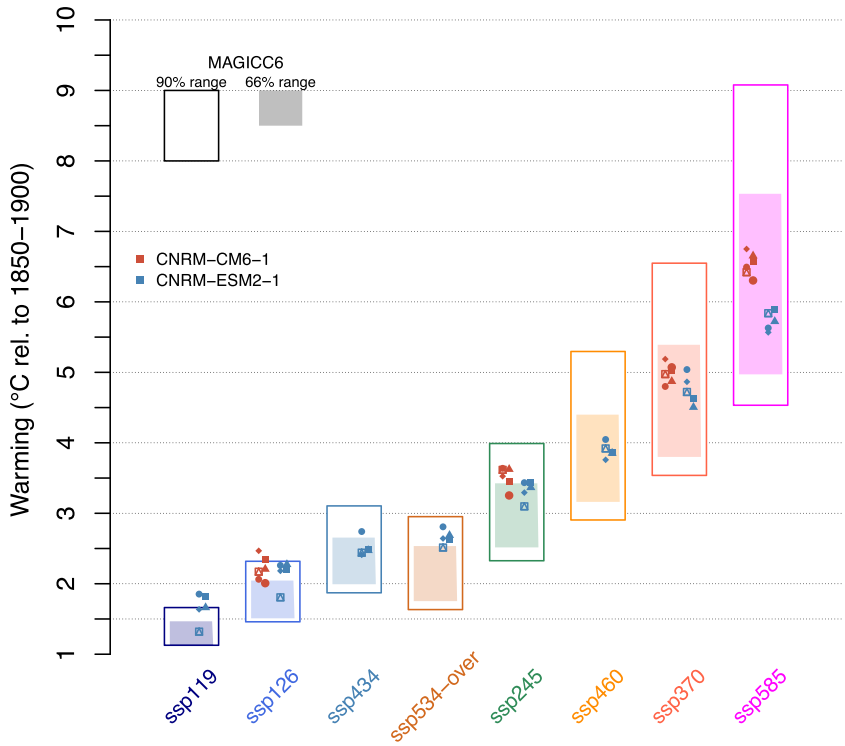

Figure 17. Global warming in 2100 as projected by CNRM-ESM2-1 and CNRM-CM6-1 for the eight scenarios of ScenarioMIP. White and gray boxes indicate the 90% (very likely) and the 66% (likely) range as emulated from MAGICC6 based on the CMIP5 model ensemble. These two ranges represent respectively the 5th–95th percentiles and the 13th–84th percentiles of the 600 global mean temperature outcomes as produced by MAGICC6 in probabilistic mode.

5. Summary and Conclusions

The first objective of this work was to describe CNRM-ESM 2-1—the Earth system model of second generation developed by CNRM-CERFACS as contribution for CMIP6. In this paper, we have described the model components and have specifically detailed the interactive Earth system components of CNRM-ESM2-1 which make this model more complex and realistic in terms of processes than its physical counterpart—the state-of-the-art AOGCM of sixth generation, CNRM-CM6-1 (Voldoire et al., 2019). The Earth system components are the interactive tropospheric aerosols, atmospheric chemistry, as well as the land and ocean carbon cycles. The first two (i.e., aerosols and chemistry) represent a major increase in the model complexity with regard to the previous generation of model (CNRM-ESM 1, Séférian, Delire, et al., 2016). The land and carbon cycles were already implemented in this former model version, but here these components have been revised and improved and show a better agreement with the observations. CNRM-ESM2-1 provides a first attempt within an ESM to bound the global carbon cycle by resolving the exchange of carbon not only between the atmosphere, land, and ocean but also between land and ocean through the aquatic continuum simulated by ISBA-CTRIP.

The second objective was to use both CNRM-ESM2-1 and CNRM-CM6-1 as a fully traceable framework to investigate how far model complexity influences the model performance over the modern period, the model response to external forcing, and the future climate projections. Indeed, these two models offer an unrivalled framework to address this question because they share the same code, the same grid resolution, and the same tuning.

In our modeling framework, we first show that the model complexity barely affects model performance over the modern period (considered to be the last 30 years before 2014). Both CNRM-CM6-1 and CNRM-ESM2-1 display comparable performance when compared against modern observations. Major differences are explained by land cover-aerosol interactions where differences in soil vegetation distributions impact dust aerosols' loads leading, in turn, to differences in surface radiation and climate.

Stronger differences are found when comparing the response of the two models to external forcing and future climate projections. We estimate that the inclusion of Earth system feedbacks reduces the ECS by ~0.5 °C for an abrupt quadrupling of atmospheric CO_2 from preindustrial level. This finding is robust either under idealistic transient scenarios (with only rising CO_2 concentration with time) or under realistic future concentrations scenarios. In either case, our analyses show that the inclusion of Earth system components revise downward future warming as projected by the AOGCM CNRM-CM6-1. Differences in the representation of land vegetation, in particular the CO_2-water-stomatal feedbacks, explains about 60% of the difference in TCR to rising CO_2. The remaining difference of ~40% is attributed to other Earth system feedbacks, especially the climate natural aerosol (i.e., dust and sea-salt) interactions that respond to climate variations in CNRM-ESM2-1 but not in CNRM-CM6-1. Nevertheless, our analyses are based on concentration-driven scenarios, which imply that climate-carbon cycle feedbacks are switched off. When switched on, our calculations suggest that climate-carbon cycle feedbacks could amplify global warming by ~16%.

Finally, the current study documents the main characteristics and behavior of CNRM models over the CMIP6 Diagnostic, Evaluation and Characterization of Klima (DECK), CMIP6 *historical*, and the ScenarioMIP future projections. Given the conclusions, this work highlights an original contribution of CNRM-CERFACS to CMIP6 and to a number of endorsed MIPs in support of IPCC assessment.

We take the opportunity to stress here that a specific effort has been made to contribute to the entire matrix of ScenarioMIP Shared Socioeconomic Pathways with CNRM-ESM2-1 future climate projections.

Ongoing developments led at CNRM-CERFACS on Earth system components aim to improve model-data comparison. They concern, for example, a better representation of the land cover-aerosol interactions but also the coupling between the air-sea exchange of trace gases and particles emitted by the ocean (e.g., DMS or organic matter) with the aerosol scheme. Future developments of CNRM-ESM will aim at better representing climate-relevant processes. For example, the inclusion of a permafrost carbon module (Morel et al., 2019) is expected to improve the representation of the soil carbon and associated CO_2 and CH_4 emissions in high latitude biomes. The representation of anthropogenic disturbances such as harvesting or irrigation is expected to be included in a future version of CNRM-ESM, improving the representation of climate-relevant human-Earth interactions. Improvements are also expected for the ocean component of CNRM-ESM where the use of a higher resolution will enable a better representation of physical-biological couplings (Berthet et al., 2019).

Data Availability Statement

All of the CNRM-ESM2-1 and CNRM-CM6-1 model outputs are available for download on ESGF under CMIP6 projects. The SURFEX-CTRIP code is available (Open-SURFEX) using a CECILL-C Licence (http://www.cecill.info/licences/Licence_CeCILL-C_V1-en.txt) at the SURFEX website (http://www.umr-cnrm.fr/surfex). NEMO-GELATO-PISCESv2-gas is also available at https://opensource.umr-cnrm.fr/; the access to the Git repository is granted upon request to the corresponding author. OASIS3-MCT can be downloaded at this website (https://verc.enes.org/oasis/download). XIOS can be downloaded at the XIOS website (https://forge.ipsl.jussieu.fr/ioserver). For the ARPEGE-Climat_v6.3 code and exact version applied to each component, please contact the authors. Finally, a number of analyzing tools developed at CNRM, or in collaboration with CNRM scientists, is available on as Open Source code (see https://opensource.cnrm-game-meteo.fr/).

Contributions

All authors contributed significantly to the writing of the paper. RS coordinated the analyses and led the writing of the paper. JV contributed to the kernel analyses. PN and MM led the analyses of aerosols and RFMIP simulations used in this work. All the authors of CNRM-CERFACS modeling group contributed to the development of CNRM-CM6-1 and CNRM-ESM2-1. The NEMO system team (GM, JD, CE, and OA) contributed to the continuous development of the NEMO ocean model. LB, OA, RS, and SB contributed to the development of the PISCES-gas branch of the PISCES biogeochemical model.

Acknowledgments

We thank Chris Jones and the anonymous reviewers for their constructive comments and suggestions about this work. This work was supported by the European Union's Horizon 2020 research and innovation program with the H2020 project CRESCENDO under the grant agreement 641816 and the H2020 CONSTRAIN under the grant agreement 820829. This work was supported by the French ANR project CONVERGENCE under grant ANR-13-MONU-0008-02 and the LEFE CYBER/GMMC PISCO project. RS thanks Meinshausen M. (MAGICC) for providing MAGICC6 output used in this work. We particularly acknowledge the support of the team in charge of the CNRM-CM climate model. Supercomputing time was provided by the Météo-France/DSI supercomputing center. RS thanks Christophe Cassou for his fruitful discussion on the paper.

References

Adler, R. F., Huffman, G. J., Chang, A., Ferraro, R., Xie, P.-P., Janowiak, J., et al. (2003). The version-2 global precipitation climatology project (GPCP) monthly precipitation analysis (1979–present). *Journal of Hydrometeorology*, *4*(6), 1147–1167. https://doi.org/10.1175/1525-7541(2003)004<1147:TVGPCP>2.0.CO;2

Anav, A., Friedlingstein, P., Kidston, M., Bopp, L., Ciais, P., Cox, P., et al. (2013). Evaluating the land and ocean components of the global carbon cycle in the CMIP5 earth system models. *Journal of Climate*, *26*(18), 6801–6843. https://doi.org/10.1175/JCLI-D-12-00417.1

Anav, A., Murray-Tortarolo, G., Friedlingstein, P., Sitch, S., Piao, S., & Zhu, Z. (2013). Evaluation of land surface models in reproducing satellite derived leaf area index over the high-latitude northern hemisphere. Part II: Earth system models. *Remote Sensing*, *5*(8), 3637–3661. https://doi.org/10.3390/rs5083637

Andrews, T., Gregory, J. M., Webb, M. J., & Taylor, K. E. (2012). Forcing, feedbacks and climate sensitivity in CMIP5 coupled atmosphere-ocean climate models. *Geophysical Research Letters*, *39*, L09712. https://doi.org/10.1029/2012GL051607

Andrews, T., Ringer, M. A., Doutriaux-Boucher, M., Webb, M. J., & Collins, W. J. (2012). Sensitivity of an Earth system climate model to idealized radiative forcing. *Geophysical Research Letters*, *39*, L10702. https://doi.org/10.1029/2012GL051942

Arora, V. K., Boer, G. J., Friedlingstein, P., Eby, M., Jones, C. D., Christian, J. R., et al. (2013). Carbon-concentration and carbon-climate feedbacks in CMIP5 earth system models. *Journal of Climate*, *26*(15), 5289–5314. https://doi.org/10.1175/JCLI-D-12-00494.1

Aumont, O., Ethé, C., Tagliabue, A., Bopp, L., & Gehlen, M. (2015). PISCES-v2: An ocean biogeochemical model for carbon and ecosystem studies. *Geoscientific Model Development*, *8*(8), 2465–2513. https://doi.org/10.5194/gmd-8-2465-2015

Beck, H. E., Van Dijk, A. I. J. M., Levizzani, V., Schellekens, J., Miralles, D. G., Martens, B., & De Roo, A. (2017). MSWEP: 3-hourly 0.25° global gridded precipitation (1979–2015) by merging gauge, satellite, and reanalysis data. *Hydrology and Earth System Sciences*, *21*(1), 589–615. https://doi.org/10.5194/hess-21-589-2017

Bernard, B., Madec, G., Penduff, T., Molines, J.-M., Treguier, A.-M., Le Sommer, J., et al. (2006). Impact of partial steps and momentum advection schemes in a global ocean circulation model at eddy-permitting resolution. *Ocean Dynamics*, *56*(5–6), 543–567. https://doi.org/10.1007/s10236-006-0082-1

Berthet, S., Séférian, R., Bricaud, C., Chevallier, M., Voldoire, A., & Ethé, C. (2019). Evaluation of an online grid-coarsening algorithm in a global eddy-admitting ocean-biogeochemical model. *Journal of Advances in Modeling Earth Systems*, *11*, 1759–1783. https://doi.org/10.1029/2019MS001644

Bianchi, D., Dunne, J. P., Sarmiento, J. L., & Galbraith, E. D. (2012). Data-based estimates of suboxia, denitrification, and N2O production in the ocean and their sensitivities to dissolved O2. *Global Biogeochemical Cycles*, *26*, GB2009. https://doi.org/10.1029/2011GB004209

Bodeker, G. E., Shiona, H., & Eskes, H. (2005). Indicators of Antarctic ozone depletion. *Atmospheric Chemistry and Physics*, *5*(10), 2603–2615. https://doi.org/10.5194/acp-5-2603-2005

Boer, G. J., Smith, D. M., Cassou, C., Doblas-Reyes, F., Danabasoglu, G., Kirtman, B., et al. (2016). The Decadal Climate Prediction Project (DCPP) contribution to CMIP6. *Geoscientific Model Development*, *9*(10), 3751–3777. https://doi.org/10.5194/gmd-9-3751-2016

Bonan, G. B., Oleson, K. W., Fisher, R. A., Lasslop, G., & Reichstein, M. (2012). Reconciling leaf physiological traits and canopy flux data: Use of the TRY and FLUXNET databases in the Community Land Model version 4. *Journal of Geophysical Research*, *117*, G02026. https://doi.org/10.1029/2011JG001913

Booth, B. B. B., Dunstone, N. J., Halloran, P. R., Andrews, T., & Bellouin, N. (2012). Aerosols implicated as a prime driver of twentieth-century North Atlantic climate variability. *Nature*, *484*(7393), 228–232. https://doi.org/10.1038/nature10946

Bouillon, R.-C. (2004). Determination of apparent quantum yield spectra of DMS photo-degradation in an in situ iron-induced Northeast Pacific Ocean bloom. *Geophysical Research Letters*, *31*, L06310. https://doi.org/10.1029/2004GL019536

Calvet, J. C., Noilhan, J., Roujean, J. L., Bessemoulin, P., Cabelguenne, M., Olioso, A., & Wigneron, J. P. (1998). An interactive vegetation SVAT model tested against data from six contrasting sites. *Agricultural and Forest Meteorology*, *92*(2), 73–95. https://doi.org/10.1016/S0168-1923(98)00091-4

Carrer, D., Meurey, C., Ceamanos, X., Roujean, J. L., Calvet, J. C., & Liu, S. (2014). Dynamic mapping of snow-free vegetation and bare soil albedos at global 1 km scale from 10-year analysis of MODIS satellite products. *Remote Sensing of Environment*, *140*, 420–432. https://doi.org/10.1016/j.rse.2013.08.041

Ciais, P., Sabine, C., Bala, G., Bopp, L., Brovkin, V., Canadell, J., et al. (2013). Carbon and other biogeochemical cycles. In T. F. Stocker, D. Qin, G.-K. Plattner, M. Tignor, S. K. Allen, J. Boschung, et al. (Eds.), *Climate Change 2013: The Physical Science Basis. Contribution of Working Group I to the Fifth Assessment Report of the Intergovernmental Panel on Climate Change*. Cambridge, United Kingdom and New York, NY, USA: Cambridge University Press.

Ciais, P., Tan, J., Wang, X., Roedenbeck, C., Chevallier, F., Piao, S.-L., et al. (2019). Five decades of northern land carbon uptake revealed by the interhemispheric CO2 gradient. *Nature*, *568*(7751), 221–225. https://doi.org/10.1038/s41586-019-1078-6

Collins, W. J., Lamarque, J.-F., Schulz, M., Boucher, O., Eyring, V., Hegglin, M. I., et al. (2017). AerChemMIP: Quantifying the effects of chemistry and aerosols in CMIP6. *Geoscientific Model Development*, *10*(2), 585–607. https://doi.org/10.5194/gmd-10-585-2017

Craig, A., Valcke, S., & Coquart, L. (2017). Development and performance of a new version of the OASIS coupler, OASIS3-MCT_3.0. *Geoscientific Model Development*, *10*(9), 3297–3308. https://doi.org/10.5194/gmd-10-3297-2017

De Noblet-Ducoudré, N., Boisier, J. P., Pitman, A., Bonan, G. B., Brovkin, V., Cruz, F., et al. (2012). Determining robust impacts of land-use-induced land cover changes on surface climate over North America and Eurasia: Results from the first set of LUCID experiments. *Journal of Climate*, *25*(9), 3261–3281. https://doi.org/10.1175/JCLI-D-11-00338.1

Decharme, B., Delire, C., Minvielle, M., Colin, J., Vergnes, J., Alias, A., et al. (2019). Recent changes in the ISBA-CTRIP land surface system for use in the CNRM-CM6 climate model and in global off-line hydrological applications. *Journal of Advances in Modeling Earth Systems*, *11*, 1207–1252. https://doi.org/10.1029/2018MS001545

Derevianko, G. J., Deutsch, C., & Hall, A. (2009). On the relationship between ocean DMS and solar radiation. *Geophysical Research Letters*, *36*, L17606. https://doi.org/10.1029/2009GL039412

DeVries, T., Le Quéré, C., Andrews, O., Berthet, S., Hauck, J., Ilyina, T., et al. (2019). Decadal trends in the ocean carbon sink. *Proceedings of the National Academy of Sciences*, 201900371. https://doi.org/10.1073/pnas.1900371116

Donohue, K. A., Tracey, K. L., Watts, D. R., Chidichimo, M. P., & Chereskin, T. K. (2016). Mean Antarctic circumpolar current transport measured in Drake Passage. *Geophysical Research Letters*, *43*, 11,760–11,767. https://doi.org/10.1002/2016GL070319

Dunne, J. P., Sarmiento, J. L., & Gnanadesikan, A. (2007). A synthesis of global particle export from the surface ocean and cycling through the ocean interior and on the seafloor. *Global Biogeochemical Cycles*, *21*, GB4006. https://doi.org/10.1029/2006GB002907

ECMWF, S. P (2014). *In IFS documentation CY40r1 Part IV: Physical processes*, (pp. 111–113). Reading, UK: ECMWF.

Eyring, V., Arblaster, J. M., Cionni, I., Sedláček, J., Perlwitz, J., Young, P. J., et al. (2013). Long-term ozone changes and associated climate impacts in CMIP5 simulations. *Journal of Geophysical Research: Atmospheres*, *118*, 5029–5060. https://doi.org/10.1002/jgrd.50316

Eyring, V., Bony, S., Meehl, G. A., Senior, C. A., Stevens, B., Stouffer, R. J., & Taylor, K. E. (2016). Overview of the Coupled Model Intercomparison Project Phase 6 (CMIP6) experimental design and organization. *Geoscientific Model Development*, *9*(5), 1937–1958. https://doi.org/10.5194/gmd-9-1937-2016

Fan, Y., & van den Dool, H. (2008). A global monthly land surface air temperature analysis for 1948-present. *Journal of Geophysical Research*, *113*, D01103. https://doi.org/10.1029/2007JD008470

Faroux, S., Kaptué Tchuenté, A. T., Roujean, J.-L., Masson, V., Martin, E., & Le Moigne, P. (2013). ECOCLIMAP-II/Europe: A twofold database of ecosystems and surface parameters at 1 km resolution based on satellite information for use in land surface, meteorological and climate models. *Geoscientific Model Development*, *6*(2), 563–582. https://doi.org/10.5194/gmd-6-563-2013

Fetterer, F., Knowles, K., Meier, W., & Savoie, M. (2002). Sea Ice Index, digital media (updated 20). Boulder, Colorado USA: NASA DAAC at the National Snow and Ice Data Center. Boulder, Colorado USA: National Snow and Ice Data Center. Retrieved from https://doi.org/10.7265/N5QJ7F7W

Flato, G., Marotzke, J., Abiodun, B., Braconnot, P., Chou, S. C., Collins, W., et al. (2013). Evaluation of climate models. In T. F. Stocker, D. Qin, G.-K. Plattner, M. Tignor, S. K. Allen, J. Boschung, et al. (Eds.), *Climate Change 2013: The Physical Science Basis. Contribution of Working Group I to the Fifth Assessment Report of the Intergovernmental Panel on Climate Change*. Cambridge, United Kingdom and New York, NY, USA: Cambridge University Press.

Friedlingstein, P., Cox, P., Betts, R., Bopp, L., von Bloh, W., Brovkin, V., et al. (2006). Climate-carbon cycle feedback analysis: Results from the C4MIP model intercomparison. *Journal of Climate*, *19*(14), 3337–3353. https://doi.org/10.1175/JCLI3800.1

Friedlingstein, P., Meinshausen, M., Arora, V. K., Jones, C. D., Anav, A., Liddicoat, S. K., & Knutti, R. (2014). Uncertainties in CMIP5 climate projections due to carbon cycle feedbacks. *Journal of Climate*, *27*(2), 511–526. https://doi.org/10.1175/JCLI-D-12-00579.1

Garcia, H. E., Locarnini, R. A., Boyer, T. P., Antonov, J. I., Baranova, O. K., Zweng, M. M., et al. (2014a). In S. Levitus, & A. Mishonov (Eds.), *World ocean atlas 2013, Volume 4: Dissolved inorganic nutrients (phosphate, nitrate, silicate)*, NOAA Atlas NESDIS, (Vol. *76*, p. 25).

Garcia, H. E., Locarnini, R. A., Boyer, T. P., Antonov, J. I., Baranova, O. K., Zweng, M. M., et al. (2014b). In S. Levitus, & A. Mishonov (Eds.), *World ocean atlas 2013, Volume 3: Dissolved oxygen, apparent oxygen utilization, and oxygen saturation*, NOAA Atlas NESDIS, (Vol. *75*, p. 27).

Geider, R. J., Maclntyre, H. L., & Kana, T. M. (1998). A dynamic regulatory model of phytoplanktonic acclimation to light, nutrients, and temperature. *Limnology and Oceanography*, *43*(4), 679–694. https://doi.org/10.4319/lo.1998.43.4.0679

Geoffroy, O., Saint-Martin, D., & Ribes, A. (2012). Quantifying the sources of spread in climate change experiments. *Geophysical Research Letters*, *39*, L24703. https://doi.org/10.1029/2012GL054172

Gibelin, A. L., Calvet, J. C., Roujean, J. L., Jarlan, L., & Los, S. O. (2006). Ability of the land surface model ISBA-A-gs to simulate leaf area index at the global scale: Comparison with satellites products. *Journal of Geophysical Research*, *111*, D18102. https://doi.org/10.1029/2005JD006691

Gibelin, A. L., Calvet, J. C., & Viovy, N. (2008). Modelling energy and CO2 fluxes with an interactive vegetation land surface model-Evaluation at high and middle latitudes. *Agricultural and Forest Meteorology*, *148*(10), 1611–1628. https://doi.org/10.1016/j.agrformet.2008.05.013

Gillett, N. P., Arora, V. K., Matthews, D., & Allen, M. R. (2013). Constraining the ratio of global warming to cumulative CO2 emissions using CMIP5 simulations. *Journal of Climate*, *26*(18), 6844–6858. https://doi.org/10.1175/JCLI-D-12-00476.1

Gillett, N. P., Shiogama, H., Funke, B., Hegerl, G., Knutti, R., Matthes, K., et al. (2016). The Detection and Attribution Model Intercomparison Project (DAMIP v1.0) contribution to CMIP6. *Geoscientific Model Development*, *9*(10), 3685–3697. https://doi.org/10.5194/gmd-9-3685-2016

Gleckler, P. J., Durack, P. J., Stouffer, R. J., Johnson, G. C., & Forest, C. E. (2016). Industrial-era global ocean heat uptake doubles in recent decades. *Nature Climate Change*, *6*(4), 394–398. https://doi.org/10.1038/nclimate2915

Gregory, J. M., Bouttes, N., Griffies, S. M., Haak, H., Hurlin, W. J., Jungclaus, J., et al. (2016). The Flux-Anomaly-Forced Model Intercomparison Project (FAFMIP) contribution to CMIP6: Investigation of sea-level and ocean climate change in response to CO₂ forcing. *Geoscientific Model Development*, *9*(11), 3993–4017. https://doi.org/10.5194/gmd-9-3993-2016

Gregory, J. M., Ingram, W. J., Palmer, M. A., Jones, G. S., Stott, P. A., Thorpe, R. B., et al. (2004). A new method for diagnosing radiative forcing and climate sensitivity. *Geophysical Research Letters*, *31*, L03205. https://doi.org/10.1029/2003GL018747

Griffies, S. M., Danabasoglu, G., Durack, P. J., Adcroft, A. J., Balaji, V., Böning, C. W., et al. (2016). OMIP contribution to CMIP6: Experimental and diagnostic protocol for the physical component of the Ocean Model Intercomparison Project. *Geoscientific Model Development*, *9*(9), 3231–3296. https://doi.org/10.5194/gmd-9-3231-2016

Grythe, H., Ström, J., Krejci, R., Quinn, P., & Stohl, A. (2014). A review of sea-spray aerosol source functions using a large global set of sea salt aerosol concentration measurements. *Atmospheric Chemistry and Physics*, *14*(3), 1277–1297. https://doi.org/10.5194/acp-14-1277-2014

Gupta, P., Remer, L. A., Levy, R. C., & Mattoo, S. (2018). Validation of MODIS 3 km land aerosol optical depth from NASA's EOS Terra and Aqua missions. *Atmospheric Measurement Techniques*, *11*(5), 3145–3159. https://doi.org/10.5194/amt-11-3145-2018

Haarsma, R. J., Roberts, M. J., Vidale, P. L., Senior, C. A., Bellucci, A., Bao, Q., et al. (2016). High Resolution Model Intercomparison Project (HighResMIP v1.0) for CMIP6. *Geoscientific Model Development*, *9*(11), 4185–4208. https://doi.org/10.5194/gmd-9-4185-2016

Hansen, J., Sato, M., Ruedy, R., Nazarenko, L., Lacis, A., Schmidt, G. A., et al. (2005). Efficacy of climate forcings. *Journal of Geophysical Research*, *110*, D18104. https://https://doi.org/10.1029/2005JD005776

Harris, I., Jones, P. D., Osborn, T. J., & Lister, D. H. (2014). Updated high-resolution grids of monthly climatic observations - the CRU TS3.10 Dataset. *International Journal of Climatology*, *34*(3), 623–642. https://doi.org/10.1002/joc.3711

Hoesly, R. M., Smith, S. J., Feng, L., Klimont, Z., Janssens-Maenhout, G., Pitkanen, T., et al. (2018). Historical (1750–2014) anthropogenic emissions of reactive gases and aerosols from the Community Emissions Data System (CEDS). *Geoscientific Model Development*, *11*(1), 369–408. https://doi.org/10.5194/gmd-11-369-2018

Holte, J., Talley, L. D., Gilson, J., & Roemmich, D. (2017). An Argo mixed layer climatology and database. *Geophysical Research Letters*, *44*, 5618–5626. https://doi.org/10.1002/2017GL073426

Huang, B., Thorne, P. W., Banzon, V. F., Boyer, T., Chepurin, G., Lawrimore, J. H., et al. (2017). Extended reconstructed sea surface temperature, version 5 (ERSSTv5): Upgrades, validations, and intercomparisons. *Journal of Climate*, *30*(20), 8179–8205. https://doi.org/10.1175/JCLI-D-16-0836.1

Huffman, G. J., Bolvin, D. T., Nelkin, E. J., Wolff, D. B., Adler, R. F., Gu, G., et al. (2007). The TRMM multisatellite precipitation analysis (TMPA): Quasi-global, multiyear, combined-sensor precipitation estimates at fine scales. *Journal of Hydrometeorology*, *8*(1), 38–55. https://doi.org/10.1175/JHM560.1

Huntzinger, D. N., Michalak, A. M., Schwalm, C., Ciais, P., King, A. W., Fang, Y., et al. (2017). Uncertainty in the response of terrestrial carbon sink to environmental drivers undermines carbon-climate feedback predictions. *Scientific Reports*, *7*(1), 4765. https://doi.org/10.1038/s41598-017-03818-2

Huntzinger, D. N., Schwalm, C., Michalak, A. M., Schaefer, K., King, A. W., Wei, Y., et al. (2013). The North American carbon program multi-scale synthesis and terrestrial model intercomparison project - Part 1: Overview and experimental design. *Geoscientific Model Development*, *6*(6), 2121–2133. https://doi.org/10.5194/gmd-6-2121-2013

Hurtt, G. C., Frolking, S., Fearon, M. G., Moore, B., Shevliakova, E., Malyshev, S., et al. (2006). The underpinnings of land-use history: Three centuries of global gridded land-use transitions, wood-harvest activity, and resulting secondary lands. *Global Change Biology*, *12*(7), 1208–1229. https://doi.org/10.1111/j.1365-2486.2006.01150.x

HWSD. (2012). Harmonized World Soil Database version 1.21. *World Harmonized Soil Database*. FAO, Rome, Italy and IIASA, Laxenburg, Austria. Retrieved from http://webarchive.iiasa.ac.at/Research/LUC/External-World-soil-database/HTML/HWSD_Data.html?sb=4

IPCC (2007). Climate Change 2007: The physical science basis. In S. Solomon, D. Qin, M. Manning, Z. Chen, M. Marquis, K. B. Averyt, et al. (Eds.), *Contribution of working group I to the fourth assessment report of the intergovernmental panel on climate change*, (p. 996). Cambridge, United Kingdom and New York, NY, USA: Cambridge University Press.

IPCC (2013). Climate change 2013: The physical science basis. In T. F. Stocker, D. Qin, G.-K. Plattner, M. Tignor, S. K. Allen, J. Boschung, et al. (Eds.), *Contribution of Working Group I to the Fifth Assessment Report of the Intergovernmental Panel on Climate Change*, (p. 1535). Cambridge, United Kingdom and New York, NY, USA: Cambridge University Press.

Ito, T., Woloszyn, M., & Mazloff, M. (2010). Anthropogenic carbon dioxide transport in the Southern Ocean driven by Ekman flow. *Nature*, *463*(7277), 80–83. https://doi.org/10.1038/nature08687

Jacobs, C. M. J., van den Hurk, B. M. M., & de Bruin, H. A. R. (1996). Stomatal behaviour and photosynthetic rate of unstressed grapevines in semi-arid conditions. *Agricultural and Forest Meteorology*, *80*(2–4), 111–134. https://doi.org/10.1016/0168-1923(95)02295-3

Jaeglé, L., Quinn, P. K., Bates, T. S., Alexander, B., & Lin, J.-T. (2011). Global distribution of sea salt aerosols: new constraints from in situ and remote sensing observations. *Atmospheric Chemistry and Physics*, *11*(7), 3137–3157. https://doi.org/10.5194/acp-11-3137-2011

Jin, X., & Gruber, N. (2003). Offsetting the radiative benefit of ocean iron fertilization by enhancing N_2O emissions. *Geophysical Research Letters*, *30*(24), 2249. https://doi.org/10.1029/2003GL018458

Joetzjer, E., Delire, C., Douville, H., Ciais, P., Decharme, B., Carrer, D., et al. (2015). Improving the ISBA CC land surface model simulation of water and carbon fluxes and stocks over the Amazon forest. *Geoscientific Model Development*, *8*(6), 1709–1727. https://doi.org/10.5194/gmd-8-1709-2015

Jones, C., Robertson, E., Arora, V., Friedlingstein, P., Shevliakova, E., Bopp, L., et al. (2013). Twenty-first-century compatible co2 emissions and airborne fraction simulated by cmip5 earth system models under four representative concentration pathways. *Journal of Climate*, *26*(13), 4398–4413. https://doi.org/10.1175/JCLI-D-12-00554.1

Jones, C. D., Arora, V., Friedlingstein, P., Bopp, L., Brovkin, V., Dunne, J., et al. (2016). C4MIP-The Coupled Climate-Carbon Cycle Model Intercomparison Project: Experimental protocol for CMIP6. *Geoscientific Model Development*, *9*(8), 2853–2880. https://doi.org/10.5194/gmd-9-2853-2016

Jones, C. D., Frölicher, T. L., Koven, C., MacDougall, A. H., Matthews, H. D., Zickfeld, K., et al. (2019). The Zero Emission Commitment Model Intercomparison Project (ZECMIP) contribution to CMIP6: Quantifying committed climate changes following zero carbon emissions. *Geoscientific Model Development Discussion*, *12*(10), 4375–4385. https://doi.org/10.5194/gmd-2019-153

Kageyama, M., Braconnot, P., Harrison, S. P., Haywood, A. M., Jungclaus, J. H., Otto-Bliesner, B. L., et al. (2018). The PMIP4 contribution to CMIP6—Part 1: Overview and over-arching analysis plan. *Geoscientific Model Development*, *11*(3), 1033–1057. https://doi.org/10.5194/gmd-11-1033-2018

Kahru, M., Leppanen, J.-M., & Rud, O. (1993). Cyanobacterial blooms cause heating of the sea surface. *Marine Ecology Progress Series*, *101*, 1–7. https://doi.org/10.3354/meps101001

Karl, T. R., Arguez, A., Huang, B., Lawrimore, J. H., McMahon, J. R., Menne, M. J., et al. (2015). Possible artifacts of data biases in the recent global surface warming hiatus. *Science*, *348*(6242), 1469–1472. https://doi.org/10.1126/science.aaa5632

Kattge, J., Díaz, S., Lavorel, S., Prentice, I. C., Leadley, P., Bönisch, G., et al. (2011). TRY - a global database of plant traits. *Global Change Biology*, *17*(9), 2905–2935. https://doi.org/10.1111/j.1365-2486.2011.02451.x

Keenan, T. F. T. F., Prentice, I. C., Canadell, J. G., Williams, C. A., Wang, H., Raupach, M. R., & Collatz, G. J. (2016). Recent pause in the growth rate of atmospheric CO2 due to enhanced terrestrial carbon uptake. *Nature Communications*, *7*(13428), 1. https://doi.org/10.1038/ncomms13428

Keller, D. P., Lenton, A., Scott, V., Vaughan, N. E., Bauer, N., Ji, D., et al. (2018). The Carbon Dioxide Removal Model Intercomparison Project (CDRMIP): Rationale and experimental protocol for CMIP6. *Geoscientific Model Development*, *11*(3), 1133–1160. https://doi.org/10.5194/gmd-11-1133-2018

Kettle, A. J., Andreae, M. O., Amouroux, D., Andreae, T. W., Bates, T. S., Berresheim, H., et al. (1999). A global database of sea surface dimethylsulfide (DMS) measurements and a procedure to predict sea surface DMS as a function of latitude, longitude, and month. *Global Biogeochemical Cycles*, *13*(2), 399–444. https://doi.org/10.1029/1999GB900004

Key, R. M., Olsen, A., van Heuven, S., Lauvset, S. K., Velo, A., Lin, X., et al. (2015). Global Ocean Data Analysis Project, Version 2 (GLODAPv2). *Ornl/Cdiac-162, Ndp-093*. *Earth System Science Data*, *8*(2), 297–323. https://doi.org/10.3334/CDIAC/OTG.NDP093_GLODAPv2

Knutti, R., Masson, D., & Gettelman, A. (2013). Climate model genealogy: Generation CMIP5 and how we got there. *Geophysical Research Letters*, *40*, 1194–1199. https://doi.org/10.1002/grl.50256

Kok, J. F. (2011). A scaling theory for the size distribution of emitted dust aerosols suggests climate models underestimate the size of the global dust cycle. *Proceedings of the National Academy of Sciences*, *108*(3), 1016–1021. https://doi.org/10.1073/pnas.1014798108

Körtzinger, A., Hedges, J. I., & Quay, P. D. (2001). Redfield ratios revisited: Removing the biasing effect of anthropogenic CO2. *Limnology and Oceanography*, *46*(4), 964–970. https://doi.org/10.4319/lo.2001.46.4.0964

Kravitz, B., Robock, A., Tilmes, S., Boucher, O., English, J. M., Irvine, P. J., et al. (2015). The geoengineering model intercomparison project phase 6 (GeoMIP6): Simulation design and preliminary results. *Geoscientific Model Development*, *8*(10), 3379–3392. https://doi.org/10.5194/gmd-8-3379-2015

Landschützer, P., Gruber, N., & Bakker, D. C. E. (2016). Decadal variations and trends of the global ocean carbon sink. *Global Biogeochemical Cycles*, *30*, 1396–1417. https://doi.org/10.1002/2015GB005359

Lauvset, S. K., Key, R. M., Olsen, A., Van Heuven, S., Velo, A., Lin, X., et al. (2016). A new global interior ocean mapped climatology: The 1° × 1° GLODAP version 2. *Earth System Science Data*, *8*(2), 325–340. https://doi.org/10.5194/essd-8-325-2016

Lawrence, D. M., Hurtt, G. C., Arneth, A., Brovkin, V., Calvin, K. V., Jones, A. D., et al. (2016). The Land Use Model Intercomparison Project (LUMIP) contribution to CMIP6: Rationale and experimental design. *Geoscientific Model Development*, *9*(9), 2973–2998. https://doi.org/10.5194/gmd-9-2973-2016

Le Moigne, P., Colin, J., & Decharme, B. (2016). Impact of lake surface temperatures simulated by the FLake scheme in the CNRM-CM5 climate model. *Tellus Series A: Dynamic Meteorology and Oceanography*, *68*(1), 31274. https://doi.org/10.3402/tellusa.v68.31274

Le Quéré, C., Andrew, R. M., Friedlingstein, P., Sitch, S., Hauck, J., Pongratz, J., et al. (2018). Global carbon budget 2018. *Earth System Science Data*, *10*(4), 2141–2194. https://doi.org/10.5194/essd-10-2141-2018

Lear, C. H., Bailey, T. R., Pearson, P. N., Coxall, H. K., & Rosenthal, Y. (2008). Cooling and ice growth across the Eocene-Oligocene transition. *Geology*, *36*(3), 251–254. https://doi.org/10.1130/G24584A.1

Lee, Y. J., Matrai, P. A., Friedrichs, M. A. M., Saba, V. S., Aumont, O., Babin, M., et al. (2016). Net primary productivity estimates and environmental variables in the Arctic Ocean: An assessment of coupled physical-biogeochemical models. *Journal of Geophysical Research: Oceans*, *121*, 8635–8669. https://doi.org/10.1002/2016JC011993

Lengaigne, M., Madec, G., Bopp, L., Menkes, C., Aumont, O., & Cadule, P. (2009). Bio-physical feedbacks in the Arctic Ocean using an Earth system model. *Geophysical Research Letters*, *36*, L21602. https://doi.org/10.1029/2009GL040145

Lengaigne, M., Menkes, C., Aumont, O., Gorgues, T., Bopp, L., André, J. M., & Madec, G. (2007). Influence of the oceanic biology on the tropical Pacific climate in a coupled general circulation model. *Climate Dynamics*, *28*(5), 503, https://doi.org/10.1007/s00382-006-0200-2–516.

Levitus, S., Antonov, J. I., Boyer, T. P., Baranova, O. K., Garcia, H. E., Locarnini, R. A., et al. (2012). World ocean heat content and thermosteric sea level change (0–2,000 m), 1955-2010. *Geophysical Research Letters*, *39*, L10603. https://doi.org/10.1029/2012GL051106

Levy, M., Bopp, L., Karleskind, P., Resplandy, L., Ethe, C., & Pinsard, F. (2013). Physical pathways for carbon transfers between the surface mixed layer and the ocean interior. *Global Biogeochemical Cycles*, *27*, 1001–1012. https://doi.org/10.1002/gbc.20092

Levy, R. C., Mattoo, S., Munchak, L. A., Remer, L. A., Sayer, A. M., Patadia, F., & Hsu, N. C. (2013). The Collection 6 MODIS aerosol products over land and ocean. *Atmospheric Measurement Techniques*, *6*(11), 2989–3034. https://doi.org/10.5194/amt-6-2989-2013

Locarnini, R. A., Mishonov, A. V., Antonov, J. I., Boyer, T. P., Garcia, H. E., Baranova, O. K., et al. (2013). In S. Levitus, & A. Mishonov (Eds.), *World ocean atlas 2013, Volume 1: Temperature*, NOAA Atlas NESDIS, (Vol. *73*, p. 40).

Ludwig, W., Probst, J.-L., & Kempe, S. (1996). Predicting the oceanic input of organic carbon by continental erosion. *Global Biogeochemical Cycles*, *10*(1), 23–41. https://doi.org/10.1029/95GB02925

Madec, G., Bourdallé-Badie, R., Bouttier, P-A., Bricaud, C., Bruciaferri, D., Calvert, D., et al. (2017). NEMO ocean engine. https://doi.org/10.5281/ZENODO.1472492

Marticorena, B., & Bergametti, G. (1995). Modeling the atmospheric dust cycle: 1. Design of a soil-derived dust emission scheme. *Journal of Geophysical Research*, *100*(D8), 16415–16430. https://doi.org/10.1029/95JD00690

Martinez-Rey, J., Bopp, L., Gehlen, M., Tagliabue, A., & Gruber, N. (2015). Projections of oceanic N2O emissions in the 21st century using the IPSL Earth system model. *Biogeosciences*, *12*(13), 4133–4148. https://doi.org/10.5194/bg-12-4133-2015

Masotti, I., Belviso, S., Bopp, L., Tagliabue, A., & Bucciarelli, E. (2016). Effects of light and phosphorus on summer DMS dynamics in subtropical waters using a global ocean biogeochemical model. *Environmental Chemistry*, *13*(2), 379–389. https://doi.org/10.1071/EN14265

Masson, V., Champeaux, J. L., Chauvin, F., Meriguet, C., & Lacaze, R. (2003). A global database of land surface parameters at 1-km resolution in meteorological and climate models. *Journal of Climate*, *16*(9), 1261–1282. https://doi.org/10.1175/1520-0442-16.9.1261

Massonnet, F., Fichefet, T., Goosse, H., Bitz, C. M., Philippon-Berthier, G., Holland, M. M., & Barriat, P. Y. (2012). Constraining projections of summer Arctic sea ice. *The Cryosphere*, *6*(6), 1383–1394. https://doi.org/10.5194/tc-6-1383-2012

Mathiot, P., Jenkins, A., Harris, C., & Madec, G. (2017). Explicit representation and parametrised impacts of under ice shelf seas in the z*-coordinate ocean model NEMO 3.6. *Geoscientific Model Development*, *10*(7), 2849–2874. https://doi.org/10.5194/gmd-10-2849-2017

Matthes, K., Funke, B., Andersson, M. E., Barnard, L., Beer, J., Charbonneau, P., et al. (2017). Solar forcing for CMIP6 (v3.2). *Geoscientific Model Development*, *10*(6), 2247–2302. https://doi.org/10.5194/gmd-10-2247-2017

Maycock, A. C., Matthes, K., Tegtmeier, S., Schmidt, H., Thiéblemont, R., Hood, L., et al. (2018). The representation of solar cycle signals in stratospheric ozone—Part~2: Analysis of global models. *Atmospheric Chemistry and Physics*, *18*(15), 11323–11343. https://doi.org/10.5194/acp-18-11323-2018

Maycock, A. C., Randel, W. J., Steiner, A. K., Karpechko, A. Y., Christy, J., Saunders, R., et al. (2018). Revisiting the mystery of recent stratospheric temperature trends. *Geophysical Research Letters*, *45*, 9919–9933. https://doi.org/10.1029/2018GL078035

Mayorga, E., Seitzinger, S. P., Harrison, J. A., Dumont, E., Beusen, A. H. W., Bouwman, A. F., et al. (2010). Global nutrient export from WaterSheds 2 (NEWS 2): Model development and implementation. *Environmental Modelling and Software*, *25*(7), 837–853. https://doi.org/10.1016/j.envsoft.2010.01.007

McCarthy, G. D., Smeed, D. A., Johns, W. E., Frajka-Williams, E., Moat, B. I., Rayner, D., et al. (2015). Measuring the Atlantic Meridional Overturning Circulation at 26°N. *Progress in Oceanography*, *130*, 91–111. https://doi.org/10.1016/j.pocean.2014.10.006

Meijers, A. J. S. (2014). The Southern Ocean in the coupled model intercomparison project phase 5. *Philosophical Transactions of the Royal Society A: Mathematical, Physical and Engineering Sciences*, *372*(2019). https://doi.org/10.1098/rsta.2013.0296

Meinen, C. S., Johns, W. E., Moat, B. I., Smith, R. H., Johns, E. M., Rayner, D., et al. (2019). Structure and variability of the Antilles Current at 26.5°N. *Journal of Geophysical Research: Oceans*, *124*, 3700–3723. https://doi.org/10.1029/2018jc014836

Meinshausen, M., Vogel, E., Nauels, A., Lorbacher, K., Meinshausen, N., Etheridge, D. M., et al. (2017). Historical greenhouse gas concentrations for climate modelling (CMIP6). *Geoscientific Model Development*, *10*(5), 2057–2116. https://doi.org/10.5194/gmd-10-2057-2017

Meinshausen, M., Wigley, T. M. L., & Raper, S. C. B. (2011). Emulating atmosphere-ocean and carbon cycle models with a simpler model, MAGICC6—Part 2: Applications. *Atmospheric Chemistry and Physics*, *11*(4), 1457–1471. https://doi.org/10.5194/acp-11-1457-2011

Menon, S., Del Genio, A. D., Koch, D., & Tselioudis, G. (2002). {GCM} simulations of the aerosol indirect effect: {S}ensitivity to cloud parameterization and aerosol burden. *Journal of the Atmospheric Sciences*, *59*(3), 692–713.

Meurdesoif Y (2018). Xios fortran reference guide. IPSL, http://forge.ipsl.jussieu.fr/ioserver/svn/XIOS/trunk/doc/XIOS_reference_guide.pdf

Michou, M., Nabat, P., & Saint-Martin, D. (2015). Development and basic evaluation of a prognostic aerosol scheme (v1) in the CNRM climate model CNRM-CM6. *Geoscientific Model Development*, *8*(3), 501–531. https://doi.org/10.5194/gmd-8-501-2015

Michou, M., Saint-Martin, D., Teyssèdre, H., Alias, A., Karcher, F., Olivié, D., et al. (2011). A new version of the CNRM chemistry-climate model, CNRM-CCM: Description and improvements from the CCMVal-2 simulations. *Geoscientific Model Development*, *4*(4), 873–900. https://doi.org/10.5194/gmd-4-873-2011

Middelburg, J. J., Soetaert, K., Herman, P. M. J., & Heip, C. H. R. (1996). Denitrification in marine systems: A model study. *Global Biogeochemical Cycles*, *10*(4), 661–673. Retrieved from http://links.isiglobalnet2.com/gateway/Gateway.cgi? GWVersion = 2& SrcAuth = mekentosj&SrcApp = Papers&DestLinkType = FullRecord&DestApp = WOS&KeyUT = A1996VV17500008

Mignot, J., Swingedouw, D., Deshayes, J., Marti, O., Talandier, C., Séférian, R., et al. (2013). On the evolution of the oceanic component of the IPSL climate models from CMIP3 to CMIP5: A mean state comparison. *Ocean Modelling*, *72*(0 SP-EP-PY-T2-), 167–184. https://doi.org/10.1016/j.ocemod.2013.09.001

Miralles, D. G., Gentine, P., Seneviratne, S. I., & Teuling, A. J. (2019). Land–atmospheric feedbacks during droughts and heatwaves: State of the science and current challenges. *Annals of the New York Academy of Sciences*, *1436*(1), 19–35. https://doi.org/10.1111/nyas.13912

Morcrette, J.-J., Boucher, O., Jones, L., Salmond, D., Bechtold, P., Beljaars, A., et al. (2009). Aerosol analysis and forecast in the European Centre for Medium-Range Weather Forecasts Integrated Forecast System: Forward modeling. *Journal of Geophysical Research*, *114*, D06206. https://doi.org/10.1029/2008JD011235

Morel, X., Decharme, B., Delire, C., Krinner, G., Lund, M., Hansen, B. U., & Mastepanov, M. (2019). A new process-based soil methane scheme: Evaluation over Arctic field sites with the ISBA land surface model. *Journal of Advances in Modeling Earth Systems*, *11*, 293–326. https://doi.org/10.1029/2018MS001329

Morgenstern, O., Hegglin, M. I., Rozanov, E., O'Connor, F. M., Abraham, N. L., Akiyoshi, H., et al. (2017). Review of the global models used within phase 1 of the Chemistry-Climate Model Initiative (CCMI). *Geoscientific Model Development*, *10*(2), 639–671. https://doi.org/10.5194/gmd-10-639-2017

Morice, C. P., Kennedy, J. J., Rayner, N. A., & Jones, P. D. (2012). Quantifying uncertainties in global and regional temperature change using an ensemble of observational estimates: The HadCRUT4 data set. *Journal of Geophysical Research*, *117*, D08101. https://doi.org/10.1029/2011JD017187

Muller, R. A., Curry, J., Groom, D., Jacobsen, R., Perlmutter, S., Rohde, R., et al. (2013). Decadal variations in the global atmospheric land temperatures. *Journal of Geophysical Research: Atmospheres*, *118*, 5280–5286. https://doi.org/10.1002/jgrd.50458

Muller, A. R., Rohde, R., Jacobsen, R., Muller, E., & Wickham, C. (2013). A new estimate of the average earth surface land temperature spanning 1753 to 2011. *Geoinformatics & Geostatistics: An Overview*, *01*(01), 1. https://doi.org/10.4172/2327-4581.1000101

Myhre, G., Shindell, D., Bréon, F.-M., Collins, W., Fuglestvedt, J., Huang, J., et al. (2013a). Anthropogenic and natural radiative forcing. In T. F. Stocker, D. Qin, G.-K. Plattner, M. Tignor, S. K. Allen, J. Boschung, et al. (Eds.), *Climate Change 2013: The Physical Science Basis. Contribution of Working Group I to the Fifth Assessment Report of the Intergovernmental Panel on Climate Change*. Cambridge, United Kingdom and New York, NY, USA: Cambridge University Press.

Myhre, G., D. Shindell, F.-M. Bréon, W. Collins, J. Fuglestvedt, J. Huang, et al., 2013b: Anthropogenic and natural radiative forcing supplementary material. In: Stocker, T.F., D. Qin, G.-K. Plattner, M. Tignor, S.K. Allen, J. Boschung, et al. (Eds.), *Climate Change 2013: The Physical Science Basis. Contribution of Working Group I to the Fifth Assessment Report of the Intergovernmental Panel on Climate Change*. Cambridge University Press, Cambridge. Available from www.climatechange2013.org and www.ipcc.ch.

Nabat, P., Somot, S., Mallet, M., Michou, M., Sevault, F., Driouech, F., et al. (2015). Dust aerosol radiative effects during summer 2012 simulated with a coupled regional aerosol–atmosphere–ocean model over the Mediterranean. *Atmospheric Chemistry and Physics*, *15*(6), 3303–3326. https://doi.org/10.5194/acp-15-3303-2015

Notz, D., Jahn, A., Holland, M., Hunke, E., Massonnet, F., Stroeve, J., et al. (2016). The CMIP6 Sea-Ice Model Intercomparison Project (SIMIP): Understanding sea ice through climate-model simulations. *Geoscientific Model Development*, *9*(9), 3427–3446. https://doi.org/10.5194/gmd-9-3427-2016

Nowicki, S. M. J., Payne, A., Larour, E., Seroussi, H., Goelzer, H., Lipscomb, W., et al. (2016). Ice Sheet Model Intercomparison Project (ISMIP6) contribution to CMIP6. *Geoscientific Model Development*, *9*(12), 4521–4545. https://doi.org/10.5194/gmd-9-4521-2016

Olbers, D., Borowski, D., Völker, C., & Wölff, J.-O. (2004). The dynamical balance, transport and circulation of the Antarctic Circumpolar Current. *Antarctic Science*, *16*(4), 439–470. https://doi.org/10.1017/s0954102004002251

Olsen, A., Key, R. M., van Heuven, S., Lauvset, S. K., Velo, A., Lin, X., et al. (2016). The Global Ocean Data Analysis Project Version 2 (GLODAPv2)—an internally consistent data product for the world ocean. *Earth System Science Data*, *8*(2), 297–323. https://doi.org/10.5194/essd-8-297-2016

O'Neill, B. C., Tebaldi, C., van Vuuren, D. P., Eyring, V., Friedlingstein, P., Hurtt, G., et al. (2016). The Scenario Model Intercomparison Project (ScenarioMIP) for CMIP6. *Geoscientific Model Development*, *9*(9), 3461–3482. https://doi.org/10.5194/gmd-9-3461-2016

Orr, J. C., & Epitalon, J. M. (2015). Improved routines to model the ocean carbonate system: Mocsy 2.0. *Geoscientific Model Development*, *8*(3), 485–499. https://doi.org/10.5194/gmd-8-485-2015

Pagani, M., Zachos, J. C., Freeman, K. H., Tipple, B., & Bohaty, S. (2005). Atmospheric science: Marked decline in atmospheric carbon dioxide concentrations during the Paleogene. *Science*, *309*(5734), 600–603. https://doi.org/10.1126/science.1110063

Parton, W. J., Stewart, J. W. B., & Cole, C. V. (1988). Dynamics of C, N, P and S in grassland soils: A model. *Biogeochemistry*, *5*(1), 109–131. https://doi.org/10.1007/BF02180320

Pearson, P. N., Foster, G. L., & Wade, B. S. (2009). Atmospheric carbon dioxide through the Eocene-Oligocene climate transition. *Nature*, *461*(7267), 1110–1113. https://doi.org/10.1038/nature08447

Petrenko, M., Kahn, R., Chin, M., & Limbacher, J. (2017). Refined use of satellite aerosol optical depth snapshots to constrain biomass burning emissions in the GOCART model. *Journal of Geophysical Research: Atmospheres*, *122*, 10,983–11,004. https://doi.org/10.1002/2017JD026693

Pfister, P. L., & Stocker, T. F. (2018). The realized warming fraction: A multi-model sensitivity study. *Environmental Research Letters*, *13*(12), 124024. https://doi.org/10.1088/1748-9326/aaebae

Pincus, R., Forster, P. M., & Stevens, B. (2016). The Radiative Forcing Model Intercomparison Project (RFMIP): Experimental protocol for CMIP6. *Geoscientific Model Development*, *9*(9), 3447–3460. https://doi.org/10.5194/gmd-9-3447-2016

Poulter, B., MacBean, N., Hartley, A., Khlystova, I., Arino, O., Betts, R., et al. (2015). Plant functional type classification for earth system models: Results from the European Space Agency's land cover climate change initiative. *Geoscientific Model Development*, *8*(7), 2315–2328. https://doi.org/10.5194/gmd-8-2315-2015

Rayner, N. A. (2003). Global analyses of sea surface temperature, sea ice, and night marine air temperature since the late nineteenth century. *Journal of Geophysical Research*, *108*(D14), 4407. https://doi.org/10.1029/2002JD002670

Resplandy, L., Keeling, R. F., Rödenbeck, C., Stephens, B. B., Khatiwala, S., Rodgers, K. B., et al. (2018). Revision of global carbon fluxes based on a reassessment of oceanic and riverine carbon transport. *Nature Geoscience*, *11*(7), 504–509. https://doi.org/10.1038/s41561-018-0151-3

Salas Mélia, D. (2002). A global coupled sea ice–ocean model. *Ocean Modelling*, *4*(2), 137–172. https://doi.org/10.1016/S1463-5003(01)00015-4

Sallée, J.-B., Matear, R. J., Rintoul, S. R., & Lenton, A. (2012). Localized subduction of anthropogenic carbon dioxide in the Southern Hemisphere oceans. *Nature Geoscience*, *5*(8), 579–584. https://doi.org/10.1038/ngeo1523

Sander, S. P., Abbatt, J., Barker, J. R., Burkholder, J. B., Friedl, R. R., Golden, D. M., et al. (2011). Chemical kinetics and photochemical data for use in atmospheric studies, Evaluation No. 17. JPL Publication 10-6, (5). Retrieved from. http://jpldataeval.jpl.nasa.gov

Schneider, U., Becker, A., Finger, P., Meyer-Christoffer, A., Ziese, M., & Rudolf, B. (2014). GPCC's new land surface precipitation climatology based on quality-controlled in situ data and its role in quantifying the global water cycle. *Theoretical and Applied Climatology*, *115*(1–2), 15–40. https://doi.org/10.1007/s00704-013-0860-x

Séférian, R., Delire, C., Decharme, B., Voldoire, A., David Salas, Y. M., Chevallier, M., et al. (2016). Development and evaluation of CNRM Earth system model-CNRM-ESM 1. *Geoscientific Model Development*, *9*(4), 1423–1453. https://doi.org/10.5194/gmd-9-1423-2016

Séférian, R., Gehlen, M., Bopp, L., Resplandy, L., Orr, J. C., Marti, O., et al. (2016). Inconsistent strategies to spin up models in CMIP5: Implications for ocean biogeochemical model performance assessment. *Geoscientific Model Development*, *9*(5), 1827–1851. https://doi.org/10.5194/gmd-9-1827-2016

Six, K. D., Kloster, S., Ilyina, T., Archer, S. D., Zhang, K., & Maier-Reimer, E. (2013). Global warming amplified by reduced sulphur fluxes as a result of ocean acidification. *Nature Climate Change*, *3*(11), 975–978. https://doi.org/10.1038/nclimate1981

Smeed, D. A., Josey, S. A., Beaulieu, C., Johns, W. E., Moat, B. I., Frajka-Williams, E., et al. (2018). The North Atlantic Ocean is in a state of reduced overturning. *Geophysical Research Letters*, *45*, 1527–1533. https://doi.org/10.1002/2017GL076350

Smith, D. M., Screen, J. A., Deser, C., Cohen, J., Fyfe, J. C., García-Serrano, J., et al. (2018). The Polar Amplification Model Intercomparison Project (PAMIP) contribution to CMIP6: Investigating the causes and consequences of polar amplification. *Geoscientific Model Development Discussion*, 1–42. https://doi.org/10.5194/gmd-2018-82

Sonntag, S., & Hense, I. (2011). Phytoplankton behavior affects ocean mixed layer dynamics through biological-physical feedback mechanisms. *Geophysical Research Letters*, *38*, L15610. https://doi.org/10.1029/2011GL048205

Struthers, H., Bodeker, G. E., Austin, J., Bekki, S., Cionni, I., Dameris, M., et al. (2009). The simulation of the Antarctic ozone hole by chemistry-climate models. *Atmospheric Chemistry and Physics*, *9*(17), 6363–6376. https://doi.org/10.5194/acp-9-6363-2009

Sunda, W. G., & Huntsman, S. a. (1997). Interrelated influence of iron, light and cell size on marine phytoplankton growth. *Nature*, *390*(6658), 389–392. https://doi.org/10.1038/37093

Tagliabue, A., & Völker, C. (2011). Towards accounting for dissolved iron speciation in global ocean models. *Biogeosciences*, *8*(10), 3025–3039. https://doi.org/10.5194/bg-8-3025-2011

Takahashi, T., Broecker, W. S., & Langer, S. (1985). Redfield ratio based on chemical data from isopycnal surfaces. *Journal of Geophysical Research*, *90*(C4), 6907. https://doi.org/10.1029/JC090iC04p06907

Talley, L. D., Lobanov, V., Ponomarev, V., Salyuk, A., Tishchenko, P., Zhabin, I., & Riser, S. (2003). Deep convection and brine rejection in the Japan Sea. *Geophysical Research Letters*, *30*(4), 1159. https://doi.org/10.1029/2002GL016451

Thomason, L. W., Ernest, N., Millán, L., Rieger, L., Bourassa, A., Vernier, J.-P., et al. (2018). A global space-based stratospheric aerosol climatology: 1979–2016. *Earth System Science Data*, *10*(1), 469–492. https://doi.org/10.5194/essd-10-469-2018

Valente, A., Sathyendranath, S., Brotas, V., Groom, S., Grant, M., Taberner, M., et al. (2016). A compilation of global bio-optical in situ data for ocean-colour satellite applications. *Earth System Science Data*, *8*(1), 235–252. https://doi.org/10.5194/essd-8-235-2016

van den Hurk, B., Kim, H., Krinner, G., Seneviratne, S. I., Derksen, C., Oki, T., et al. (2016). LS3MIP (v1.0) contribution to CMIP6: the Land Surface, Snow and Soil moisture Model Intercomparison Project—aims, setup and expected outcome. *Geoscientific Model Development*, *9*(8), 2809–2832. https://doi.org/10.5194/gmd-9-2809-2016

van Marle, M. J. E., Kloster, S., Magi, B. I., Marlon, J. R., Daniau, A.-L., Field, R. D., et al. (2017). Historic global biomass burning emissions for CMIP6 (BB4CMIP) based on merging satellite observations with proxies and fire models (1750–2015). *Geoscientific Model Development*, *10*(9), 3329–3357. https://doi.org/10.5194/gmd-10-3329-2017

Vial, J., Dufresne, J. L., & Bony, S. (2013). On the interpretation of inter-model spread in CMIP5 climate sensitivity estimates. *Climate Dynamics*, *41*(11–12), 3339–3362. https://doi.org/10.1007/s00382-013-1725-9

Vogt, M., Vallina, S. M., Buitenhuis, E. T., Bopp, L., & Le Quéré, C. (2010). Simulating dimethylsulphide seasonality with the dynamic green ocean model PlankTOM5. *Journal of Geophysical Research*, *115*, C06021. https://doi.org/10.1029/2009JC005529

Voldoire, A., Decharme, B., Pianezze, J., Lebeaupin Brossier, C., Sevault, F., Seyfried, L., et al. (2017). SURFEX v8.0 interface with OASIS3-MCT to couple atmosphere with hydrology, ocean, waves and sea-ice models, from coastal to global scales. *Geoscientific Model Development*, *10*(11), 4207–4227. https://doi.org/10.5194/gmd-10-4207-2017

Voldoire, A., Saint-Martin, D., Sénési, S., Decharme, B., Alias, A., Chevallier, M., et al. (2019). Evaluation of CMIP6 DECK experiments with CNRM-CM6-1. *Journal of Advances in Modeling Earth Systems*, *11*, 2177–2213. https://doi.org/10.1029/2019MS001683

Wales, P. A., Salawitch, R. J., Nicely, J. M., Anderson, D. C., Canty, T. P., Baidar, S., et al. (2018). Stratospheric injection of brominated very short-lived substances: Aircraft observations in the western Pacific and representation in global models. *Journal of Geophysical Research: Oceans*, *123*, 5690–5719. https://doi.org/10.1029/2017JD027978

Wanninkhof, R. (2014). Relationship between wind speed and gas exchange over the ocean revisited. *Limnology and Oceanography: Methods*, *12*(6), 351–362. https://doi.org/10.4319/lom.2014.12.351

Webb, M. J., Andrews, T., Bodas-Salcedo, A., Bony, S., Bretherton, C. S., Chadwick, R., et al. (2017). The Cloud Feedback Model Intercomparison Project (CFMIP) contribution to CMIP6. *Geoscientific Model Development*, *10*(1), 359–384. https://doi.org/10.5194/gmd-10-359-2017

Wenzel, S., Cox, P. M., Eyring, V., & Friedlingstein, P. (2016). Projected land photosynthesis constrained by changes in the seasonal cycle of atmospheric CO2. *Nature*, *538*(7626), 499–501. https://doi.org/10.1038/nature19772

Yin, X. (2002). Responses of leaf nitrogen concentration and specific leaf area to atmospheric CO 2 enrichment: a retrospective synthesis across 62 species. *Global Change Biology*, *8*(7), 631–642. Retrieved from. http://www.blackwell-synergy.com/links/doi/10.1046/j.1365-2486.2002.00497.x/abs/

Zanchettin, D., Khodri, M., Timmreck, C., Toohey, M., Schmidt, A., Gerber, E. P., et al. (2016). The model intercomparison project on the climatic response to volcanic forcing (VolMIP): Experimental design and forcing input data for CMIP6. *Geoscientific Model Development*, *9*(8), 2701–2719. https://doi.org/10.5194/gmd-9-2701-2016

Zelinka, M. D., & Hartmann, D. L. (2010). Why is longwave cloud feedback positive? *Journal of Geophysical Research*, *115*, D16117. https://doi.org/10.1029/2010JD013817

Zeng, Z., Piao, S., Li, L. Z. X., Zhou, L., Ciais, P., Wang, T., et al. (2017). Climate mitigation from vegetation biophysical feedbacks during the past three decades. *Nature Climate Change*, *7*(6), 432–436. https://doi.org/10.1038/nclimate3299

Zhang, J., Tian, W., Xie, F., Chipperfield, M. P., Feng, W., Son, S.-W., et al. (2018). Stratospheric ozone loss over the Eurasian continent induced by the polar vortex shift. *Nature Communications*, *9*(1), 206. https://doi.org/10.1038/s41467-017-02565-2

Zheng, G., & DiGiacomo, P. M. (2017). Remote sensing of chlorophyll-a in coastal waters based on the light absorption coefficient of phytoplankton. *Remote Sensing of Environment*, *201*, 331–341. https://doi.org/10.1016/j.rse.2017.09.008

Zhou, T., Turner, A. G., Kinter, J. L., Wang, B., Qian, Y., Chen, X., et al. (2016). GMMIP (v1.0) contribution to CMIP6: Global monsoons model inter-comparison project. *Geoscientific Model Development*, *9*(10), 3589–3604. https://doi.org/10.5194/gmd-9-3589-2016

Zhu, Z., Bi, J., Pan, Y., Ganguly, S., Anav, A., Xu, L., et al. (2013). Global data sets of vegetation leaf area index (LAI)3g and fraction of photosynthetically active radiation (FPAR)3g derived from global inventory modeling and mapping studies (GIMMS) normalized difference vegetation index (NDVI3G) for the period 1981 to 2011. *Remote Sensing*, *5*(2), 927–948. https://doi.org/10.3390/rs5020927

Zuidema, P., Redemann, J., Haywood, J., Wood, R., Piketh, S., Hipondoka, M., & Formenti, P. (2016). Smoke and clouds above the Southeast Atlantic: Upcoming field campaigns probe absorbing aerosol's impact on climate. *Bulletin of the American Meteorological Society*, *97*(7), 1131–1135. https://doi.org/10.1175/bams-d-15-00082.1

Zweng, M. M., Reagan, J. R., Antonov, J. I., Locarnini, R. A., Mishonov, A. V., Boyer, T. P., et al. (2013). In S. Levitus, & A. Mishonov (Eds.), *World ocean atlas 2013, Volume 2: Salinity*, NOAA Atlas NESDIS, (Vol. *74*, p. 39).